SCanning Imaging Absorption spectroMeter for Atmospheric ChartograpHY - Phase E

Slit function comparisons with level 0 data

summary

For objective 79 internal spectral line source (SLS) and sun measurements are analysed. The in-flight data originates from the switch on data acquisition phase (SODAP). The measurements are carefully selected to exclude possible changes over time (e.g. decontaminations, contaminations).

With the focus on the slit function, in-flight internal SLS are analysed with the help of several fitting algorithms. Per channel a recommendation for the preferred function is given, which is the optimal function for most lines within a channel. For the slit function suggested the simplicity of the algorithm is taken into account. In addition, results from the on-ground measurements are shown.

Three different sun observation measurements with small and large aperture as well as via the elevation scan mechanism (ESM) -mirror and -diffuser are carefully selected and investigated. The Fraunhofer lines are given in an existing key data product. This previously delivered list is transformed to vacuum wavelengths and checked versus on-ground zenith sky measurements as well as in-flight data. Lines are added and rejected. Results of the full width at half maximum (FWHM) are compared.

Prepared	: Berit Ahlers		22 June, 2004
Checked	: Coen Schrijvers		22/06/2004
Agreed	: Erik Boslooper	E.C. Bosl	

DISTRIBUTION LIST

Paper copy		TNO TPD	
J. Carpay	NIVR	Berit Ahlers C. Schrijvers E. Boslooper	1x 1x 1x
.pdf file			
A. von Bargen H. Bovensmann C. Chlebek J. Frerick M. Gottwald Q. Kleipool E. Krieg G. Lichtenberg S. Slijkhuis	DLR IFE DLR ESTEC DLR SRON DLR SRON DLR		

DOCUMENT CHANGE RECORD

Issue	Date	Number of pages	Short description	Page
1	22-06-2004	62 (plus pages in Annex 4)	First issue	All

CONTENTS

1. Introduction

Slit functions are determined from internal spectral light source (SLS) measurements and sun observations from Fraunhofer lines. The sun observations are performed with the small or large aperture, via the elevation scan mechanism (ESM) –mirror or diffuser.

In chapter 3 the carefully selected measurements used and the associated information - i.e. pixel exposure times (PET), detector and optical bench module (OBM) temperatures, data correction- will be given.

The fourth chapter describes the concept and approach for the objective including the fitting algorithms used.

The analysis results are in chapter 5. The first part [chapter 5.1] concerns the slit function results of the internal SLS. Several algorithms have been used to retrieve a slit function per emission line and per channel. Results of the full width at half maximum (FWHM) are stated. The second part [chapter 5.2] provides the analysis of three sun measurements in different modes. An on-ground zenith sky measurement is at first instance used for the determination of the Fraunhofer lines selected. Relative comparisons of the fits and FWHM are presented.

One prerequisite for the performed measurements in-flight was, that the detector temperatures had to be as close as possible to the on-ground (= requirement for in-flight) values to get meaningful comparisons. This has not been the case during SODAP. Therefore care has to be taken during the interpretation of the data.

2. Documents

2.1 Applicable Documents

AD01 SCIAMACHY Instrument Requirements Document, PO-RS-DAR-SH-0001, issue 3C, 25 September 1998.

2.2 References

RD01 Wavelength and slit function calibration of the SCIAMACHY PFM, TN-SCIA-1000TP/189, issue 1, 15 February 1999.

RD02 OPTEC5: Slit function calibration of the SCIAMACHY PFM, RP-SCIA-1000TP/267, issue 1, 14 December 2000.

RD03 Recalculation of OPTEC5 Non-Linearity, SRON–SCIA–PhE–RP–013, issue 1, rev. 0, 12 November 2003.

RD04 Ch 1-5 Memory Effect I: Key data implementation and in-flight measurements, SRON–SCIA–PhE–RP–11, issue 2, 12 September 2003.

RD05 Algorithm Specification for Dark Signal Determination, SRON–SCIA–PhE–RP–009, issue 1, rev. 0, 14 April 2003.

RD06 Estimation of missing dark signal parameters, SRON-SCIA-PhE-RP-012, version 1, rev. 0, 24 March 2004.

R07 CD SRON Dark current Sciamachy 23 March 2004.

RD08 Basic pre-processing and data-correction for in-orbit calibration, TPD-SCIA-PhE-TN-003, issue 1, 16 December 2002.

R09 SOST Web page, http://atmos.af.op.dlr.de/projects/scops/.

RD10 The Ambient-Performance Test Evaluation Report, RP-SCIA-0000FO/205, issue 1, 2 July 1999.

RD11 ENVISAT-1 SCIAMACHY Level 0 to 1c Processing Algorithm Theoretical Basis Document, ENV-ATB-DLR-SCIA-0041, issue 3, 3 February 2004.

RD12 Sun-over-ESM-diffuser incl. ESM angle variation – in-flight, TPD-SCIA-PhE-RP-008, issue 1, 10 November 2003.

RD13 In-orbit NDF optical properties, TPD-SCIA-PhE-RP-002, issue 1, 16 December 2002.

RD14 In-orbit performance monitoring of ESM-diffuser versus ESM-mirror, TPD-SCIA-PhE-RP-003, issue 1, 16 December 2002.

RD15 Comparison of SLS and WLS calibration measurements on-ground and in-flight, TPD-SCIA-PhE-TN-013, issue 1, 8 April 2004.

RD16 Optec Cold Tests Instrument Performance Evaluation Report, RP-SCIA-0000FO/191, issue 1, 18 December 1997.

RD17 SCIAMACHY in-flight instrument performance, H. Bovensmann et al., proceedings of the ENVISAT Calibration Review (SP-520), ESA Publications Division, 2002.

RD18 OPTEC5: Wavelength calibration of the SCIAMACHY PFM, RP-SCIA-1000TP/266, issue 1, 4 December 2000.

2.3 Abbreviations

AIT	Assembly, integration and test
APSM	Aperture sun mechanism
ASM	Azimuth scan mechanism
BU	Binary units
CoAdd	Co-adding
EGSE	Electrical ground support equipment
ESM	Elevation scan mechanism
FWHM	Full width half maximum
IR	Infrared
IT	Integration time (=PET*CoAdd)
ME(C)	Memory effect (correction)
MLI	Multi layer insulation
MSM	Measurement
NCWM	Nadir cover window mechanism
NDF(M)	Neutral density filter (mechanism)
NIR	Near infrared
NL	Non linearity
OBM	Optical bench module
OPTEC	Optical test facility
PET	Pixel exposure time
PI	Principle investigator
RD	Reference document
SCIAMACHY/ SCIA	Scanning imaging absorption spectrometer for atmospheric cartography
SCOE	Sciamachy check-out equipment
SFS	Sun follower
SLS	Spectral line source
SO&C	Sun occultation and calibration
SODAP	Switch on data acquisition phase
SRC	SCIA radiant cooler
temp	Temperature
TL	Timeline
TV	Thermal vacuum
UV	Ultra violet
VIS	Visual

3. List of measurements and associated information

The measurements used for this analysis are performed with either the internal spectral line source (SLS, mounted in the calibration unit) or the sun and measured by the SCIAMACHY detector via the scan mechanism(s). The first part of this chapter describes the measurements used, the second describes the associated pixel exposure times (PETs) and co-addings (CoAdds), the third the measured detector and optical bench module (OBM) temperatures and the fourth the data correction.

3.1 Measurements

Several measurements are used in this work:

- The standard *internal spectral line source* (SLS) measurements with a PtCrNe hallow cathode lamp (state_ID 59, dedicated dark state_ID 9);
- The *sun-via-ESM-diffuser* via the limb port, azimuth scan mechanism (ASM) mirror and elevation scan mechanism (ESM) diffuser with the neutral density filter (NDF) to reduce the light detected by channels 3 to 6 with a factor of about 5 (state_ID 62);
- The *sub-solar-calibration-pointing* (state_ID 53) via the sub-solar port, ESM mirror and
- The *sun-occultation-and-calibration-pointing* measurement (SO&C, state_ID 51) via the limb port over the two mirrors (ASM- and ESM-mirror). SO&C window starts at sunrise to sun above atmosphere.

A first suggestion was to also implement an internal SLS measurement with the small aperture in the light path as measured on-ground to have a direct comparison between small (0.045° x 0.72°) and large aperture (0.045° x 1.8°) results. It turned out to be not possible to be implemented in the switch on data acquisition phase (SODAP). Therefore the suggested comparison can't be performed.

The measurements from SODAP have been carefully selected. It was the intention to choose orbital files executed within a minimum timeframe, without decontaminations and instrument/ satellite failures in between. All measurements used for this work are retrieved around orbit 1650 considering the previous mentioned trade-offs. A detailed list of these measurements can be found in the Annex 1.

A short overview about the measurement setups is given in the following table. The ESM and ASM angles as set during the different activities are listed as well as several mechanism settings like the small or large aperture and the nadir calibration window (NCWM).

Table 1 Overview of main settings within the flight states used in this work. The nadir calibration window mechanism (NCWM), the aperture stop mechanism (APSM), the NDF mechanism and scan mechanism settings are given. (Internal SLS angle settings in brackets from OPTEC5.)

State description	State_IDs	NCWM	APSM[i)]	NDFM	ESM [°]	ASM [°]
SO&C_Pointing	51	closed	**small**	**in**	-13.39, -12.65	-33, -33.4
Sub_Solar_Cal_Pointing	53	**open**	**small**	**in**	56.93, 56.88	0, 3.6
Spectral_Lamp_Cal	59	closed	large	out	9.78 (9.765)	0 (45.00)
Sun_ESM_Diffuser_Cal	62	closed	large	**in**	165	-33.6, 34.7

i) small aperture 0.045° x 0.72°, large aperture 0.045° x 1.8°

Originally the ASM unused position was 45 degrees. Since the ASM did undergo a hardware modification i.e. a grinded aluminium diffuser has been fixed on the mirror's backside, it has been decided to change the unused position to zero degrees. During the OPTEC5 internal SLS measurement the ASM unused position is still 45 degrees. The measurements via the diffuser are performed with an almost 180 degrees rotation in ESM angle setting. The measurements used are listed in the Annex 1.

3.2 PET and Coadding settings

In Table 2 the pixel exposure times (PETs in seconds) and CoAdds for the states used are shown. Multiplication of PET and CoAdd yields the integration time (IT). Dark signal measurements (e.g. D_SLS_Pre59) generally surround a corresponding light measurement (e.g. SLS_Pre59) during SODAP. The only difference between the so-called light and dark signal measurements is that the light source is switched on or off, respectively not pointed to.

The *sub-solar-calibration-pointing* (state_ID 53) IT has been changed from the originally planned settings in that way, that channels 3 and 6 have a complete readout after one second, while the other channels are readout after half a second. The ITs are also different for the *sun-occultation-and-calibration-pointing* (state_ID 51) after CoAdd changes. The background of the IT changes is not completely clear, but the consequence of these changes is that the detectors are likely to measure different images/ scenery.

Table 2 Pixel exposure times (PETs) in seconds and CoAdds as set for the SCIA channels during the different measurement executions. Shading symbolises different ITs versus the other channels. The originally planned settings are in brackets.

CH	1a	1b	2a	2b	3	4	5	6	7	8
Sun occultation & calibration pointing (state_ID 51)										
PET [s]	0.0625	0.0625	0.0625 (0.03125)	0.0625 (0.03125)	0.0625	0.0625	0.0625	0.03125	0.0625 (0.03125)	0.0625
Coadd	1	1	1	1	2 (1)	2 (1)	2 (1)	2 (1)	1	2 (1)
Sub solar calibration pointing (state_ID 53)										
PET [s]	0.0625	0.0625	0.0625 (0.03125)	0.0625 (0.03125)	0.0625	0.0625	0.0625	0.03125	0.0625 (0.03125)	0.0625
Coadd	8	8	8	8	16 (8)	8	8	16 (8)	8	8
Spectral lamp calibration (Internal SLS, OPTEC 5 state_IDs 9,59)										
PET [s]	4	4	2	2	0.125	0.03125	0.25	0.25	1	1
Coadd	1	1	2	2	32	64	16	16	4	4
Sun via ESM diffuser calibration with NDF in (state_ID 62)										
PET [s]	0.0625	0.0625	0.0625	0.0625	0.03125	0.03125	0.0625	0.03125	0.125	0.125
Coadd	2	2	2	2	2	2	2	2	1	1

3.3 Detector and OBM temperatures

In Table 3 the average temperatures of the detectors and at different locations on the optical bench module (OBM) are given per orbit for the measurements used [see Annex 1]. The column: “OPTEC5 low” represents the detector temperature settings during the on-ground phase in 1999 at Schiphol while the instrument was in the vacuum chamber under an average pressure of $1.8*10^{-4}$ Pascal. The OPTEC5 low temperature settings are equal to the SODAP and nominal in-flight operation required settings.

The requirement for the detector temperatures in-flight are that they shall be as close as possible to on-ground values to allow meaningful comparisons of the performed activities.

Between June 2002 (around orbit 1455) and February 2003 (orbit 5119) the detector temperatures were far out of range due to erroneous commanding inputs. The changed inputs to reach the requirements have been made effective on 21 February 2003. This is equivalent to orbit 5119 and long after the SODAP and Delta-SODAP where the measurements used for this work have been executed.

Therefore the main requirement for the analysis of SODAP and Delta-SODAP measurements is not fulfilled and meaningful comparisons to on-ground results are hampered.

In addition, channels 7 and 8 suffer from contamination (the so called ice-layer build-up), which changes with time.

Table 3 Detector and OBM temperature settings during on-ground OPTEC5 tests, which have been the requirement for SODAP and in-flight MSM's (the orbit numbers from the used raw files are stated).

Orbit	OPTEC 5 low	1634	1640	1642	1658	1684	5594
CH	Temperature [K]						
1	207.5	204.6	204.6	204.6	204.6	204.6	207.1
2	207.0	204.1	204.1	204.1	204.1	204.1	206.6
3	224.8	223.3	223.3	223.2	223.3	223.2	224.8
4	223.6	221.8	221.8	221.8	221.8	221.8	223.9
5	221.9	220.0	220.0	220.0	220.0	220.0	222.2
6	203.3	198.9	198.9	199.0	198.8	198.8	200.2
7	150.9	150.5	150.6	150.6	150.6	150.6	149.3
8	146.8	149.3	149.3	149.3	149.4	149.4	148.0
AZ	-	258.2	258.2	258.2	258.2	258.2	258.2
ELEV	-	256.7	256.8	256.7	256.8	256.8	256.8
RAD	-	251.5	251.5	251.5	251.5	251.5	251.5
OBM	255.3	1)	1)	1)	1)	1)	1)

1) see SOST webpage [R09], nominal temperature of -17.9° C.

In the following graph the difference between the in-orbit reached detector temperatures per channel versus the requirement values are plotted. The NIR channels 6 and 8 are furthest off with more than four degrees in channel 6, and 2.5 K in channel 8. The temperatures are stable around orbit 1650. The detector temperatures for orbit 5594 (after the re-settings) are shown as well, relevant for one *sub-solar-calibration-pointing* measurement. The UV and VIS channels 1 to 5 are closest to the requirement.

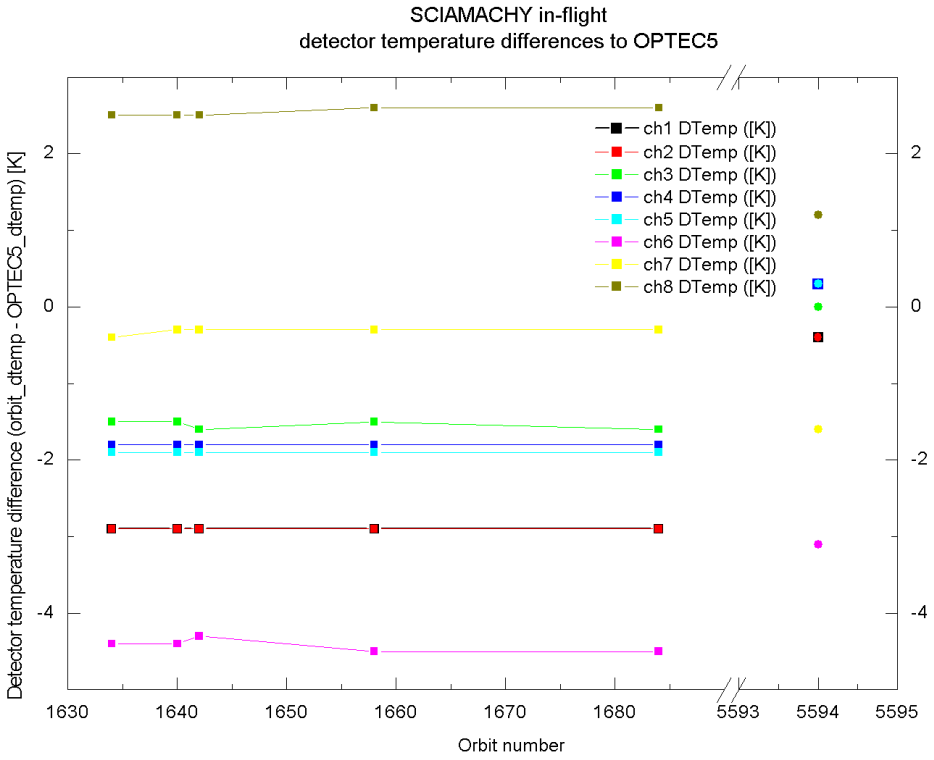

Figure 1 Detector temperature differences for each channel between the orbit files used and OPTEC5 values. Temperatures from orbit 5594 are after the detector temperature setting change in February 2003.

From Table 3 and Figure 1 it follows that the detector temperature requirements for in-flight were never met during SODAP and Delta-SODAP.

3.4 Data correction

Averaging data records is described per state, since the state execution is possibly split in different acquisition phases. The first record is eliminated as required by the memory effect correction (MEC) algorithm. Correction for the reticon memory effect (ME, channels 1 to 5) is applied according to the new specification, which was derived in RD04. The new specification for the correction of the effect (look-up table) was incorporated in the pre-processing software described in RD08. The latest version of the look-up table was provided by SRON as contained in file, and labelled 10 October 2003. The non-linearity (NL) correction concerns the InGaAs detectors (channels 6 to 8) as described in RD03. The specification for the correction of the effect was incorporated in the pre-processing software described in RD08. The latest version of the specification was provided by SRON.

Subsequently, the data is corrected for dark current and electronic offset. Due to missing dedicated dark measurements a modelled dark is constructed from dark-current and analogue offset parameters provided by SRON, which were derived from in-orbit measurements as described in RD05 and RD06. For each orbit a dark model was calculated and supplied on CD [see R07]. For the calculation of these parameters the ME and NL effect have been taken into account. The modelled dark is then subtracted from the data, which yields a dark signal corrected spectrum.

All data used is normalised to one second and Coadd one [measured in BU/s].

4. Concept and approach

The slit function for both the small and large aperture from Fraunhofer lines (delivered as key data by DLR, Sander Slijkhuis) and slit function for large aperture from *internal SLS* are determined. The averaged and dark signal corrected spectrum obtained from a *sun-over-ESM-diffuser* (sun irradiance measurement) observational sequence and an averaged dark signal corrected *internal SLS* spectrum can be used to determine the slit function per channel and the variations within each channel. The difference between the results from the two measurement types can serve to examine the differences between internal and external illumination (SLS blocking effect). The sun observation *SO&C-pointing* and *sub-solar-calibration-pointing* results are compared relatively.

Meaning of objective is understood as: Verify applicability of on-ground slit function key data for in-flight conditions. Determination of absolute slit function based on Fraunhofer lines is considered out-of-scope.

The wavelength calibration, analysed as amongst others described in RD15, is performed with the internal SLS measurement in orbit 1642.

The purpose of the slit function calibration with the *internal SLS* is to describe the instrument response (both optically and electronically) to spectral lines that are spectrally much narrower than the spectral resolution of the SCIAMACHY instrument. The slit function describes how the instrument measures narrow spectral lines.

For the slit function analysis the dark signal corrected averaged internal SLS measurement will be fitted using several algorithms. The best fit per channel will be determined and results put in context with OPTEC5 results. The following algorithms as previously used in RD01 and RD02 have been used:

- **Gaussian**:

$$y = a[1] * \exp\left[-\left(\frac{x - a[2]}{a[3]}\right)^2\right] + a[4] + a[5] * x \qquad (1)$$

with a full width at half maximum (FWHM) of

$$FWHM = 2 * a[3] * \sqrt{\ln 2} \qquad (1.1)$$

- **Double Gaussian**:

$$y = a[1] * \exp\left[-\left(\frac{x - a[2]}{a[3]}\right)^2\right] + a[4] * \exp\left[-\left(\frac{x - a[2]}{a[5]}\right)^2\right] + a[6] + a[7] * x \qquad (2)$$

with FWHM of:

$$FWHM1 = 2 * a[3] * \sqrt{\ln 2} \qquad (2.1)$$

$$FWHM2 = 2 * a[5] * \sqrt{\ln 2} \qquad (2.2)$$

The total function FWHM is a more complicated function of a[1]-a[5].

- **Lorentzian**:

$$y = \frac{a[1]}{(a[2])^2 + (x - a[3])^2} + a[4] + a[5] * x \qquad (3)$$

with the FWHM of:

$$FWHM = 2 * a[2] \qquad (3.1)$$

- **Squared hyperbolic secant:**

$$y = a[2] * \sec h^2\left(\frac{1.7628 * (x - a[1])}{a[3]}\right) + a[4] + a[5] * x \tag{4}$$

with:

$$\sec h(x) = \frac{2}{e^x + e^{-x}} \tag{4.1}$$

and a FWHM of:

$$FWHM = a[3] \tag{4.2}$$

- **Voigt:**

$$y = \frac{a[1] * a[3]}{\sqrt{2} * \pi\sqrt{\pi} * a[4]} \int_{-\infty}^{\infty} \frac{\exp\left[-\frac{(x-w)^2}{2\sqrt{a[4]}}\right]}{(a[2]-w)^2 + (a[3])^2} dw + a[5] + a[6] * x \tag{5}$$

The final FWHM is determined by the Lorentzian width parameter a[3] (gamma) and the Gaussian width parameter a[4] (delta).

- **Exponential:**

$$y(x) = a[1] * e^{-\ln 2\left(\frac{x-a[2]}{a[3]}\right)^4} + a[4] + a[5]x \tag{6}$$

with

a[1]: height;

a[2]: position;

a[3]: FWHM;

a[4]: background level and

a[5]: background linear coefficient;

- **Simple hyperbolic:**

$$y = \frac{(a[3])^2}{(a[1])^2 + (x - a[2])^4} + a[4] + a[5] * x \tag{7}$$

$$FWHM = 2\sqrt{a[1]} \tag{7.1}$$

- **Compound hyperbolic:**

$$y = \frac{(a[3])^2}{(a[1])^2 + (x - a[2])^2} + \frac{(a[4])^2}{(a[1])^2 + (x - a[2])^4} + a[5] + a[6] * x \tag{8}$$

The final FWHM is determined by the width parameter a[1], but not equal to it.

Particularly channels 7 and 8 are not thoroughly analysed in this document for amongst others the following reasons:

- PtCrNe hallow cathode lamp does not provide enough PtCrNe emission lines;
- So-called ice layer build-up, less transmission.

Hans Schrijver/ SRON is investigating the widening of the slit function due to the contamination in these channels.

For the sun spectra careful selection of data is performed. Fraunhofer lines suggested in the key data are in first instance evaluated with the help of an on-ground zenith sky measurement. The Gaussian algorithm is used to retrieve the full width at half maximum (FWHM) values, which are relatively compared with each other. It is not the intention of this work to derive absolute data on the Fraunhofer lines.

For two sun observations the Doppler shift as described in the ATBD [see RD11] has to be considered. In equation 21 on page 46 of the ATBD the Doppler shift at 500 nanometres is mentioned:

$$d_{500nm} = 1.66782 * 10^{-6} * \sqrt{x^2 + y^2 + z^2} * \cos\theta_{AZ} * \cos\theta_{Elev} [nm] \quad (9)$$

with

$\sqrt{x^2 + y^2 + z^2}$ - velocity spacecraft in [m/s].

For the sun occultation measurements the average azimuth angle and average elevation scan angles in the state are used for theta. For the sun-over-diffuser states the azimuth angle equals the solar elevation angle The Doppler shift correction is not required for sub-solar measurements ($d_{500nm} = 0$).

5. Slit function analysis results

The first part of this chapter provides a detailed description about the results of the slit function determined with the *internal SLS* measurement; the second part [see section 5.2] presents the analysis of different sun observation measurements, the *sun-occultation-and-calibration-pointing*, the *sub-solar-calibration-pointing* and the *sun-over-ESM-diffuser-calibration*. The results of the fits are compared hereafter.

In general the dark signal correction by SRON is used. For the internal SLS measurement (state_ID 59) also a dedicated dark measurement is used.

Be aware, that while the x-axis shows a pixel scale the read-out for channel 2 is reversed compared to the wavelength grid. Smaller wavelengths correspond to higher pixel numbers in this channel.

5.1 Internal SLS measurements

In orbit 1684 the internal SLS has been measured including a dedicated dark signal measurement. The raw SLS data has been corrected with this dedicated dark signal measurement and compared with the modelled dark signal corrected data. The two corrected spectra are almost identical, even with a dark-model quality of 40 [see R07] and the differences of the FWHM results are smaller than 0.005 pixels and can be disregarded. In the following the modelled dark is used.

5.1.1 Example lines

Several algorithms [see equations in chapter 4] are tested on the spectral data to fit the literature vacuum wavelengths [see Annex 2] and retrieve the optimal slit function per channel/ line. The SLS data used is from orbits 1642 and 1684, i.e. after all covers have been opened and close to the investigated sun spectra observations. As example one line per channel is shown in the following with the different fits on the orbit 1684 data.

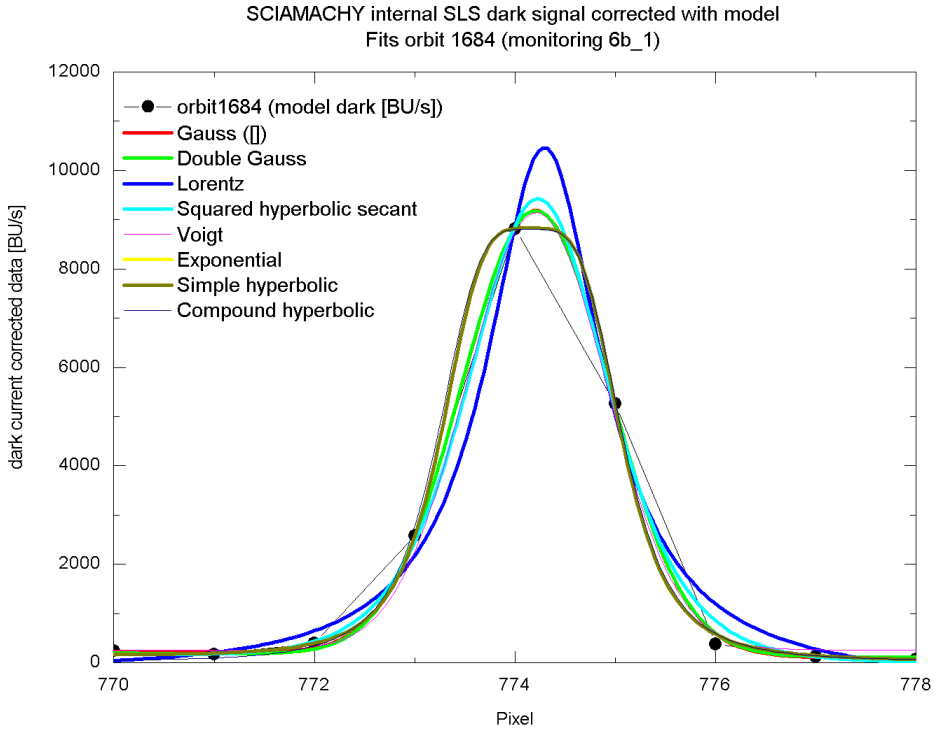

Figure 2 In **Channel 1** measured Platinum line corresponding to the literature vacuum wavelength of **306.5600 nm**. Averaged, dark signal corrected with model dark and normalised SLS signals in BU per second from **orbit 1684** (black) during SODAP with all covers open. Several fits are over plotted and are therefore less visible.

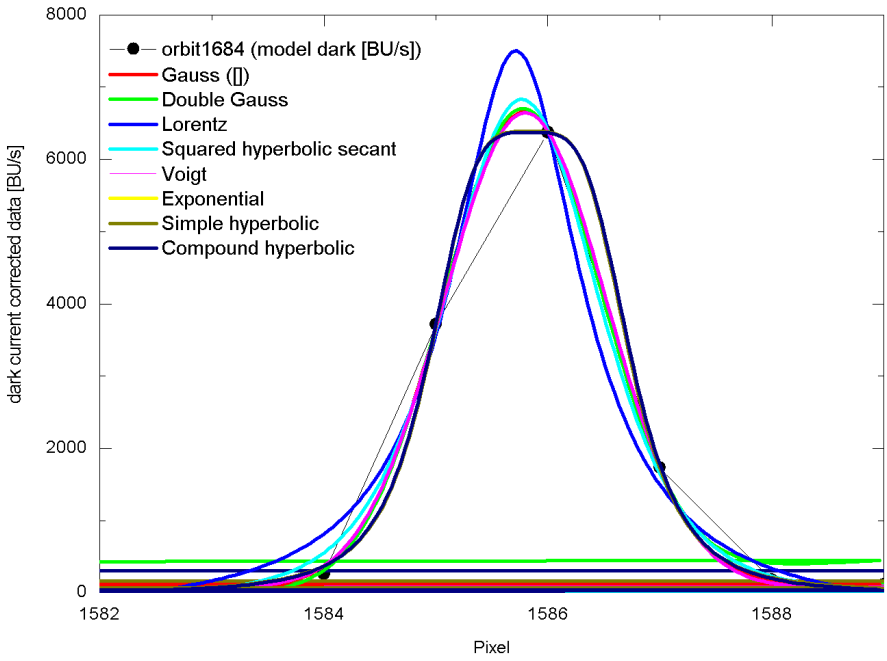

Figure 3 In **Channel 2** measured Neon line corresponding to the literature vacuum wavelength of **352.14783 nm**. Averaged, dark signal corrected and normalised SLS signals in BU/s from **orbit 1684** (black) during SODAP with all covers open. Several fits are over plotted and are therefore less visible (fitting lines crossing in lower part of graph due to the opposite pixel/ wavelengths readout in this channel).

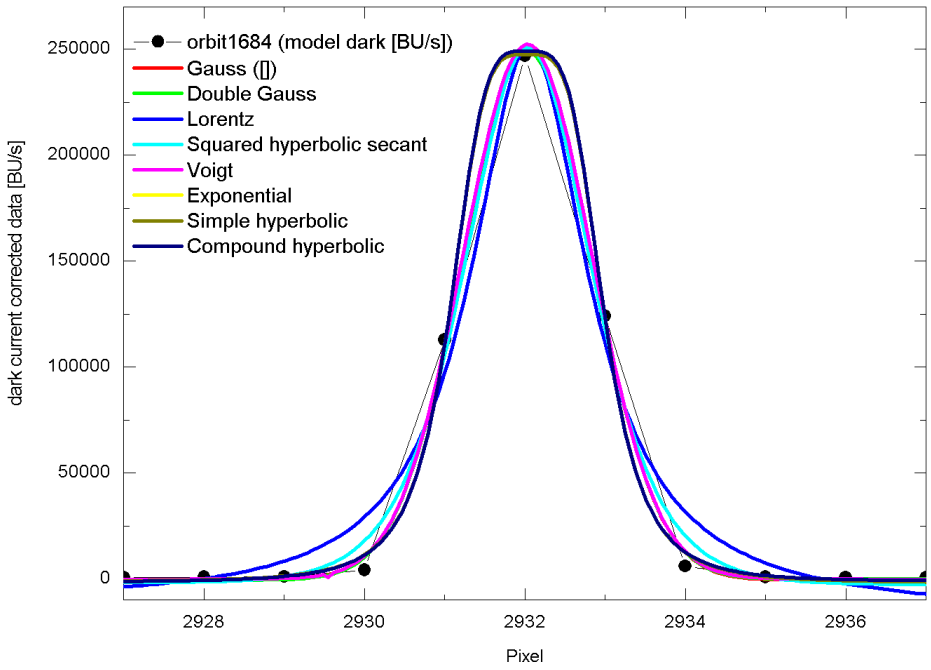

Figure 4 In **Channel 3** measured Neon line corresponding to the literature vacuum wavelength of **594.64812 nm**. Averaged, dark signal corrected and normalised SLS signals in BU per second from **orbit 1684** (black).

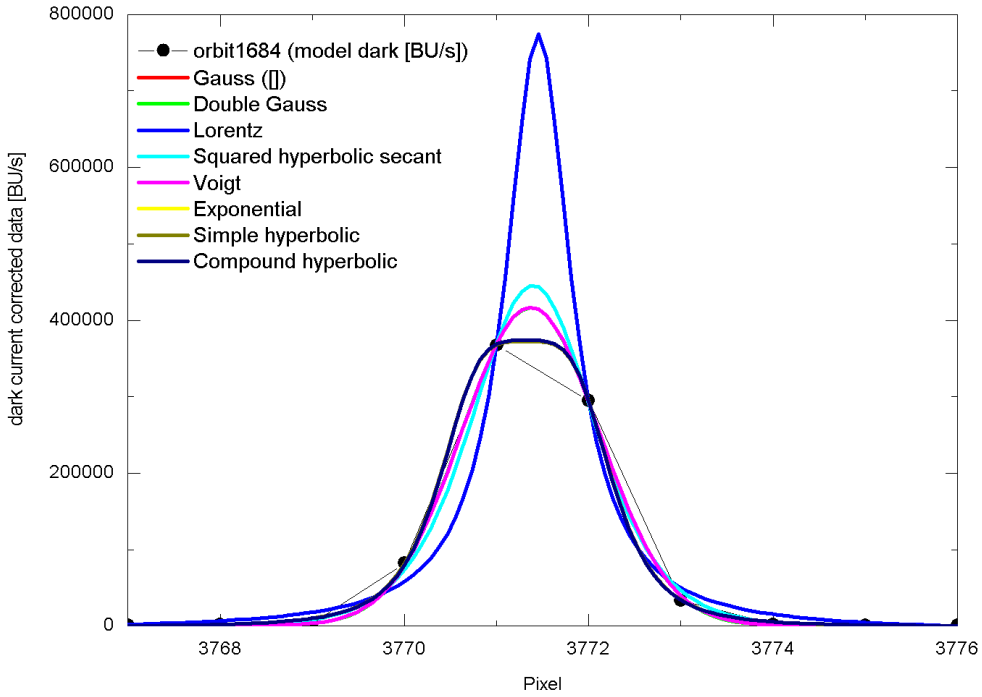

Figure 5 In **Channel 4** measured Neon line corresponding to the literature vacuum wavelength of **744.09472 nm**. Averaged, dark signal corrected and normalised SLS signals in BU per second from **orbit 1684** (black).

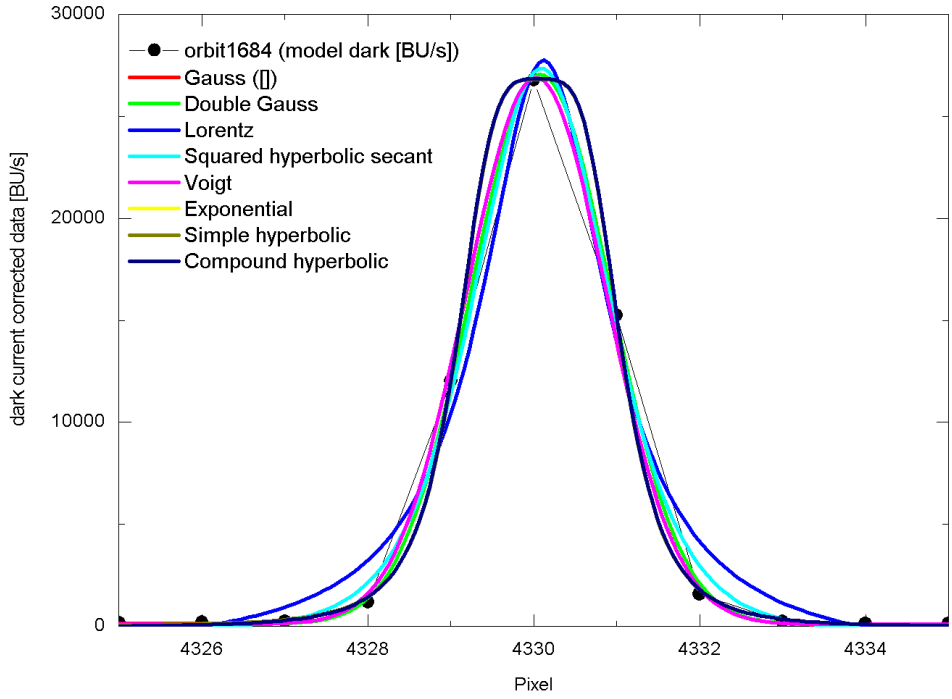

Figure 6 In **Channel 5** measured Neon line corresponding to the literature vacuum wavelength of **849.76940 nm**. Averaged, dark signal corrected and normalised SLS signals in BU per second from **orbit 1684** (black).

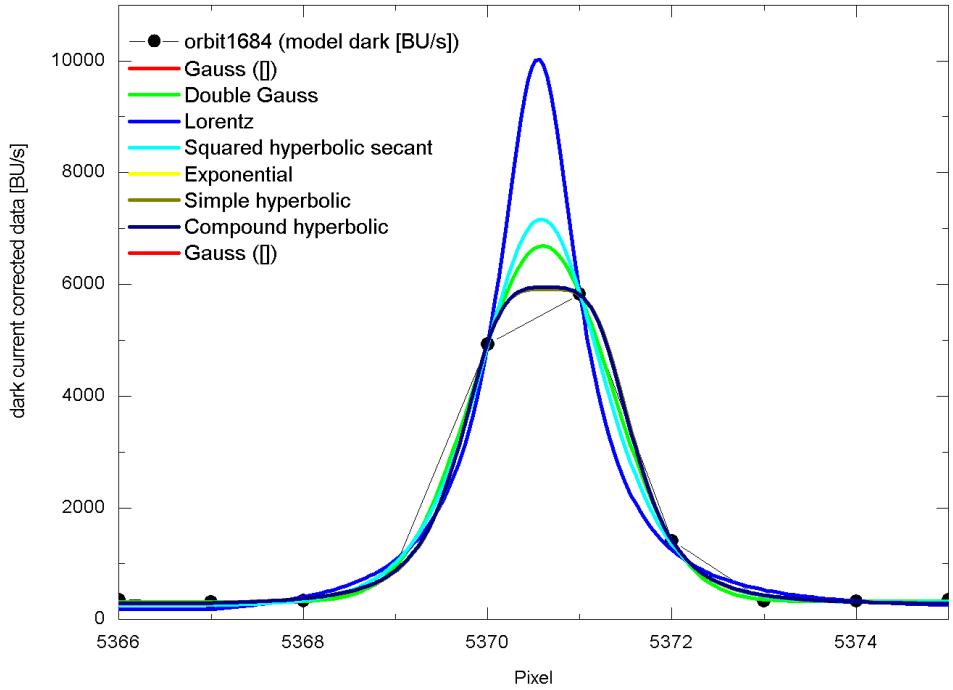

Figure 7 In **Channel 6** measured Neon line corresponding to the literature vacuum wavelength of **1169.12011 nm**. Averaged, dark signal corrected and normalised SLS signals in BU per second from **orbit 1684** (black).

A list of fitted lines is given in the annex [see Annex 2]. Changes of the expected pixel positions (from 0 to 1023 for each channel) and the fitting windows versus OPTEC5 are marked in that list.

The Gaussian and simple hyperbolic result graphs for all fitted lines are attached in the end of this report [see Annex 4].

The fits in channels 7 and 8 are not further evaluated, since the calibration in these channels is based on the cat-gas measurements amongst others due to the lack of emission lines of the PtCrNe hallow cathode lamp in this wavelength region. In addition, the so-called ice layer build-up during SODAP has an influence on the measured line intensities and the slit function. As previously mentioned further research for channels 7 and 8 is performed by Hans Schrijver/ SRON.

One example for additional dead or bad pixels is shown in Figure 8 below. Hardware changes between OPTEC2 and OPTEC5, the shim exchange to improve the slit function in the NIR channels, affects the data as expected.

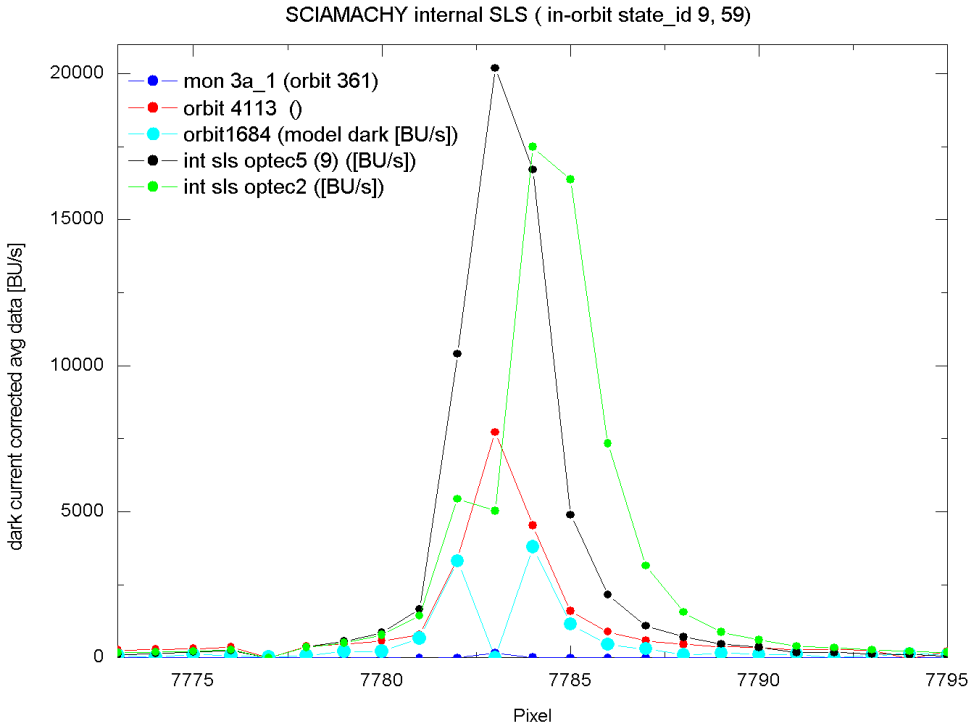

Figure 8 Example for additional bad pixels in channels 7/ 8 here shown for pixel 7783 in channel 8. In **green** the raw data from OPTEC2, in **black** from OPTEC5 after the shim exchange. Hardly visible in **blue** the data from an early SODAP measurement before the SRC release and cooling of the NIR channels. During orbital 1684 data (**cyan**) pixel 7783 seems to be dead, during the internal SLS measurement performed in orbit 4113 shown in **red** signal is again measurement at this pixel.

5.1.2 Best fit per channel

Looking at the fitting quality parameters (CHI squared, CHI squared reduced) a recommendation of the best fitting algorithm is given per channel in the following table [see Table 4] using the PtCrNe lamp as spectral line source. The previous results from the on-ground phases are also listed [see RD01 for OPTEC2 and RD02 for OPTEC5]. The preferred function is optimal for most lines within a channel, not necessarily for all lines. For the slit function suggested the simplicity of the algorithm is taken into account. This means for example if the Voigt fit leads to nearly the same result as a Gaussian, the latter will be preferred. Depending on the fit used the resulting spectral resolution varies.

The results are expected to be possibly different from the on-ground reported results, which are based on an *external SLS* (s-polarised). The *internal SLS* faces a blocking of the optical beam by the elevation scan mirror housing resulting in a partial blocking of the aperture and/ or the field of view as compared to the external observations. The SLS blocking shift related to the wavelength calibration between the on-ground measured internal SLS and external SLS results are part of the key data [see also RD01 and RD18].

Table 4 Best fitting slit function recommendations per channel for the *external* s-polarised PtCrNe *SLS* measurement from OPTEC2 [see RD01] and OPTEC5 [see RD02] slit function results and the in-flight results for orbit 1684 measured with the *internal SLS*.

CH	Best slit function		
	s-pol ext SLS		int SLS
	OPTEC2	OPTEC5	Orbit 1684
1	simple hyperbolic	simple hyperbolic	**simple hyperbolic**
2	simple hyperbolic	simple hyperbolic	**Gaussian**
3	simple hyperbolic	simple hyperbolic	**simple hyperbolic**
4	simple hyperbolic	Gaussian	**Gaussian**
5	simple hyperbolic	Gaussian	**simple hyperbolic**
6	Gaussian	Gaussian	**Gaussian**
7	simple hyperbolic	simple hyperbolic	**(compound hyperbolic from the available lines)**
8	compound hyperbolic	compound hyperbolic	**(compound hyperbolic from the available lines)**

In channel 2 the Gaussian algorithm is recommended for the in-flight measurement in orbit 1684 versus the simple hyperbolic function during OPTEC5. The recommendations for channels 7 and 8 are in brackets due to a lack of spectral lines and therefore not sufficient information.

The FWHM in pixels for the in-flight data from orbit 1642 and the *internal SLS* from OPTEC5 results as well as the key data values based on the *external s-polarised SLS* are listed in the Annex 2.1 (as example for the Gaussian and simple hyperbolic algorithms).

In the following figures the differences of the FWHM results are visualised. Firstly the difference between the on-ground *external* s-polarised measured *SLS* and *internal SLS* (in **black** Gaussian algorithm results, in **blue** simple hyperbolic FWHM results in pixels). Secondly the comparisons of the in orbit 1642 retrieved *internal SLS* measurement data with the *internal on-ground SLS* data are shown (in **red** the Gaussian algorithm results and in **cyan** the simple hyperbolic FWHM results). Per channel the recommended algorithms are shown.

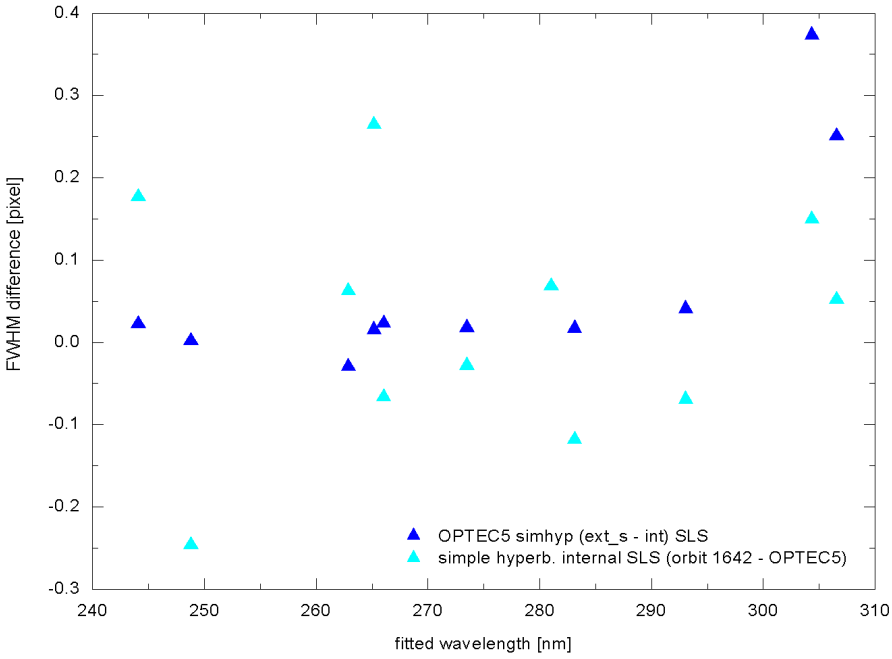

Figure 9 **Channel 1** difference in FWHM results in pixels between the best suggested channel fit (simple hyperbolic algorithm [see Table 4]) of the key data (*external* s-pol *SLS* msm, OPTEC5) and the *internal SLS* during OPTEC5 in **blue,** and the difference between the in-flight fit in orbit 1642 and the *internal SLS* from OPTEC5 in **cyan**. The FWHM results between the external and internal OPTEC5 results differ less than the results between the *internal SLS* in-flight and on-ground [see for results Annex 2.1].

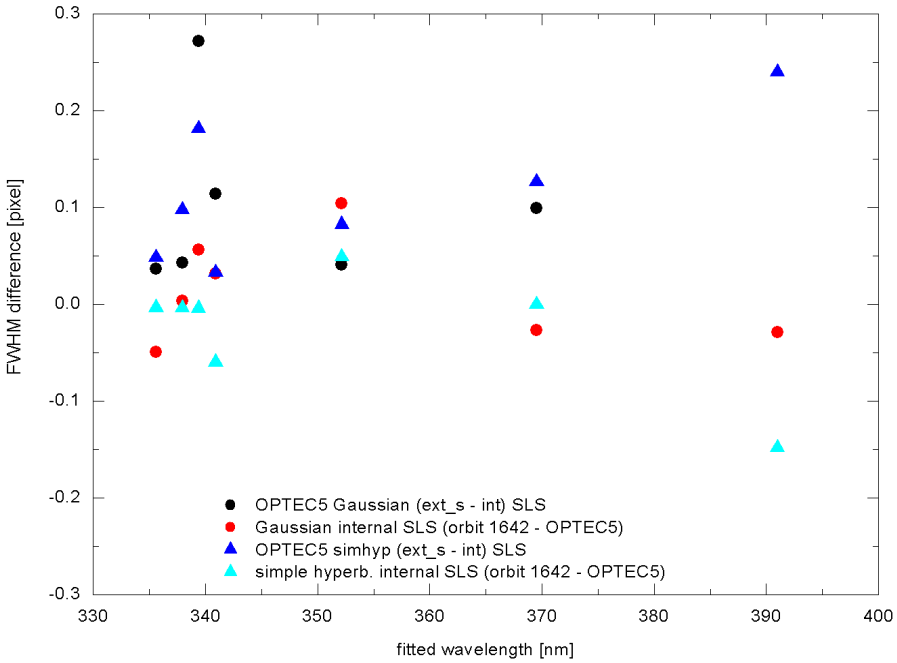

Figure 10 **Channel 2** differences of FWHM results in pixels. The simple hyperbolic algorithm suggested for the key data and the Gaussian for the orbit 1642 data. FWHM result differences between the key data (*external* s-pol *SLS* msm) and *internal SLS* during OPTEC5 in **black** (Gaussian); **blue** (simple hyperbolic). The in-flight fit of orbit 1642 data difference with the *internal SLS* from OPTEC5 in **red** (Gaussian) and **cyan** (simple hyperbolic) [see for results Annex 2.1].

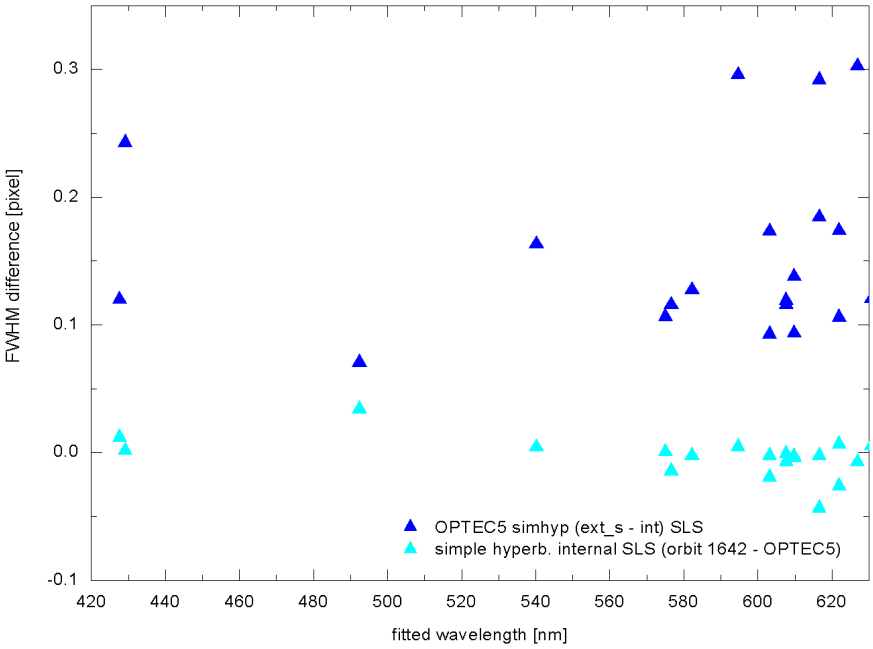

Figure 11 **Channel 3** difference in FWHM results in pixels between the best suggested channel fit (simple hyperbolic algorithm) of the key data (*external* s-pol *SLS* msm, OPTEC5) and the *internal SLS* during OPTEC5 in **blue** and the in-flight fit in orbit 1642 with the *internal SLS* from OPTEC5 in **cyan** [see for results Annex 2.1].

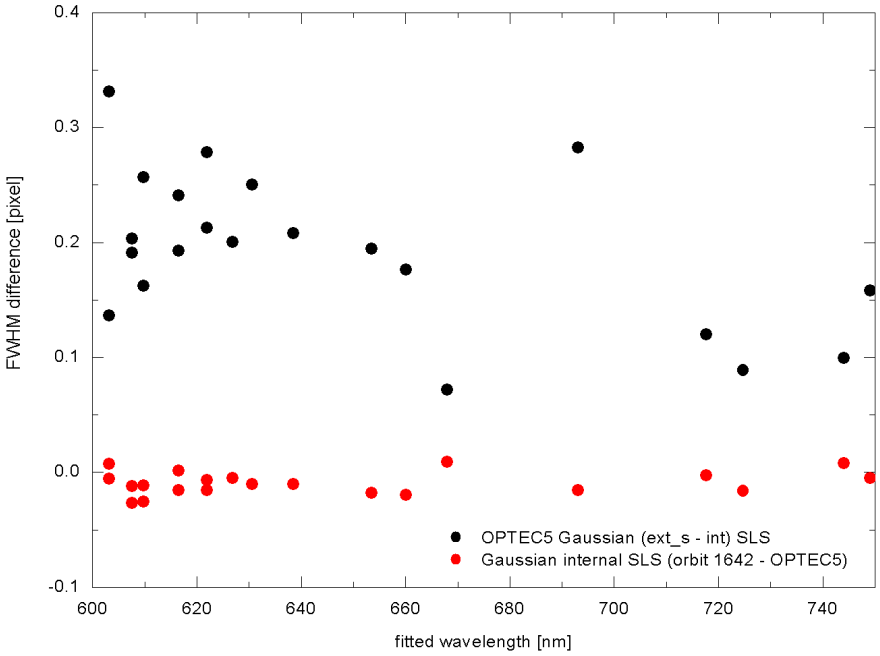

Figure 12 **Channel 4** difference in FWHM results in pixels between the best suggested channel fit (Gaussian algorithm) of the key data (*external* s-pol *SLS* msm, OPTEC5) and the *internal SLS* during OPTEC5 in **black** and the in-flight fit in orbit 1642 with the *internal SLS* from OPTEC5 in **red** [see for results Annex 2.1].

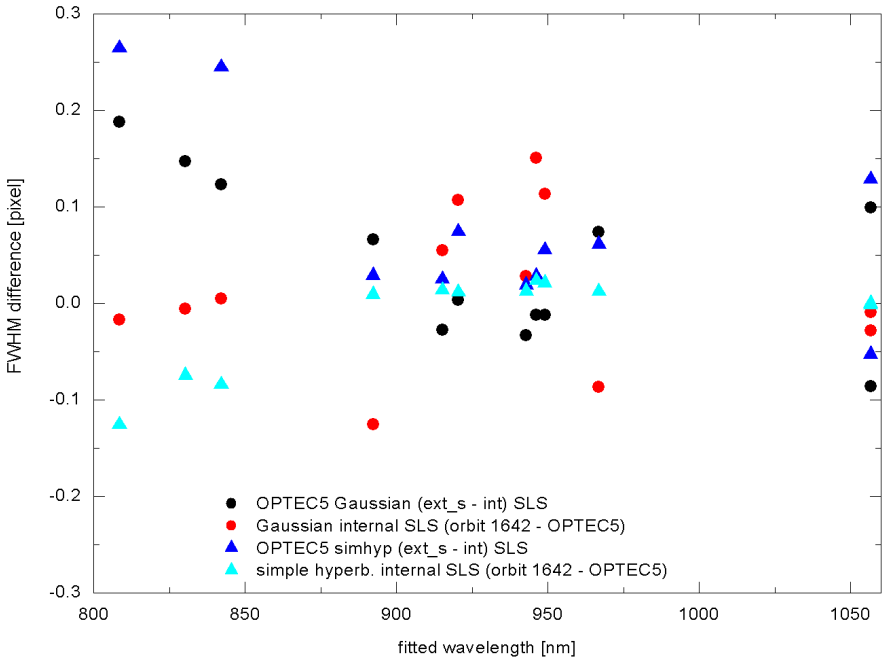

Figure 13 **Channel 5** differences of FWHM results in pixels. The simple hyperbolic algorithm suggested for the key data and the Gaussian for the orbit 1642 data. FWHM result differences between the key data (*external* s-pol *SLS* msm) and *internal SLS* during OPTEC5 in **black** (Gaussian); **blue** (simple hyperbolic). The in-flight fit of orbit 1642 data difference with the *internal SLS* from OPTEC5 in **red** (Gaussian) and **cyan** (simple hyperbolic) [see for results Annex 2.1].

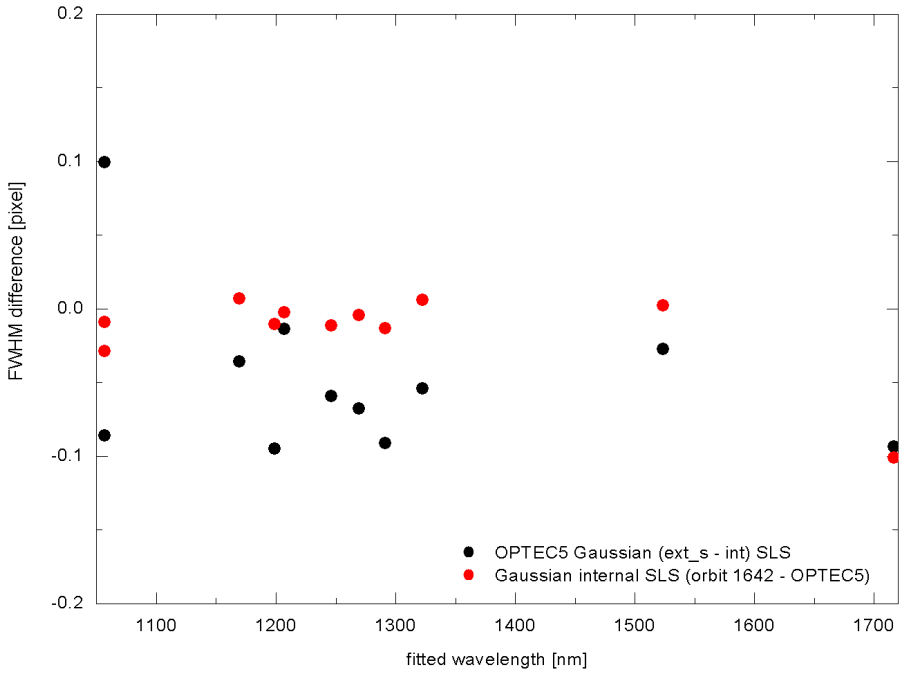

Figure 14 **Channel 6** difference in FWHM results in pixels between the best suggested channel fit (Gaussian algorithm) of the key data (*external* s-pol *SLS* msm, OPTEC5) and the *internal SLS* during OPTEC5 in **black** and the in-flight fit in orbit 1642 with the *internal SLS* from OPTEC5 in **red** [see for results Annex 2.1].

Except for channel 1 the simple hyperbolic algorithm for the *internal* on-ground and in-flight FWHM results are more similar than for the on-ground measured *internal* and *external SLS* FWHM results. The Gaussian FWHM fit results in channels 4 and 6 are also more similar for the two *internal SLS* measurements than for the *external* and *internal SLS* on-ground results.

5.2 Sun measurements

The Fraunhofer lines are listed in the Annex 3. The first list of wavelengths originates from the key data supplied by Sander Slijkhuis/ DLR. The key data lists ambient parameters. To be comparable with the wavelength calibration based on vacuum literature values of the SLS emission lines the key data is transformed to vacuum wavelengths with the help of the NIST absorption line database. The identification of the lines on SCIA measured solar data has been performed with the help of the first zenith sky measurements from the delta-PI period on-ground.

Some of the pre-selected Fraunhofer lines from the key data are not used. One example is shown in Figure 15 for the Na I line in channel 3 (key data 588.9973 nm, ambient wavelength). A blend of two lines (indicated by the red arrows) is visible in the SCIA spectra; therefore the line is not used. The corrected and normalised spectra in binary units per second (BU/s) of in-flight sun observation measurements is linked to the y-axis scale on the left. In **black** the state_ID 51 *SO&C-pointing* is visualised; in **red** the *sub-solar-calibration-pointing* (state_ID 53) and in **blue** the *sun-over-ESM-diffuser-calibration* measurement (state_ID 62).

The on-ground zenith sky measurements shown in **green** is linked to the right y-axis scale with far lower signal values in BU per second. The other Fraunhofer line positions can be found in the Annex 3.1.

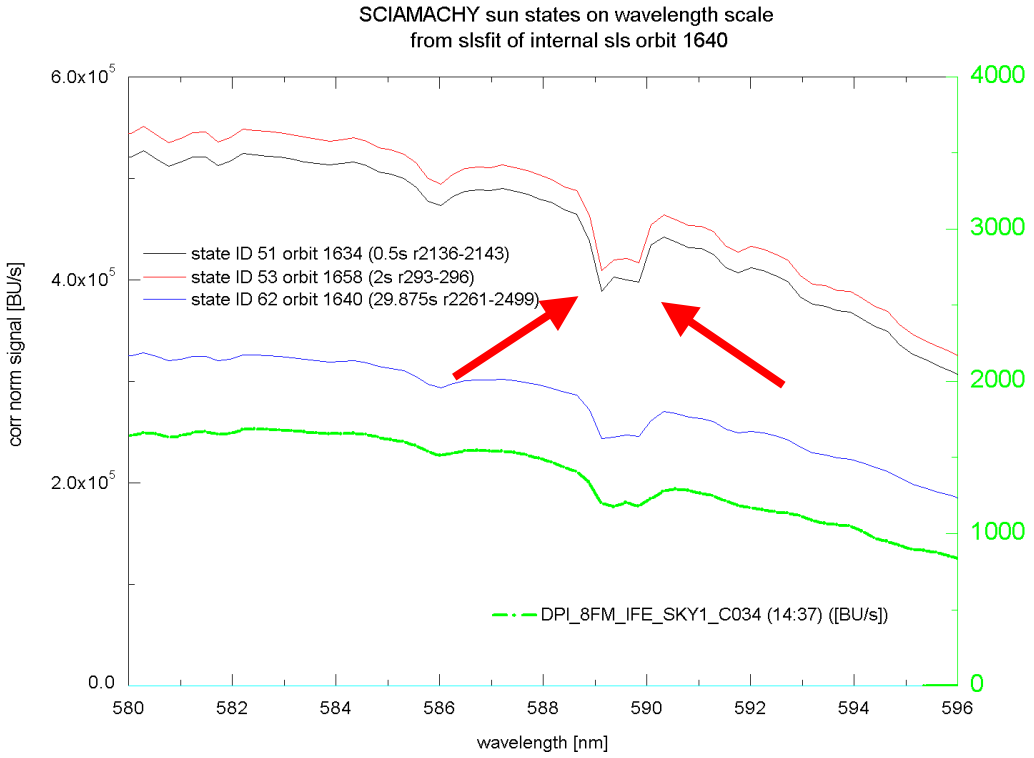

Figure 15 Double line visible in in-flight sun observation spectra and on-ground zenith sky measurement. Corrected spectra of in-flight sun observation measurements (left y-axis scale, **black**: state_ID 51, **red**: state_ID 53, **blue**: state_ID 62) and on-ground zenith sky measurements shown in **green** (right y-axis scale) with far lower signal values in BU/s.

For the relative comparison of the sun spectra used in this work, the Gaussian algorithm has been used. It is not the intention of this work to derive absolute data on the Fraunhofer lines. The Gaussian algorithm is only used to compare the full width at half maximum (FWHM) of observed lines with each other relatively. The Doppler effect, as described in the ATBD [see RD11] for level 1b to level 2 processing, has not been corrected for in the *sun-occultation-and-calibration-pointing* and *sun-over-ESM-diffuser-calibration* states used. It will affect the higher wavelengths (blue-shifted), but the wavelengths investigated in this work - covered by channels 1 to 5 - are to be not significantly affected by not correcting for the Doppler shift. For these channels the Doppler shift effect is smaller than the accuracy of the intended comparison. The maximum Doppler shift in channel 8 for solar spectra is 0.047 nm with an annual variation of up to ± 9 percent. The *sub-solar-calibration-pointing* measurements are not affected by a Doppler shift.

5.2.1 Different types of sun observations

The three used measurement types:

- *sun-occultation-and-calibration-pointing* measurement (SO&C, state_ID 51) via the limb port over the two mirrors (ASM- and ESM-mirror). SO&C window starts at sunrise to sun above atmosphere;
- *sub-solar-calibration-pointing* (state_ID 53) via the sub-solar port over the ESM mirror and
- *sun-via-ESM-diffuser-calibration* via the limb port, azimuth scan mechanism (ASM) mirror and elevation scan mechanism (ESM) diffuser with the neutral density filter (NDF) to reduce the light detected by channels 3 to 6 with a factor of about 5 (state_ID 62);

will be described in the following.

5.2.1.1 Sun-occultation-and-calibration-pointing (SO&C-pointing, state_ID 51)

During this measurement [see also description on SOST web page R09] using the limb configuration the sun is observed as schematically shown in Figure 16. The SO&C window starts at sunrise (phase 1: start phase - with calculation/ acquisition of sunrise position for ASM and 17.2 km height for ESM; phase 2 - ESM scanning at 17.2 km and ASM following sun track) and ends when the sun is above the earth's atmosphere (phase 5: ESM also pointing to the sun as the ASM and both mirrors track the sun centre until the sun is observed above the atmosphere).

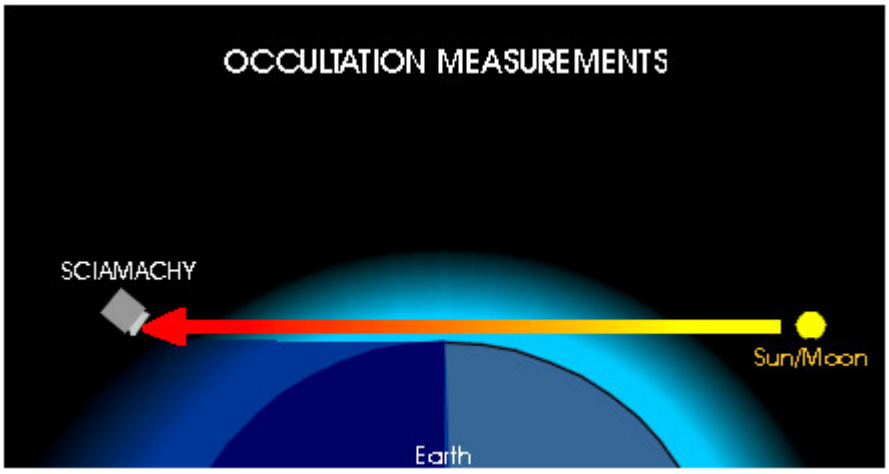

Figure 16 Schematic set-up for the solar occultation measurement (fig. SOST-IFE).

Conform the measurement description the final phase 5 - pointing to the sun – shall provide several seconds of measurement time above the atmosphere. For the analysis records 2136 to 2143 (the last half second) are used and are shown in the following figure.

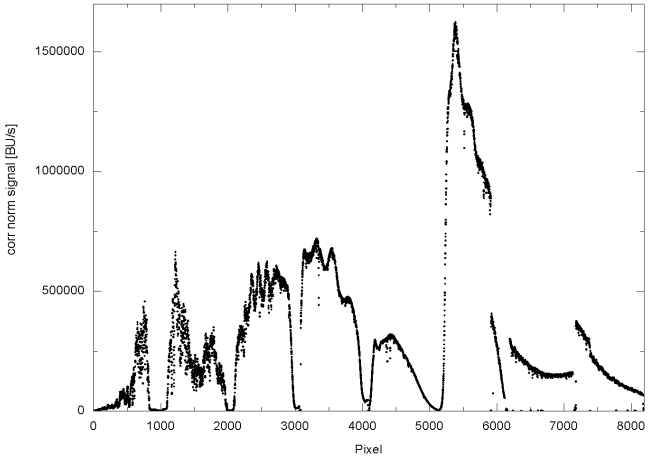

Figure 17 Corrected and normalised *SO&C-pointing* measurement data (state_ID 51) observed in orbit 1634 in BU per second averaged over records 2136 to 2143 (phase 5).

Different averages of the measured state over 0.5, 5, 16 and 64 seconds are compared [see Figure 18], normalised to the last record (2143) of 1/16th second. The average over 64 seconds includes measurements through the earth's atmosphere and scans over the sun which explain the major offset to the other ratios. The ratios with the averaged over 0.5, 5 and 16 seconds are supposed to be performed in the last phase 5 of the state pointing at the sun above the atmosphere. Remarkable is the signal decrease in channel 1 of about 30 percent in the comparison of the average over the total last phase pointing at the sun above the atmosphere and the last record (2143) within this phase.

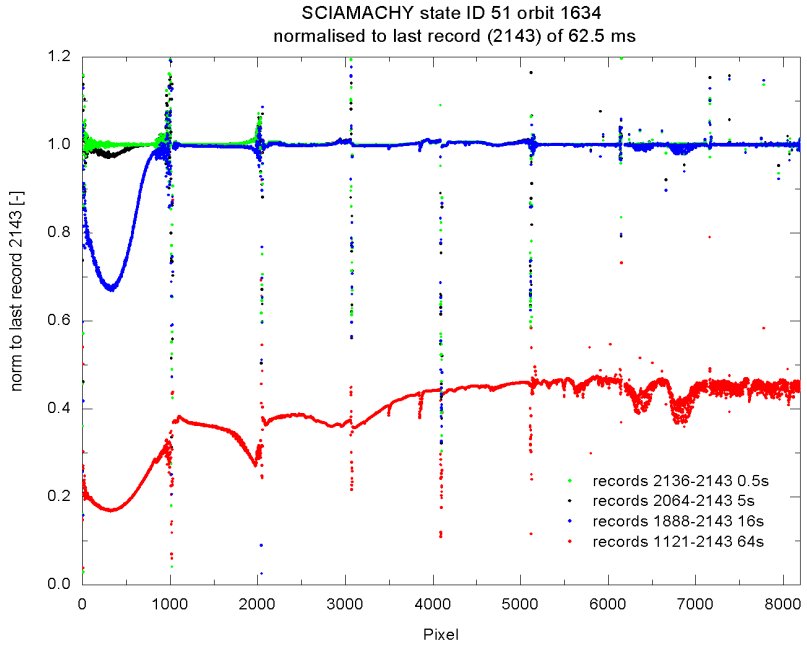

Figure 18 Normalisation to last record (r2143, 62.5 ms) of several averages of the *SO&C-pointing* measurement. In **green** the ratio of the average of 0.5 s, in **black** 5 s, in **blue** 16s (the last phase of the state, sun above earth's atmosphere) and in **red** the complete state execution including observation of the sun through the earth's atmosphere.

A zoom of the previous graph reveals the feature of the oxygen A-band around pixel 3850 that still appears in the last five seconds average. This also explains the signal difference in the UV through atmospheric absorption. Only the last 0.5 seconds seem to be measured above the earth's atmosphere and will be used for further analysis. This is not according to the measurement parameter definition where several seconds of sun above earth's atmosphere were expected [see R09].

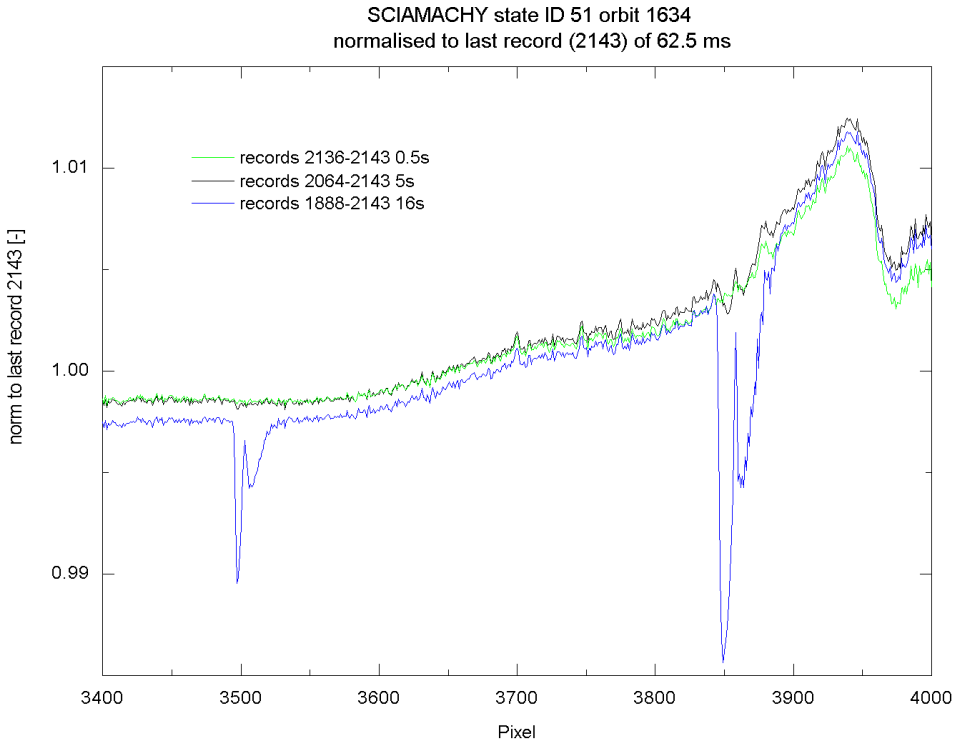

Figure 19 Zoom of Figure 18. Visible oxygen A-band around pixel 3850 in averages of last 5 (in **black**) and 16 s (in **blue**). While during the last phase 5 of the state the measurements should be performed above the earth's atmosphere, this absorption line reveals it is still measured through the atmosphere, which also explains the absorption in the UV [see Figure 18].

5.2.1.2 Sub-solar-calibration-pointing (state_ID 53)

Average of records 281 to 323 (21.5 s) over all four phases (except the first record due to MEC) of the state execution and 293 to 296 (2 s) of phase 3, when the ESM acquires the sun with the sun follower (SFS) centring the slit (0.045°) on the sun, are shown in Figure 20. Phase 3 is supposed to measure over six seconds. The signal decreases after two seconds. Therefore the average of two seconds with the highest signal levels is used with an average ESM angle of 56.906 degrees from phase 3. The sub solar measurements are influenced/ affected by the so-called 'guillotine-effect' due to an interfering bracket and two layers of MLI as discovered by Manfred Gottwald/ DLR and reported in the on-ground AIT results [see RD10]. In the same reference it is reported to be the case for ESM angles below 55.72 degrees. Since the ESM angle is larger for the raw data used, the decrease of the signal in phase 3 can't be explained by the 'guillotine-effect'. The reason for the decrease of the signal in this phase is at the present time not known. In 'Technical Note on the evaluation of the subsolar pointing state ID 53 w.r.t. centre position in subsolar window and signal shape, SCIAMACHY Azimuth alignment_TecNote, SSCP signal analysis 1 December 2003' by E. Krieg/ DLR-IMF an observed azimuth position jump is mentioned.

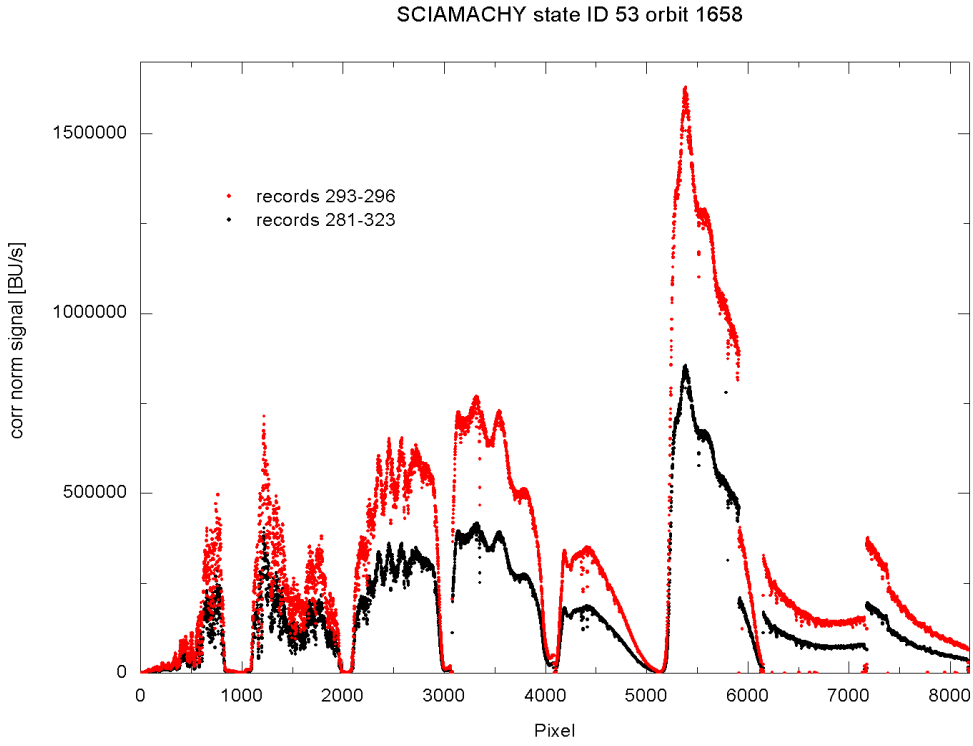

Figure 20 Corrected and normalised *sub-solar-calibration-pointing* measurement data (state_ID 53) observed in orbit 1658 in BU per second. In **red** the first two seconds averaged from phase 3, in **black** the average of all records.

5.2.1.3 Sun-over-ESM-diffuser-calibration with NDF (state_ID 62)

The measurement concept has been described in the 'Sun-over-ESM-diffuser incl. ESM angle variation – in-flight' [see RD12]. Spectral features that originate from the ESM diffuser are investigated in that report. For the present analysis the data has been averaged over the whole state (orbit 1640, records 2261 to 2499, except first record 2260 due to MEC). The analysis of sun-over-ASM-diffuser measurements is part of other objectives performed by other parties.

5.2.2 In-flight sun measurement analysis result comparison

In Figure 21 the previously described sun observing spectra are shown. All these measurements are performed with the NDF in the light path (the spectra are not corrected for the NDF transmission!). The wavelength calibration, analysed as amongst others described in RD15, is performed with the *internal SLS* measurement in orbit 1642.

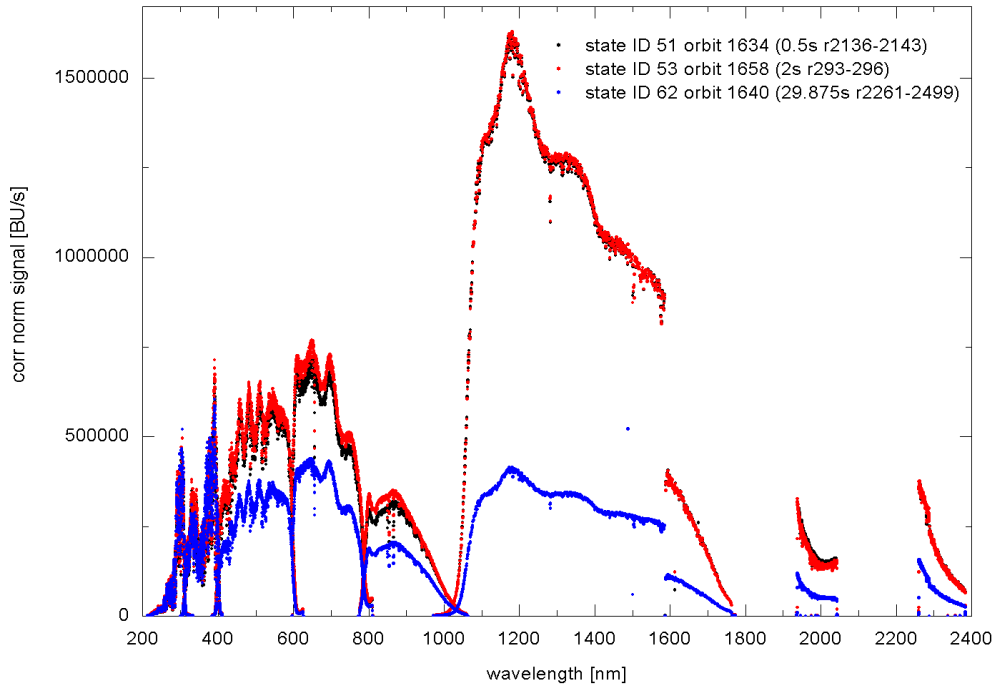

Figure 21 Observed sun spectra used. In **black** last 0.5 s of the *SO&C-pointing* msm, in **red** the last 2 s *sub-solar-calibration-pointing* spectra of orbit 1658 and in **blue** the *sun-over-ESM-diffuser-calibration* msm performed in orbit 1640. The spectra are plotted on a wavelength scale retrieved with the help of the *internal SLS* measurement performed in orbit 1642.

One of the major differences between the *SO&C-pointing* measurement (state_ID 51) shown in **black** in the previous graph and the in **red** shown *sub-solar-calibration-pointing* (state_ID 53) are the viewing directions and viewing ports. While the latter is performed via the ESM-mirror looking via the sub-solar port in anti-flight direction towards the sun, the *SO&C-pointing* observation uses the limb port looking in flight direction of ENVISAT using the ASM-mirror as well. At least absorption from the second mirror is expected to result in lower signals.

The *sun-over-ESM-diffuser-calibration* state (state_ID 62) shown in **blue** shows far lower intensities in channels 3 to 8. In the limb configuration the sun is observed via the ASM-mirror and the ESM-diffuser. For this measurement the large aperture is used, while the other two measurements are performed with the small aperture.

Ratios between the spectra shown in Figure 21 are visualised in Figure 22 for a general impression of the differences in spectra amongst others due to the aforementioned differences in observation.

The upper **red** dots represent the ratio of the *sub-solar-calibration-pointing* observation divided by the *SO&C-pointing* observation (state_ID 53 / state_ID 51). Channels 1 and 2 show a difference of around 10 percent, channels 3 and 4 a little less and in channel 5 the signal differences drop from about 15 percent to zero.

The **blue** dots show the ratio between the *sun-via-ESM-diffuser-calibration* and the *SO&C-pointing* spectra (state_ID 62 / state_ID 51). The signals in channel 1 and 2 show a smaller offset then in channels 3 to 5. Those again a smaller offset then in channels 6 to 8. Wiggles are visible with reduced frequency up to the end of channel 5. The slit function for these two compared states is different due to the use of the small and large aperture. Spectral features from the ESM-diffuser influence the results. The IT is different in channels 3 to 6 and 8 for state 51, and in channels 3 and 6 for state 53 to the other channels. Possibly different parts of the sun are observed. The mentioned points shall just give a short overview of possible reasons. Investigating this more intensively is beyond the scope of this particular work.

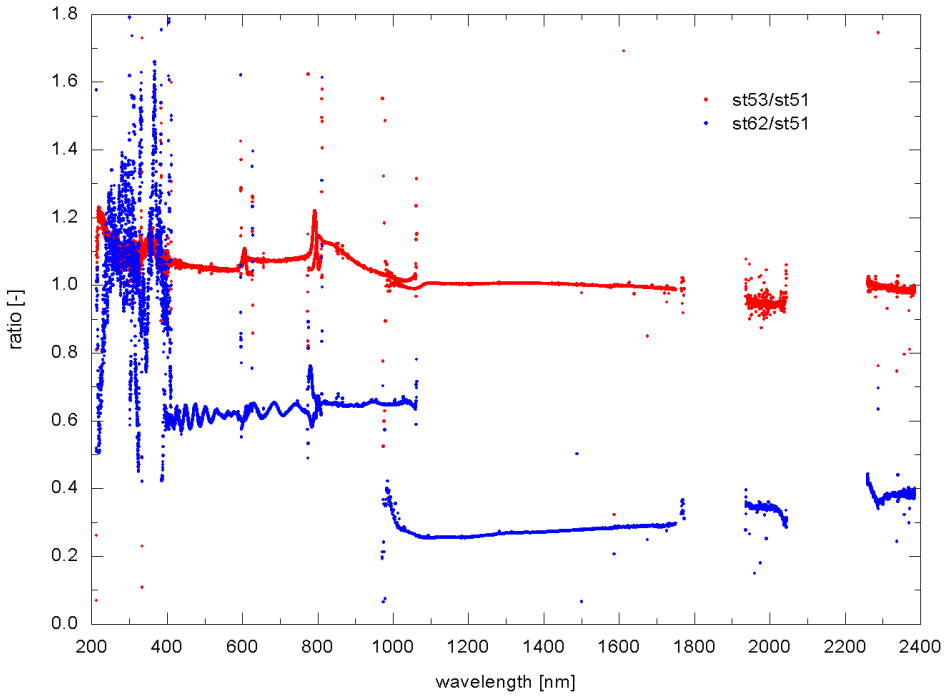

Figure 22 The upper **red** dots represent the ratio of the *sub-solar-calibration-pointing* observation divided by the *SO&C-pointing* observation of the previous Figure 21 (state_ID 53 / state_ID 51). The **blue** dots are the ratio of the *sun-via-ESM-diffuser* and the *SO&C-pointing spectra* (state_ID 62 / state_ID 51).

Since no Doppler effect correction has been performed on the relevant data the ratio in the NIR wavelength area (channels 6 to 8) have to be interpreted considering this. For the overall impression the influence is negligible and on the scale of Figure 22 this effect is anyhow not visible.

Channel dependent apertures as documented in the OPTEC cold test performance report [see RD16] influence the results. Channels 1 and 2 (~ 7.5 cm^2) have by design a factor 2 larger aperture than channels 3 to 5. Channel 6 has the smallest aperture with about 1.4 cm^2 and channels 7 and 8 have an aperture of about half the size of channels 3 to 5.

The next two graphs show the calculated ‘design’ curve and measured curve from RD16 (large aperture configuration divided by small aperture configuration) and the ratio between the in-flight measured and previously discussed state_ID 62 with the large aperture and ESM-diffuser and the state_ID 51 with the small aperture measured via the two mirrors (both in limb configuration). In both ratios similar wiggles are visible and the jump between channels 5 and 6 around 1000 nanometres is in

both cases around factor three. For a better comparison the in-flight data [see Figure 24] could in addition be corrected by the adequate ESM-mirror / -diffuser correction factor taking also into account the small and large instrument aperture (channel dependent, from objective 11 for large aperture factor ~1000 to 1600, see RD14).

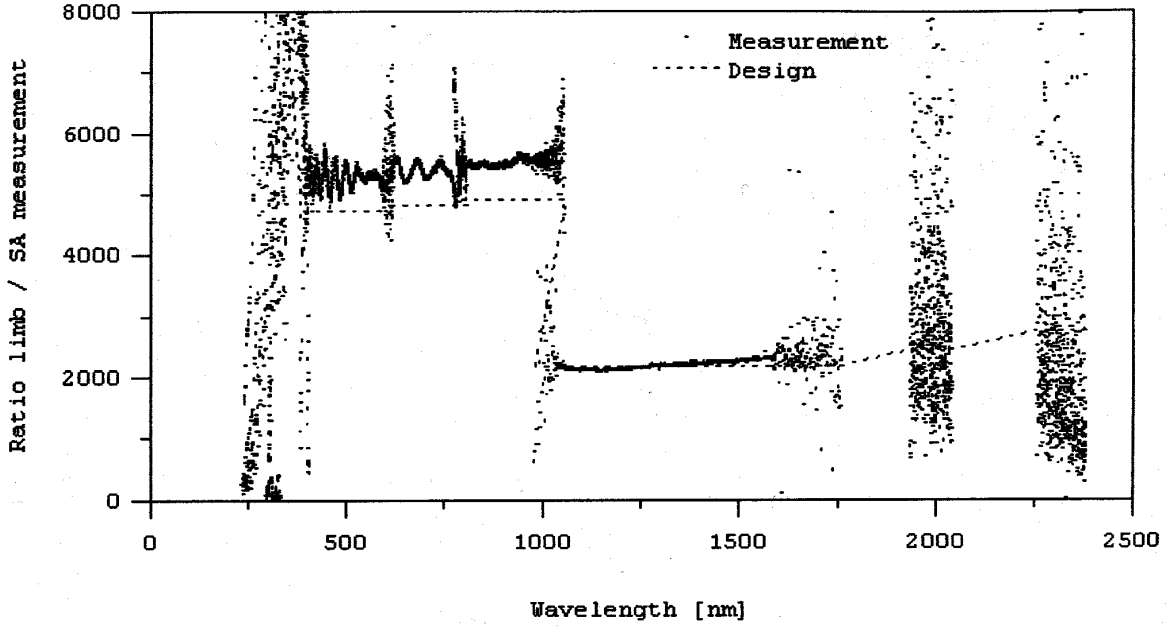

Figure 17 Ratio of measurement in limb and limb with small aperture modes

Figure 23 Figure from RD16 of the OPTEC cold test performance result of the large divided by small aperture results via limb.

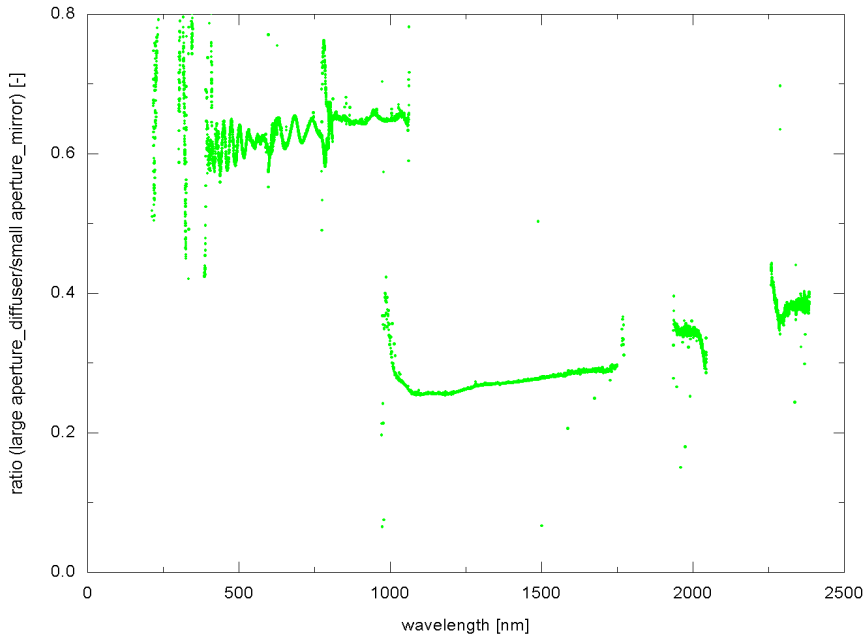

Figure 24 In-flight ratio of state_ID 62 with the large aperture via ESM-diffuser and state_ID 51 with the small aperture via two mirrors (not corrected for mirror/ diffuser).

5.2.2.1 Line fits

Per channel example lines are shown for the different in-flight sun observations described in the previous chapters. The *SO&C-pointing* (state_ID 51) spectrum from orbit 1634 is **black**; the *sub-solar-calibration-pointing* (state_ID 53, orbit 1658) is illustrated in **red** and the *sun-over-ESM-diffuser* measurement from orbit 1640 (state_ID 62) in **blue**. The appropriate fits are visualised. A Gaussian algorithm is used for relative comparison of the results. Testing all the different functions on the observed spectra can retrieve better results. This is out of scope for this work. Comparisons of the Gaussian fit FWHM results normalised to *SO&C-pointing* (state_ID 51) results are given in the tables below each graph.

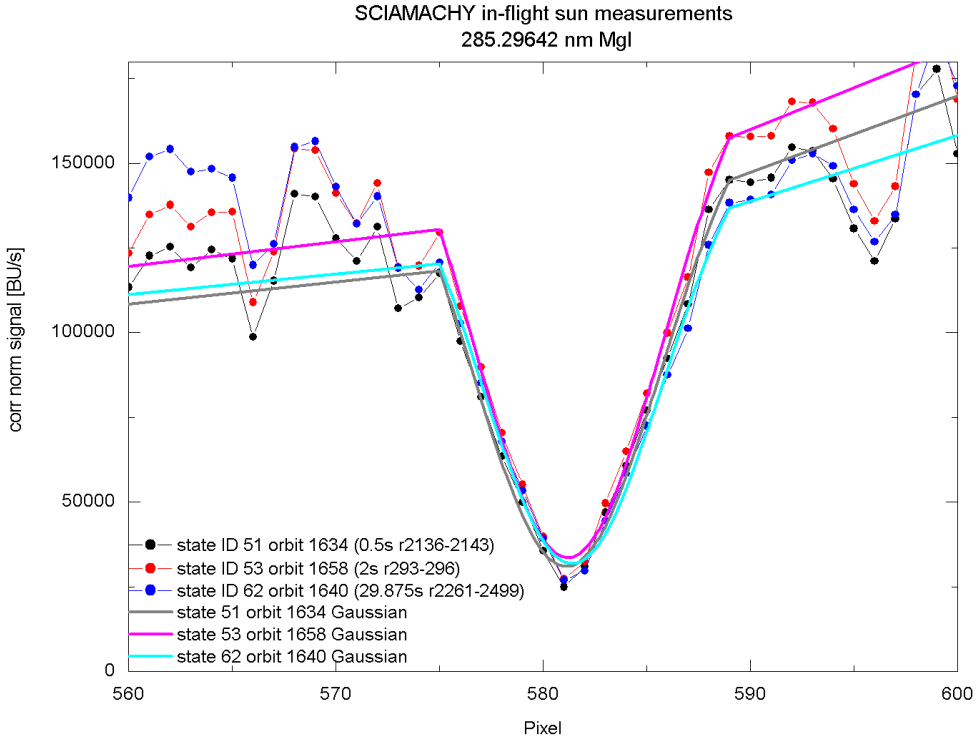

Figure 25 **Channel 1** example of an observed Fraunhofer line. The **Mg I** absorption line at **285.29642 nm** is visualised. Three different sun observation modes are shown (**black**: state_ID 51, **red**: state_ID 53, **blue**: state_ID 62) with the corresponding Gaussian fits (**grey**: state_ID 51, **magenta**: state_ID 53, **cyan**: state_ID 62).

Table 5 FWHM comparison of fitted Fraunhofer line in Figure 25 between the different sun observation states. For Fraunhofer lines see list in Annex 3.

Fitted line vacuum wavelength [nm]	FWHM (Gaussian) normalised to state_ID 51 results [-]		
	State_ID 51	State_ID 53	State_ID 62
285.29642	1	1.005	0.956

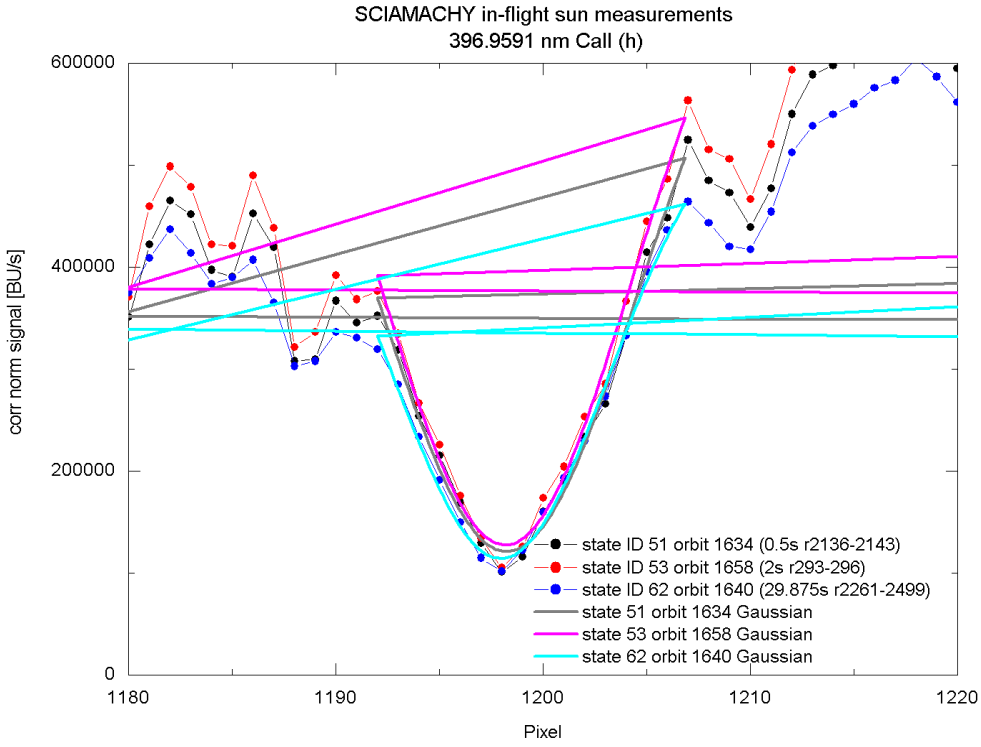

Figure 26 **Channel 2** example of an observed Fraunhofer line h. The **Ca II** absorption line at **396.9591 nm** is visualised (fitting lines crossing due to the opposite pixel/ wavelengths readout in this channel). Three different sun observation modes are shown (**black**: state_ID 51, **red**: state_ID 53, **blue**: state_ID 62) with the corresponding Gaussian fits (**grey**: state_ID 51, **magenta**: state_ID 53, **cyan**: state_ID 62).

Table 6 FWHM comparison of fitted Fraunhofer line in Figure 26 between the different sun observation states. For Fraunhofer lines see list in Annex 3.

Fitted line vacuum wavelength [nm]	FWHM (Gaussian) normalised to state_ID 51 results [-]		
	State_ID 51	State_ID 53	State_ID 62
396.9591	1	0.972	0.943

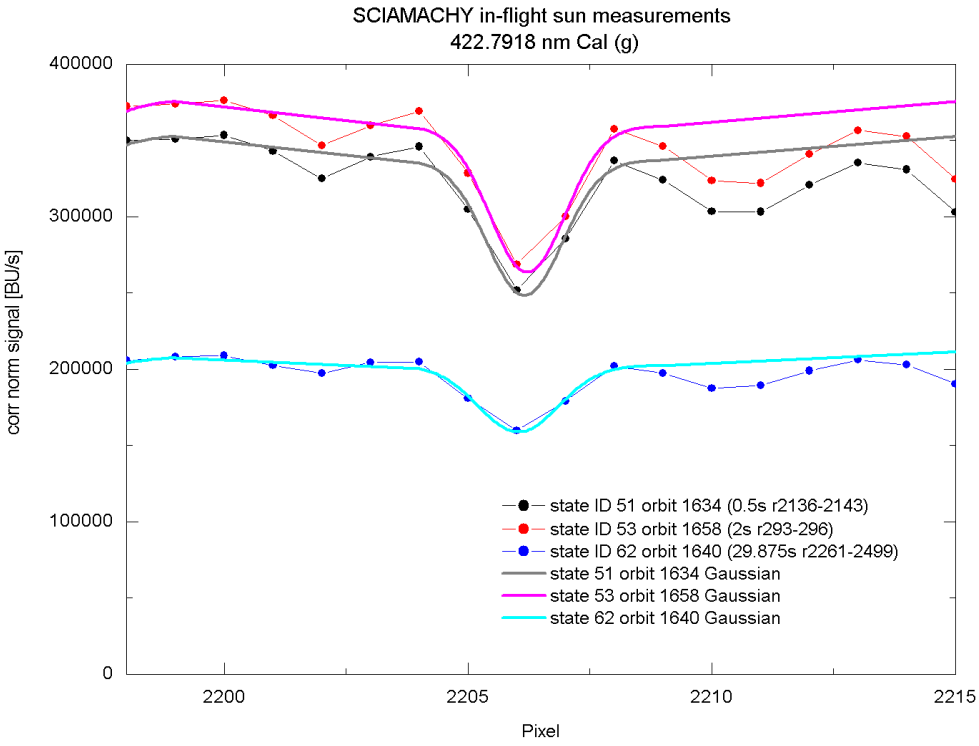

Figure 27 **Channel 3** example of an observed Fraunhofer line. The **Ca I** absorption line at **422.7918 nm** is visualised. Three different sun observation modes are shown (**black**: state_ID 51, **red**: state_ID 53, **blue**: state_ID 62) with the corresponding Gaussian fits (**grey**: state_ID 51, **magenta**: state_ID 53, **cyan**: state_ID 62).

Table 7 FWHM comparison of fitted Fraunhofer line in Figure 27 between the different sun observation states. For Fraunhofer lines see list in Annex 3.

Fitted line vacuum wavelength [nm]	FWHM (Gaussian) normalised to state_ID 51 results [-]		
	State_ID 51	State_ID 53	State_ID 62
422.7918	1	0.995	1.064

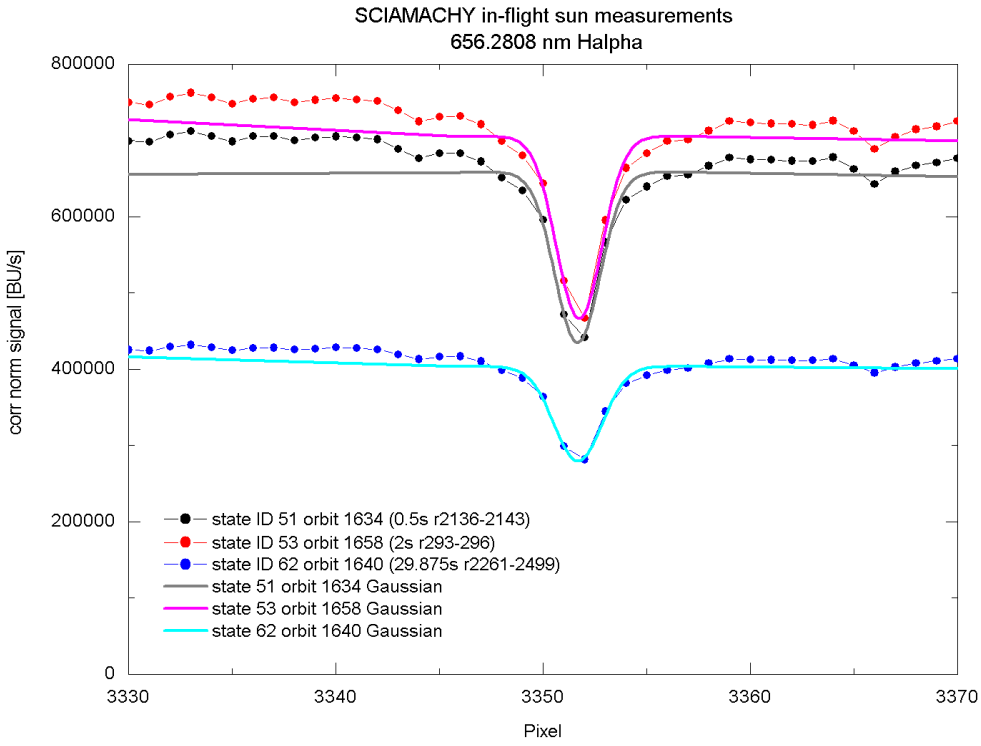

Figure 28 **Channel 4** example of an observed Fraunhofer line **H-alpha**. This absorption line at **656.2808 nm** is visualised. Three different sun observation modes are shown (**black**: state_ID 51, **red**: state_ID 53, **blue**: state_ID 62) with the corresponding Gaussian fits (**grey**: state_ID 51, **magenta**: state_ID 53, **cyan**: state_ID 62).

Table 8 FWHM comparison of fitted Fraunhofer line in Figure 28 between the different sun observation states. For Fraunhofer lines see list in Annex 3.

Fitted line vacuum wavelength [nm]	FWHM (Gaussian) normalised to state_ID 51 results [-]		
	State_ID 51	State_ID 53	State_ID 62
656.2808	1	1.011	1.074

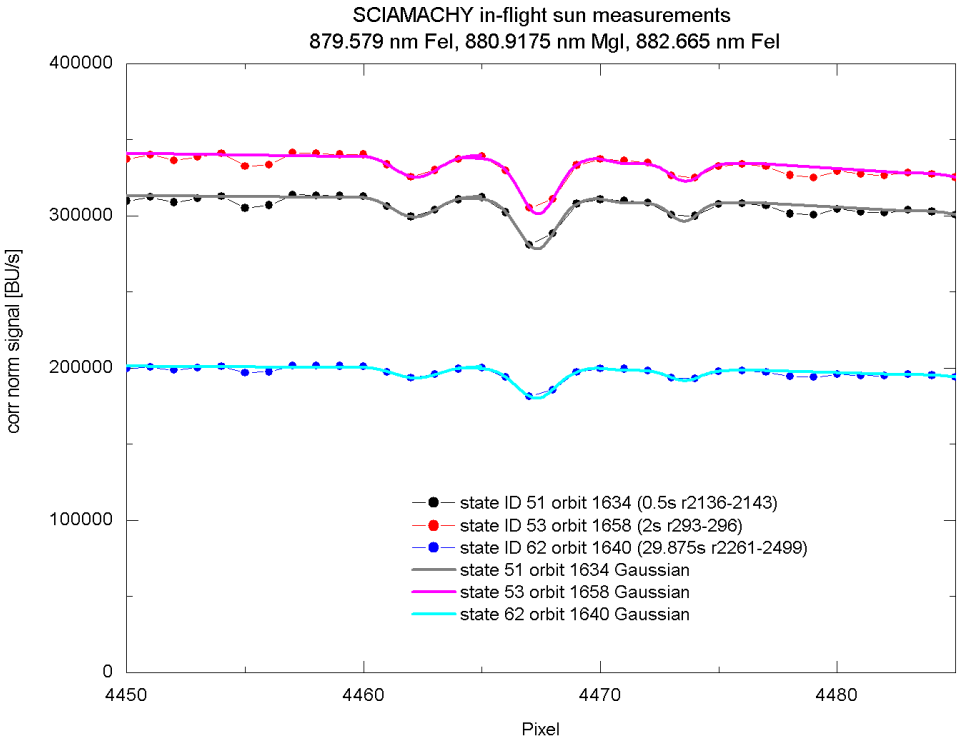

Figure 29 **Channel 5** example of observed Fraunhofer lines. The fits of **Fe I** and **Mg I** absorption lines at **879.579**, **880.9175** and **882.665 nm** are visualised. Three different sun observation modes are shown (**black**: state_ID 51, **red**: state_ID 53, **blue**: state_ID 62) with the corresponding Gaussian fits (**grey**: state_ID 51, **magenta**: state_ID 53, **cyan**: state_ID 62).

Table 9 FWHM comparison of fitted Fraunhofer line in Figure 29 between the different sun observation states. For Fraunhofer lines see list in Annex 3.

Fitted line vacuum wavelength [nm]	FWHM (Gaussian) normalised to state_ID 51 results [-]		
	State_ID 51	State_ID 53	State_ID 62
879.579	1	1.001	1.016
880.9175	1	0.982	1.042
882.665	1	1.139	1.130

A relative comparison between the FWHM results using the Gaussian algorithm for the in-flight sun measurements is shown below. Per fitted line the results are shown in Figure 30. The results from the *sun-over-ESM-diffuser-calibration* (state_ID 62) deviate the most from the other two sun measurements mainly due to the large aperture used in the light path. The FWHM of the Mg I line at 285 nanometres [see also fit in Figure 25] is quite large as well as the Ca II k line at 393 nanometres due to their wide absorption features.

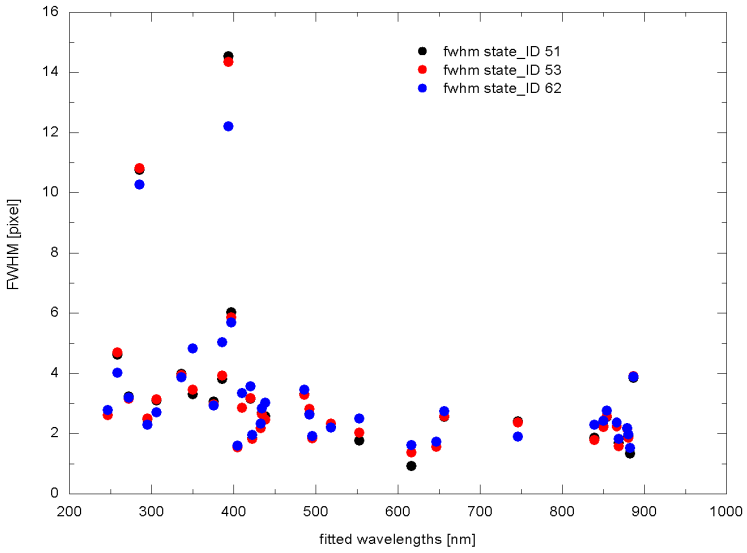

Figure 30 FWHM results using the Gaussian algorithm. *SO&C-pointing* (state_ID 51) in **black**, *sub-solar-calibration-pointing* (state_ID 53) in **red** and in **blue** the *sun-over-ESM-diffuser-calibration* results from state_ID 62.

Comparison between fits of the *SO&C-pointing* observation FWHM results and the *sub-solar-calibration-pointing* results from the previous graph. The results vary about plus minus five percent.

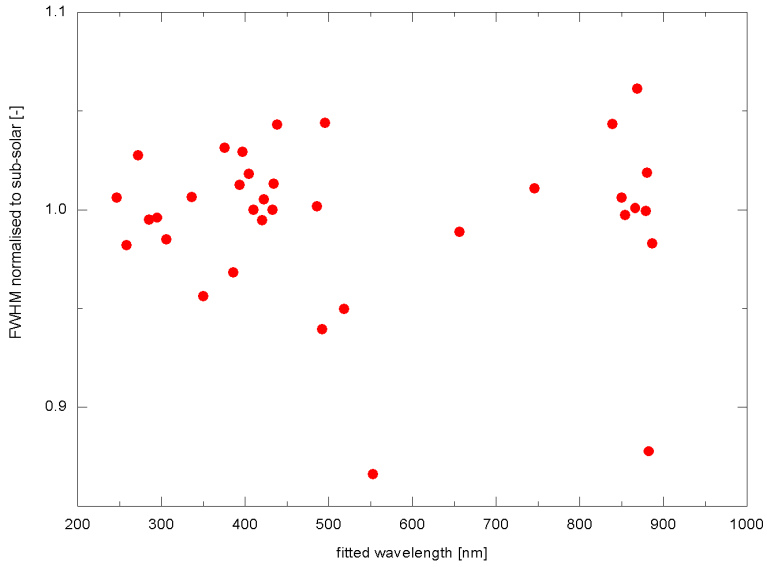

Figure 31 *SO&C-pointing* (state_ID 51) FWHM results ratioed to *sub-solar-calibration-pointing* (state_ID 53) FWHM results.

The pixel positions [see Figure 32] of the Gaussian fitted Fraunhofer lines show that the line positions of the *sub-solar-calibration-pointing* and the *SO&C-pointing* sun observations both performed with the small aperture are within 0.1 pixels. The shift in channel 2 is actually negative; due to the opposite read-out of the pixels versus wavelengths it appears positive in the graph. The differences of the line positions with the help of the fit of the *sun-over-ESM-diffuser-calibration* measurement with the large aperture are larger.

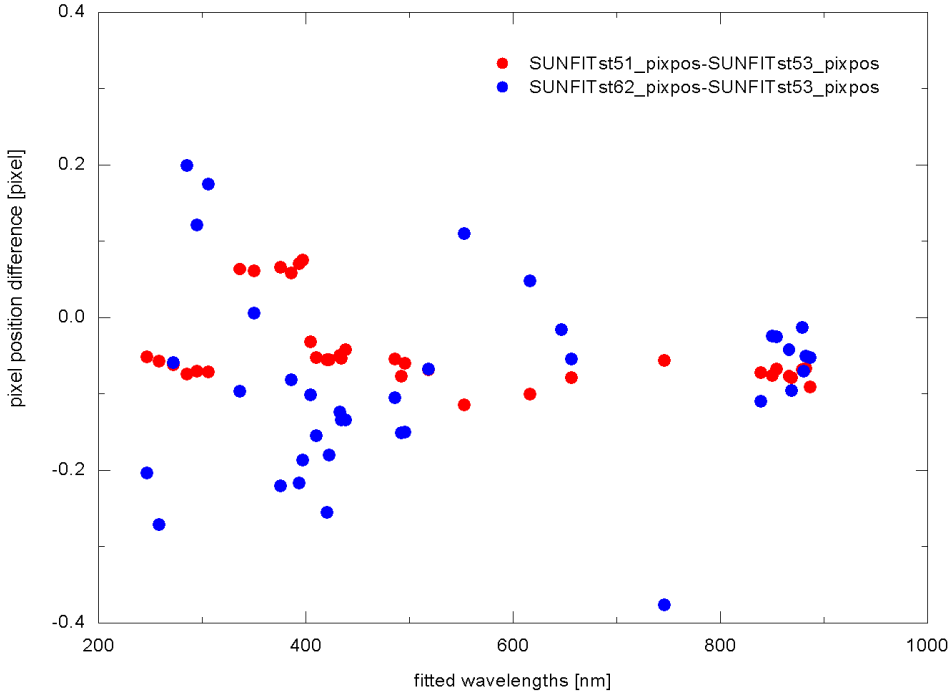

Figure 32 Pixel position comparison of fitted Fraunhofer lines between the different sun observations. The **red** dots represent the difference between the found positions of the *SO&C-pointing* to the *sub-solar-calibration-pointing* msm; the **blue** dots represent the difference of the *sun-over-ESM-diffuser-calibration* msm with the *sub-solar-calibration-pointing* results.

5.2.3 In-flight versus on-ground

Amongst others the following points have to be taken into account comparing results from on-ground to in-flight and measurements in-flight with reasonable time differences:

- The NDF transmission has changed with respect to the on-ground results as reported in RD13;
- ESM-diffuser/ -mirror degradation might both have independently changed as already mentioned in comparison with on-ground results in RD14;
- Stray light influences are not accounted for;
- Doppler shift influence for sun observations in channels 6 to 8 (in channels 1 to 5 the influence can be neglected for this relative comparison).

During the delta-PI phase of OPTEC2 in 1998/ 1999 at Schiphol zenith sky measurements have been performed. These measurements through the earth's atmosphere are plotted with the in-flight observations. The OPTEC2 wavelength scale is used for the on-ground observations. The wavelength calibration using the internal SLS measurement in orbit 1642 is used for the in-flight measurements.

As example the k (393.4777 nm) and h (396.9591 nm) Ca II lines in the overlap region of channels 2 and 3 are shown. The absorption line wavelengths are transferred to the vacuum wavelength and therefore slightly different from the values given in the key data by DLR. The on-ground spectrum shown in green corresponds to the y-axis on the right hand side; the scale on the left hand side represents the far higher measured signal values in-flight.

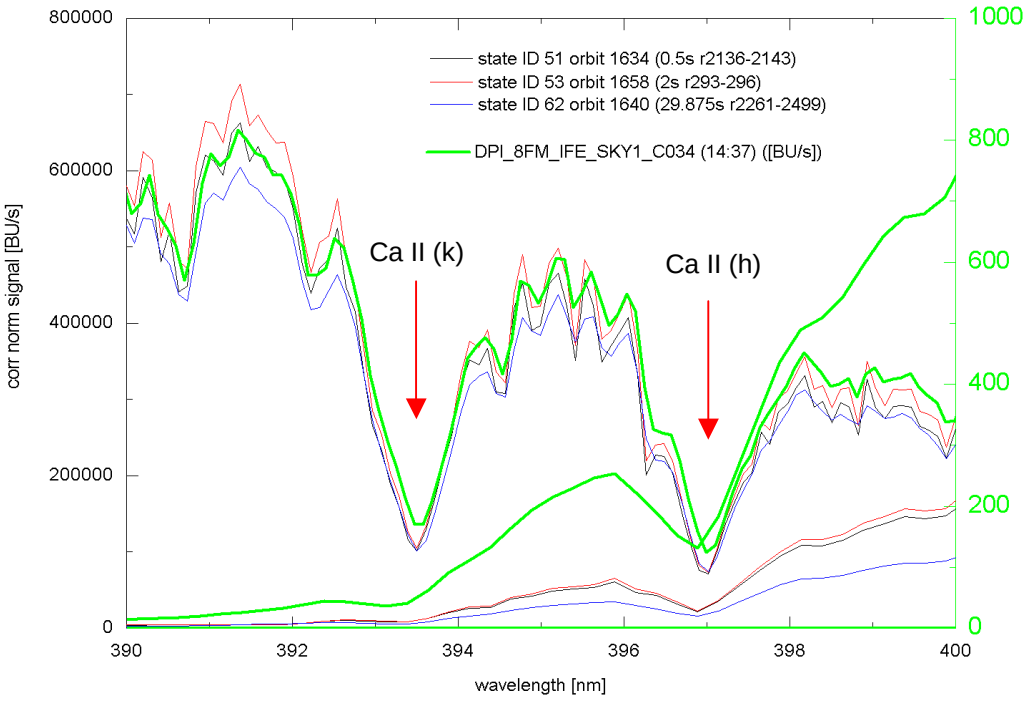

Figure 33 Corrected spectra of in-flight sun observation measurements (left y-axis scale) and on-ground zenith sky measurements shown in **green** (right y-axis scale). The overlap region of channels 2 and 3 is shown with the absorption features of the **k** and **h Ca II** lines at **393.4777** and **396.9591 nm**. The high similarity of the in-flight data and the about four years later observed in-flight spectra speaks for itself.

6. Conclusion

Slit functions have been determined from *internal spectral light source* (SLS) measurements with the help of emission lines and sun observations using Fraunhofer lines. The sun observations are performed with the small or large aperture, via the elevation scan mechanism –mirror or -diffuser. The measurements used for this investigation have been carefully selected from the switch on data acquisition phase, with as criterion the minimisation of possible influences of changes such as time, decontamination phases and contamination. The data is then memory effect and non-linearity corrected as well as dark signal corrected.

Direct comparison of slit functions retrieved from in-flight *SLS* with key data from on-ground *external SLS* measurements has to be performed with care since the *internal SLS* beam is blocked in the optical path by the elevation scan mirror housing. This leads to shifts as also delivered in the key data and possibly different slit function results, which have been shown in this report. The difference between the *internal* and *external* on-ground retrieved full width at half maximum results are compared per channel as well as the results from the *internal SLS* full width at half maximum from on-ground and in-flight data. Several algorithms have been tested to fit the literature vacuum wavelengths of the PtCrNe hallow cathode emission lines. A preferred algorithm is recommended per channel.

The Fraunhofer lines supplied in the key data are pre-selected with the help of an on-ground zenith sky measurement. Several lines had to be excluded and additional lines were identified. Three different sun observations with the neutral density filter in the light path are further investigated:

- The *sun-occultation–and-calibration-pointing* (state_ID 51) measurement through the limb port via the two mirrors with the window starting at sunrise and ending above the atmosphere. The small aperture is used. During the last phase of this measurement the sun has not been measured above the earth's atmosphere while several seconds were expected. Only the last half-second of the state shows no typical absorption feature of the earth's atmosphere (e.g. oxygen A-band).
- The *sub-solar-calibration-pointing* (state_ID 53) sun observation measured through the sub-solar port via the elevation scan mechanism (ESM) mirror using the small aperture. In phase 3 six seconds of sun pointing are planned, while only two seconds have similar signal heights in the investigated orbit. This cannot be explained with the previously on-ground reported 'guillotine-effect', since the angle setting is within the non-affected area.
- The *sun-over-ESM-diffuser-calibration* (state_ID 62) through the limb port via the azimuth scan mechanism mirror and ESM-diffuser using the large aperture.

The integration times of the *sun-occultation-and-calibration-pointing* and *sub-solar-calibration-pointing* measurements are not the same for all channels. This way the detectors are likely to measure different images/ scenery.

Comparisons between on-ground zenith sky measurements and in-flight sun observations show that the spectra are very stable over a time of almost four years.

Small and large aperture signal relation is comparable to on-ground investigations.

The full width at half maximum results are estimated for one orbit per sun observation and relatively compared with each other. The results in channels 1 to 6 between the two sun measurements with the small aperture in the light path once via the sub-solar port in anti-flight direction (*sub-solar-calibration-pointing*) and the other time in flight direction via the limb port (*sun-occultation–and-calibration-pointing*) lie around 0.1 pixels. The difference between the two limb viewing sun observations with large (*sun-over-ESM-diffuser-calibration*) respectively small aperture (*sun-occultation–and-calibration-pointing*) are larger - as expected - and lie around plus/ minus 0.2 pixels. Furthermore the influence if measured near the equator or elsewhere could be checked in another investigation.

We suggest to close the objective 79 with the analysis presented in this report.

General points:

- The main focus has been put on the ultra-violet and visual channels.
- The neutral density filter transmission has changed with respect to the on-ground results, and the ESM-mirror/ -diffuser degradation has been independently changed as reported earlier. For comparisons within this work no correction has been implemented since the effect of this is estimated to be minor within the frame of these investigations.
- Stray light corrections are not accounted for.
- Doppler shift corrections for the *sun-occultation–and-calibration-pointing* and *sun-over-ESM-diffuser-calibration* have been omitted. For channels 1 to 5 the effect is smaller than the accuracy of the intended comparison. The expected maximum Doppler shift in channel 8 for solar spectra is 0.047 nanometres with an annual variation of up to plus/ minus nine percent.
- The detector temperature requirements for in-flight were never met during the investigated switch on data acquisition states.

Annex 1 Used in-flight msm's

Table 10 List of used msm's performed during SODAP. Mainly measurement from measurement window 5.1 (MW5.1)/ lunar measurement 3 (LM3) after the nadir cover release have been used. The special state name, the state IDs are followed by the records and the level 0 file name where the raw data can be found.

Msm	Special State	St. ID	Rec.	File name SCI_NL__…	Orbit
AZACM (limb cover) release					**477**
Sciamachy Radiant Cooler (SRC) cover release					**653**
ELACM (nadir cover) release					**1594**
MW5.1/ LM3	Bet_51 (SO&C)	51	1121-2143 (2136-2143)	0PNPDK20020623_052841_x_00077_**01634**_0150.N1	1634
	Bet_62 (sun-ESM-diffuser)	62	2261-2499	0PNPDK20020623_163009_x_00083_**01640**_0156.N1	1641
	Bet_59 (int SLS)	59	10390-10391	0PNPDK20020623_190232_x_00085_**01642**_0158.N1	1642
	Bet_53 (sub-solar)	53	281-323 (293-296)	0PNPDK20020624_215451_x_00101_**01658**_0189.N1	1658
Mon6b_1	D_SLS_Pre59	9	10-12 16-18	0PNPDK20020626_172920_x_00127_**01684**_0221.N1	1684
	SLS_Pre59	59	13-15		
Nominal operation					
	sscp02, sub_solar_cal_ pointing	53	2288-2331	0PNPDK20030326_210951_x_00029_**05594**_0412.N1	

Annex 2 Literature vacuum lines for SLS

Table 11 Spectral emission line list for slit function calibration using the PtCrNe hallow cathode lamp as internal SLS per channel with vacuum literature wavelengths in nanometres for the used algorithms. These are followed by the expected pixel positions and the minimum and maximum of the used fitting frame. The description gives the name of the emission line. (Marked in red are changes with respect to the inputs from the OPTEC5 results.)

CH	Line #	Wavelength [nm]	Exp pixel pos	Min	Max	Descr.	
1	1	244.0800	229	222	234	PtI	
1	2	248.7920	266	262	272	PtI	
1	3	262.8810	384	381	389	PtI	
1	4	265.1650	403	401	407	PtI	
1	5	266.0240	411	407	415	PtI	
1	6	273.4770	476	471	480	PtI	
1	7	281.0310	543	540	546	NeII	Not used OP5
1	8	283.1130	562	557	564	PtI	
1	9	293.0650	652	646	658	PtI	
1	10	304.3530	754	750	757	PtI	
1	11	306.5600	774	770	779	PtI	
2		321.9122	837	833	839	NeII	Not used in-flight
2		332.4690	742	740	744	NeII	Not used in-flight
2	1	335.5981	714	711	718	NeII	
2	2	337.9187	693	688	698	NeII	
2	3	339.3772	680	676	682	NeII	
2	4	340.9110	666	662	669	PtI	
2		344.86908	629	627	633	NeI	Not used in-flight
2	5	352.14783	562	557	565	NeI	
2		356.9519	517	515	523	NeII	Not used in-flight
2	6	369.5263	399	395	403	NeII	
2		372.8165	368	365	372	NeII	Not used in-flight
2	7	390.9864	198	194	201	CrI	
3	1	427.5999	178	174	182	CrI	
3	2	429.0923	184	181	191	CrI	
3	3	492.3654	450	446	454	CrI	
3	4	540.20632	654	651	657	NeI	

CH	Line #	Wavelength [nm]	Exp pixel pos	Min	Max	Descr.	
3	5	574.98934	802	796	805	NeI	
3	6	576.60178	808	805	813	NeI	
3	7	582.17694	832	828	835	NeI	
3		588.35254	858	851	864	NeI	Not used in-flight
3	8	594.64812	884	877	890	NeI	
3	9	603.16667	919	912	926	NeI	
3	10	607.60194	938	932	943	NeI	
3	11	609.78507	947	942	953	NeI	
3	12	616.52996	974	970	980	NeI	
3	13	621.90013	996	989	1002	NeI	
4	1	603.16667	35	29	41	NeI	
4	2	607.60194	55	49	61	NeI	
4	3	609.78507	65	59	71	NeI	
4	4	616.52996	95	91	101	NeI	
4	5	621.90013	120	113	126	NeI	
4	6	626.82283	142	136	148	NeI	
4	7	630.65325	160	155	166	NeI	
4	8	638.47562	196	190	201	NeI	
4	9	653.4687	266	261	272	NeI	
4	10	660.07755	297	291	303	NeI	
4	11	668.01202	334	328	340	NeI	
4	12	693.13788	454	447	460	NeI	
4	13	717.59155	571	564	578	NeI	
4	14	724.71631	606	598	614	NeI	
4	15	744.09472	699	690	708	NeI	
4	16	749.09335	723	719	728	NeI	
5	1	808.46806	118	110	126	NeI	
5		813.86428	137	133	143	NeI	Not used in-flight
5	2	830.26077	193	187	199	NeI	
5	3	842.07408	234	228	240	NeI	
5		849.76940	262	256	268	NeI	Not used in-flight
5		859.36188	295	290	303	NeI	Not used in-flight
5		863.70188	311	304	313	NeI	Not used in-flight
5	4	892.19495	412	407	417	NeI	
5	5	915.11825	494	488	502	NeI	
5	6	920.42844	513	507	518	NeI	
5	7	942.79647	594	589	600	NeI	
5		944.9620	602	599	604	NeI	Not used

CH	Line #	Wavelength [nm]	Exp pixel pos	Min	Max	Descr.	
							in-flight
5	8	946.18045	606	604	612	NeI	
5	9	948.92843	616	612	623	NeI	
5		953.67782	634	627	636	NeI	Not used in-flight
5	10	966.80706	681	675	688	NeI	
5	11	1056.53015	1001	994	1010	NeI	
6	1	1056.53015	106	100	112	NeI	
6		1080.10008	136	133	139	NeI	Not used in-flight
6		1084.74477	142	139	146	NeI	Not used in-flight
6	2	1169.12011	251	247	255	NeI	
6	3	1198.81924	289	285	295	NeI	
6	4	1206.96360	300	295	305	NeI	
6	5	1246.27976	351	344	353	NeI	
6	6	1269.26721	381	379	385	NeI	
6	7	1291.55459	410	406	415	NeI	
6	8	1322.28558	451	444	456	NeI	
6	9	1523.48758	713	710	719	NeI	
6	10	1716.66169	956	948	963	NeI	
7	1	1958.2480	207	197	217	NeI	
7	2	2035.5793	940	925	955	NeI	
8	1	2269.3965	76	64	88	NeI	
8	2	2310.6817	394	382	412	NeI	
8	3	2326.6649	522	504	544	NeI	
8	4	2337.9377	615	596	635	NeI	Dead pixel 7783 in middle of fit
8	5	2364.2965	839	820	860	NeI	

Annex 2.1 Example slit function results per fitted line

Table 12 FWHM with Gaussian and simple hyperbolic algorithms. Results from *internal SLS* msm in orbit 1642, *internal SLS* msm's during OPTEC5 and key data values retrieved with the *external SLS* (s-polarised). Grey shaded the suggested best fitting slit functions per channel. Results in channel 7 and 8 from the in-flight msm are not listed, since they are not reliable [see text].

Fitted wavelength [nm]	Gauss FWHM [pixel]			Simple hyperbolic FWHM [pixel]		
	Orbit 1642	OPTEC5		Orbit 1642	OPTEC5	
		int SLS	ext s_pol SLS (key data)		int SLS	ext s_pol SLS (key data)
Channel 1						
244.08	1.9998	2.0793	2.0972	2.2177	2.0407	2.0633
248.792	2.0182	1.9896	1.9806	2.0211	2.267	2.2689
262.881	1.8179	1.9696	1.9426	2.0898	2.027	1.9978
265.165	1.7809	1.4759	1.6057	1.8726	1.6079	1.6233
266.024	1.6683	1.8522	1.8867	1.8698	1.9361	1.9596
273.477	1.7466	1.8572	1.8771	1.88	1.908	1.9259
281.031	1.8443	1.7402	--	1.9076	1.839	--
283.113	1.5664	1.8148	1.8513	1.7837	1.9015	1.9186
293.065	1.6249	1.8008	1.8643	1.7986	1.8677	1.9086
304.353	1.7113	1.4993	1.8097	1.8107	1.6609	2.0346
306.56	1.7456	1.6135	1.864	1.8385	1.7866	2.0376
Channel 2						
335.5981	1.7044	1.7539	1.7905	1.8303	1.8336	1.882
337.9187	1.7863	1.7828	1.8258	1.853	1.857	1.9546
339.3772	1.6755	1.6193	1.891	1.8169	1.8212	2.0024
340.9110	1.7322	1.7009	1.8148	1.865	1.9249	1.9578
352.1478	1.7088	1.6051	1.6457	1.8121	1.7629	1.8455
369.5263	1.7348	1.762	1.8612	1.8344	1.8348	1.9611
390.9864	1.7468	1.7761	2.3247	1.8823	2.0305	2.2702
Channel 3						
427.5999	2.0792	2.0827	2.2141	2.111	2.0989	2.219
429.0923	2.0668	2.0521	2.1895	2.083	2.0812	2.3239
492.3654	1.8206	1.7532	1.7675	1.9413	1.907	1.9776
540.2063	1.6022	1.5981	1.507	1.801	1.7966	1.9601
574.9893	1.8817	1.9172	2.1208	1.998	1.9972	2.1037
576.6018	1.7448	1.7638	2.0574	1.9841	1.9984	2.1143
582.1769	1.8551	1.868	2.0148	1.9342	1.9365	2.064
594.6481	1.9081	1.8976	2.0822	1.9536	1.9488	2.2447
603.1667	1.742	1.7349	2.0663	1.9132	1.9324	2.1059
607.6019	1.8164	1.8434	2.0468	1.9362	1.9367	2.0558
609.7851	1.8085	1.8343	1.9962	1.9351	1.9379	2.0316
616.5300	1.6224	1.6377	1.8787	1.7928	1.8361	2.0206
621.9001	1.6115	1.6271	1.8399	1.7771	1.8031	1.9769

Fitted wavelength [nm]	Gauss FWHM [pixel]			Simple hyperbolic FWHM [pixel]		
	Orbit 1642	OPTEC5		Orbit 1642	OPTEC5	
		int SLS	ext s_pol SLS (key data)		int SLS	ext s_pol SLS (key data)
Channel 4						
603.1667	1.7554	1.7609	1.8971	1.8415	1.8436	1.9365
607.6019	1.7707	1.783	1.974	1.8754	1.8825	1.9985
609.7851	1.722	1.7335	1.9903	1.9009	1.9049	2.0429
616.5300	1.8242	1.8229	2.0157	1.8952	1.8975	2.1895
621.9001	1.8006	1.8073	2.0859	2.0108	2.0041	2.1102
626.8228	1.8719	1.8767	2.0768	1.9237	1.9309	2.2335
630.6532	1.834	1.8445	2.0944	1.9774	1.972	2.0925
638.4756	1.8816	1.8917	2.0995	1.975	1.9711	2.0946
653.4687	1.8253	1.8434	2.0376	2.0333	2.0277	2.0798
660.0775	1.8206	1.8403	2.0164	1.9958	1.9904	2.0528
668.0120	1.877	1.8681	1.94	1.9306	1.9285	2.0503
693.1379	1.8449	1.8602	2.1426	1.9306	1.9304	2.1709
717.5915	1.6603	1.6629	1.7829	1.837	1.8477	1.971
724.7163	1.8475	1.8635	1.9526	1.9277	1.9281	1.9886
744.0947	1.7747	1.767	1.8663	1.9131	1.9248	2.1074
749.0933	1.7509	1.7558	1.9137	1.9559	1.9818	2.0747
Channel 5						
808.4681	2.0357	2.0531	2.2408	2.0491	2.1747	2.4391
830.2608	2.0175	2.0236	2.1703	2.0314	2.1058	2.4246
842.0741	1.9823	1.9774	2.1003	2.0078	2.0918	2.3364
892.1949	1.7764	1.9019	1.9678	1.9798	1.9706	1.9996
915.1182	1.9158	1.8609	1.8331	1.9596	1.9457	1.9706
920.4284	1.8835	1.7764	1.78	1.9424	1.9306	2.0049
942.7965	1.8937	1.8658	1.8323	1.9494	1.9366	1.9558
946.1804	1.8804	1.73	1.7178	1.96	1.9365	1.9647
948.9284	1.8915	1.7784	1.7661	1.9469	1.9259	1.9813
966.8071	1.8511	1.9376	2.0111	1.9854	1.973	2.0344
1056.5302	1.9949	2.0236	2.1228	2.0238	2.0251	2.1536
Channel 6						
1056.5302	1.8033	1.8125	1.7263	1.9931	1.9929	1.9403
1169.1201	1.7541	1.7473	1.7113	1.9285	1.9291	1.8468
1198.8192	1.7671	1.7775	1.6824	1.8653	1.8709	1.8141
1206.9636	1.7743	1.7769	1.763	1.8755	1.8832	1.854
1246.2798	1.802	1.8135	1.7542	1.8706	1.8785	1.8393
1269.2672	1.7561	1.7607	1.693	1.8529	1.8535	1.8114
1291.5546	1.6137	1.6271	1.5357	1.7561	1.7665	1.6798
1322.2856	1.5497	1.5437	1.4895	1.6912	1.6823	1.606
1523.4876	1.7017	1.6994	1.6719	1.7927	1.7914	1.767
1716.6617	1.6503	1.7511	1.6575	1.8567	1.9931	1.7834

Fitted wavelength [nm]	Gauss FWHM [pixel]			Simple hyperbolic FWHM [pixel]		
	Orbit 1642	OPTEC5		Orbit 1642	OPTEC5	
		int SLS	ext s_pol SLS (key data)		int SLS	ext s_pol SLS (key data)
Channel 7						
1958.248		1.7383	1.9903		2.0018	2.1503
2035.5793		1.6744	1.7748		1.8492	1.8787
Channel 8						
2269.3965		1.634	-		1.8074	-
2310.6817		1.7385	1.6948		1.8262	1.8021
2326.6649		1.7602	1.7297		1.9821	1.9325
2337.9377		2.4486	2.4997		2.5593	2.8088
2364.2965		2.0623	1.9946		2.0605	2.0482

Annex 3 Fraunhofer lines

Table 13 Fraunhofer lines used for the slit function calibration of the sun spectra from key data and the in vacuum conditions transformed wavelengths with the help of the NIST atomic database.

CH	#	Wavelength key data [nm]	Wavelength vacuum [nm]	Exp px pos key data	Exp px pos	Min	Max	Descr.	source	remark
1	1	246.265	246.3392	246	246	243	249	FeI	NIST	
1	2	258.590	258.5312	347	348	344	351	FeI	NIST	
1	3	272.090	271.9833	464	463	460	465	FeI	NIST	
1	4	285.213	285.29642	581	581	575	589	MgI	NIST	
1	5	294.921	294.8738	669	668	666	672	FeII	NIST	
1	6	305.9094	305.9975	768	768	766	772	FeI	NIST	
2		317.9342	318.0251	873	870	865	874	CaII	NIST	Not used
2	1	336.1193	336.2184	709	709	704	714	TiII	NIST	
2	2	349.7843	349.8841	584	584	581	586	FeI`	NIST	
2		364.7851	364.8882	444	442	439	444	FeI	NIST	Not used
2	3	375.8245	375.9301	340	339	337	341	FeI	NIST	
2	4	385.9992	386.1006	244	243	240	246	FeI	NIST	
2	5	-	393.4777	-	174	168	183	CaII	NIST	k
2	6	-	396.9591	-	141	135	147	CaII	NIST	h
3	1	-	396.9591	-	53	50	57	CaII	NIST	h
3	2	404.5825	404.6956	84	85	82	87	FeI	NIST	
3	3	-	410.292	-	107	103	111	H	NIST	Delta double
3	4	-	420.3212	-	147	144	151	FeI	NIST	
3	5	422.6740	422.7918	158	158	156	161	CaI	NIST	
3	6	-	432.6978	-	199	196	202	FeI	NIST	
3	7	-	434.17	-	205	202	208	H	NIST	Gamma double
3	8	-	438.4776	-	223	221	225	FeI	NIST	
3		470.3003	470.43068	357	357	354	361	MgI	NIST	Large width, not used
3	9	-	486.272	-	424	419	427	H	NIST	Beta double
3	10	-	492.1875	-	449	447	452	FeI	NIST	
3	11	495.761	495.8981	465	465	462	467	FeI	NIST	c
3	12	518.3619	518.50479	561	562	560	564	MgI	NIST	b1
3	13	552.8418	552.99403	708	709	706	711	MgI	NIST	
3		588.9973	-	932				NaI	SFF	Not used
4	1	616.2180	616.3878	94	95	93	97	CaI	NIST	Many lines
4		630.1508	-	157				FeI	SFF	Not used
4	2	646.2570	646.4353	232	233	231	235	CaI	NIST	
4	3	656.2808		279	280	274	286	Hα	SFF	C?

CH	#	Wavelength key data [nm]	Wavelength vacuum [nm]	Exp px pos key data	Exp px pos	Min	Max	Descr.	source	remark
4	4	746.2342	746.2342	710	711	708	714	CrI	NIST	
4		778.0568	778.237	862	862	859	865	FeI	NIST	Not used
5	1	838.7782	839.0075	223	223	221	226	FeI	NIST	
5	2	849.8062	850.035	261	263	259	267	CaII	NIST	
5	3	854.2144	854.444	277	278	274	282	CaII	NIST	
5	4	866.2170	866.452	319	320	317	324	CaII	NIST	
5	5	-	869.1007	-	329	327	332	FeI	NIST	
5	6	-	879.579	-	366	364	369	FeI	NIST	
5	7	880.6775	880.9175	371	372	369	375	MgI	NIST	
5	8	-	882.665	-	378	375	381	FeI	NIST	
5	9	-	886.939	-	393	388	396	FeI	NIST	
5		-	892.981	-	416	413	418	FeI	NIST	Not used
5		988.905	-	761				FeI	SFF	Not used
6		1058.5137	1058.8040	109	109	106	112	SiI	NIST	?
6		1066.0990	1066.3891	118	118	115	121	SiI	NIST	?
6	1	1282.1614	-	398	398	395	401	H	L&W	
6		1487.6060	-	667	667	664	668	NiI	L&W	Dead pixel
6		1672.3527	-	901	901	899	903	AlI	L&W	
7		1949.8689	-	133	133	130	136	SiI	L&W	
7		1978.2198	-	386	386	384	389	CaI	L&W	Dead pixels
7		1985.8527	-	456	457	455	460	CaI	L&W	
7	1	1986.7642	-	465	465	462	467	CaI	L&W	
7	2	1992.2620	-	516	516	513	519	CaI	L&W	
7		2009.7538	-	683	683	680	686	?	?	
7	3	2034.9441	-	933	933	930	936	SiI	L&W	
8	1	2261.4167	-	16	16	13	19	?	?	
8		2267.1984	-	59	59	56	62	SiI	L&W	Dead pixels
8		2274.6659	-	115	115	112	118	FeI	L&W	Dead pixels
8	2	2281.4226	-	166	166	163	169	MgI	L&W	
8		2291.2700	-	242	242	239	245	?	?	No absorption line visible
8		2335.4773	-	594	595	591	597	NaI	L&W	Dead pixels
8		2338.5522	-	619	620	616	622	NaI	L&W	
8		2383.0200	-	1000	1000	997	1003	?	?	Double line

L&W - Livingston and Wallace, 1991

Annex 3.1 Fraunhofer line fit examples

The OPTEC2 wavelength scale (vacuum wavelengths) is used for the on-ground observations. The wavelength calibration (also vacuum wavelengths) using the *internal SLS* measurement in orbit 1642 is used for the in-flight measurements. The Fraunhofer list [see Table 13] states two wavelengths per fitted line, the ones from the key data (their values are used in the following graph for the names) and the ones transferred to vacuum wavelengths (the vacuum wavelengths are used for the line position of the shown data on the vacuum wavelength). For all graphs shown in the following the colour code of the corrected spectra of in-flight sun observation measurements corresponding to the left y-axis scale is **black** for state_ID 51, the *SO&C pointing*, **red** for state_ID 53, the *sub-solar-calibration-pointing* and **blue** for state_ID 62, the *sun-over-ESM-diffuser* measurement. The on-ground zenith sky measurements shown in **green** is linked to the right y-axis scale with far lower signal values in BU/s.

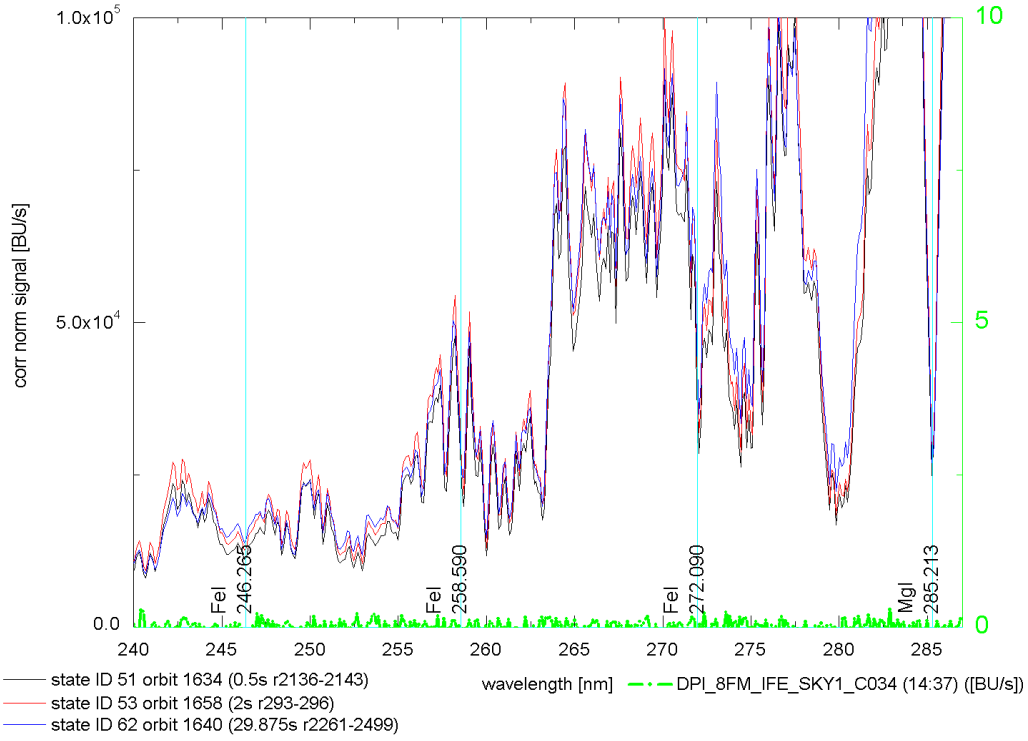

Figure A 1 In-flight sun observation spectra and on-ground zenith sky measurement: **Channel 1** line positions in the beginning of the channel from key data list in Table 13. Corrected spectra of in-flight sun observation measurements (left y-axis scale, **black**: state_ID 51, **red**: state_ID 53, **blue**: state_ID 62) and on-ground zenith sky measurements shown in **green** (right y-axis scale) with low signal values in BU/s due to the absorption in the UV through the earth atmosphere. The **Mg I** line fit can be viewed in Figure 25.

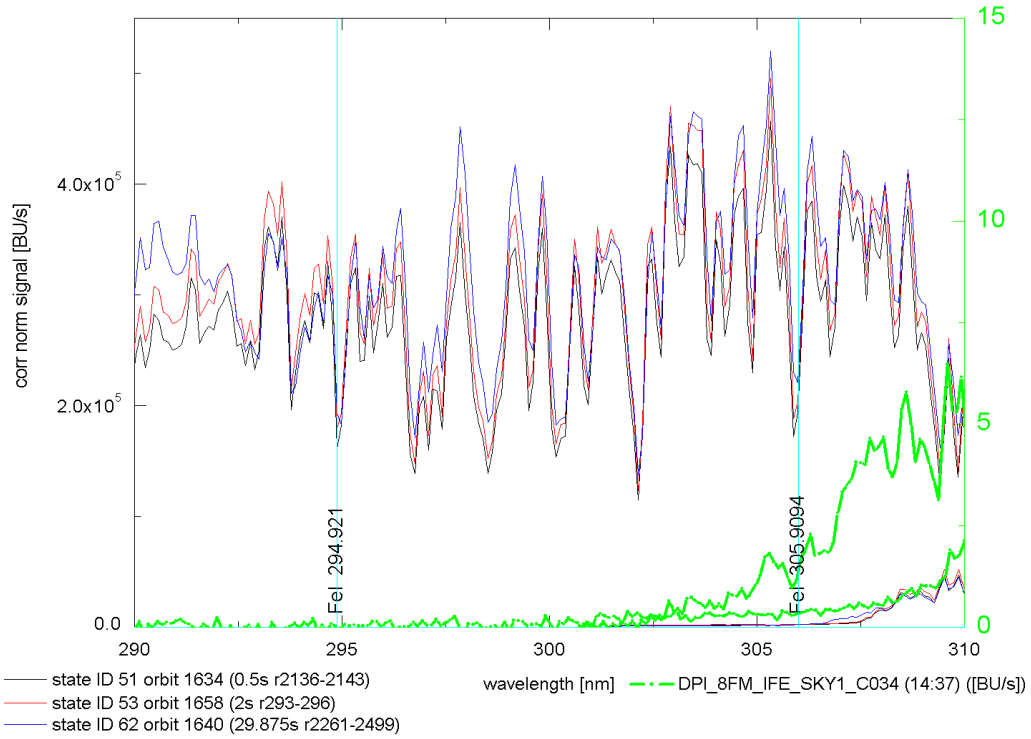

Figure A 2 **Channel 1** line positions. Strong UV absorption through in earth's atmosphere still visible in on-ground zenith sky data visualised in **green**.

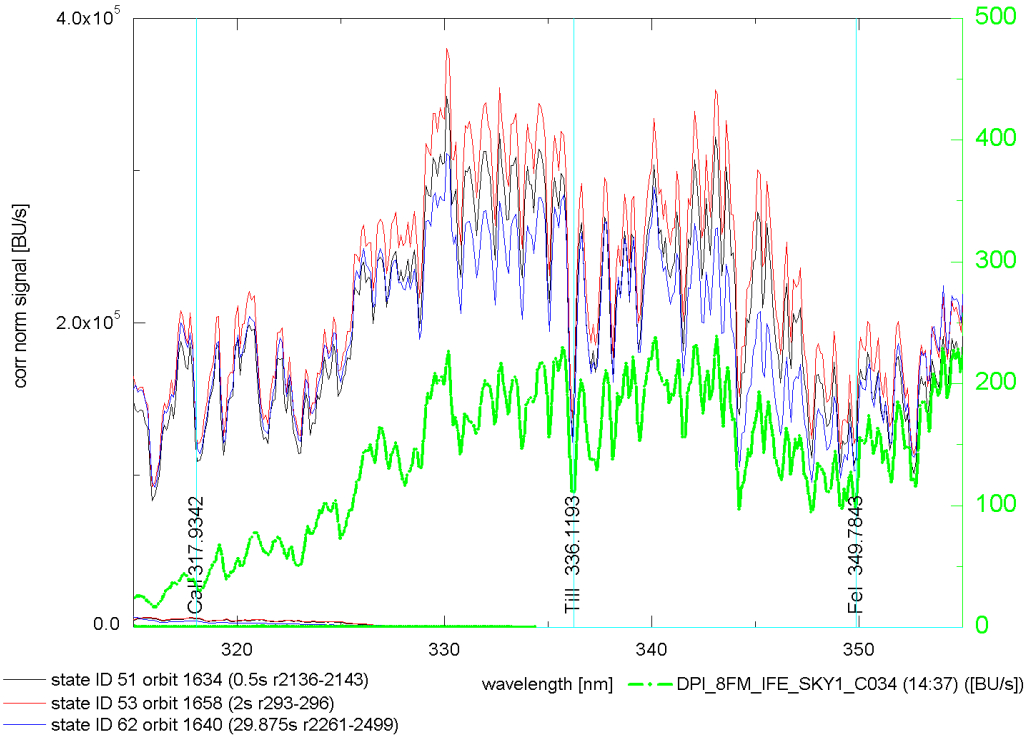

Figure A 3 **Channel 2** line positions in the beginning of the channel. The **Ca II** line is not used for the analysis.

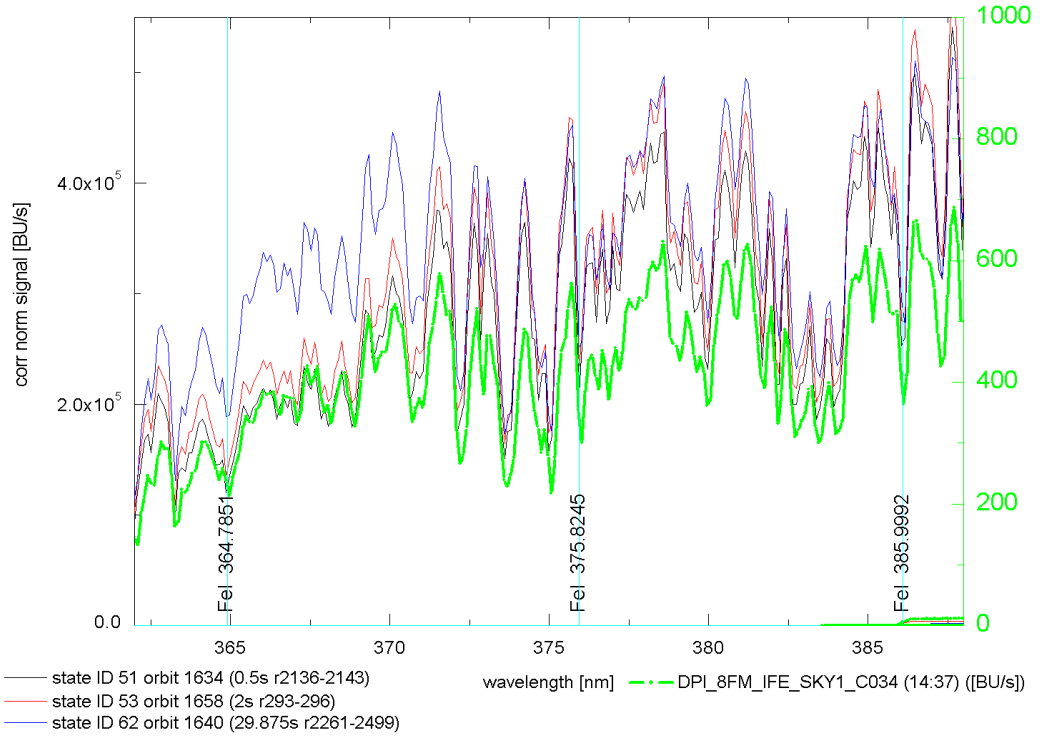

Figure A 4 **Channel 2** line positions. The first shown **Fe I** line is not used in the analysis due to its shape.

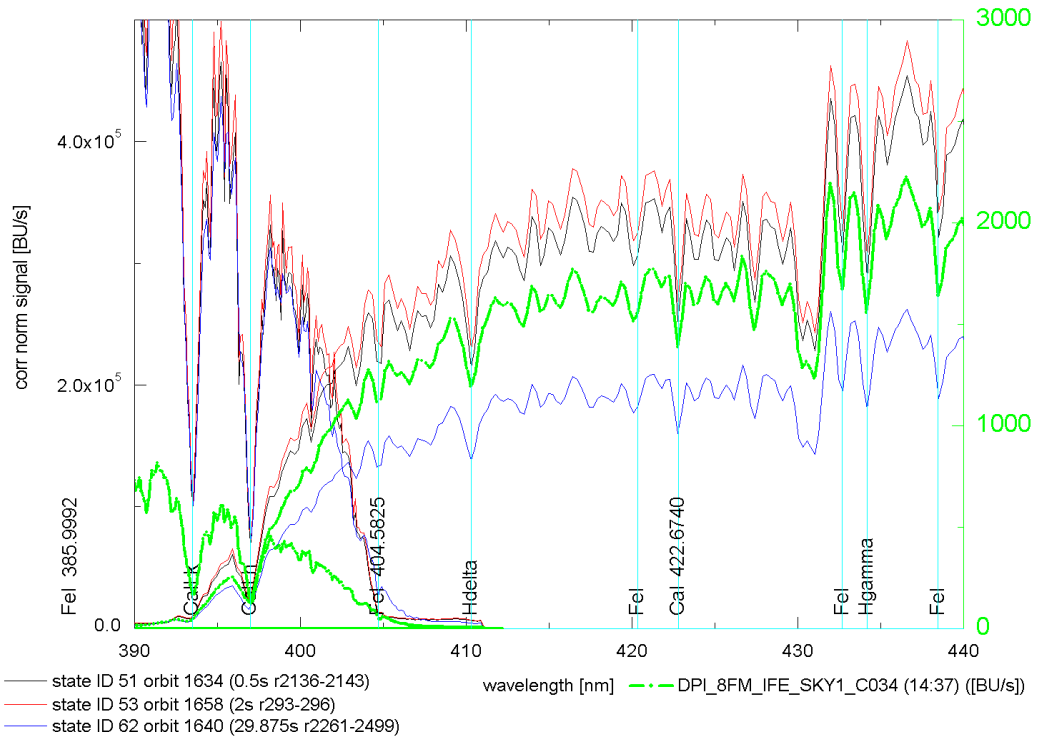

Figure A 5 **Channel 3** line positions in the beginning of the channel (overlap with **channel 2** visible, see also Figure 33). The lines **Fe I** (404.5825 nm) and **Ca I** (422.6740 nm, see also fit in Figure 27) are originated from the key data.

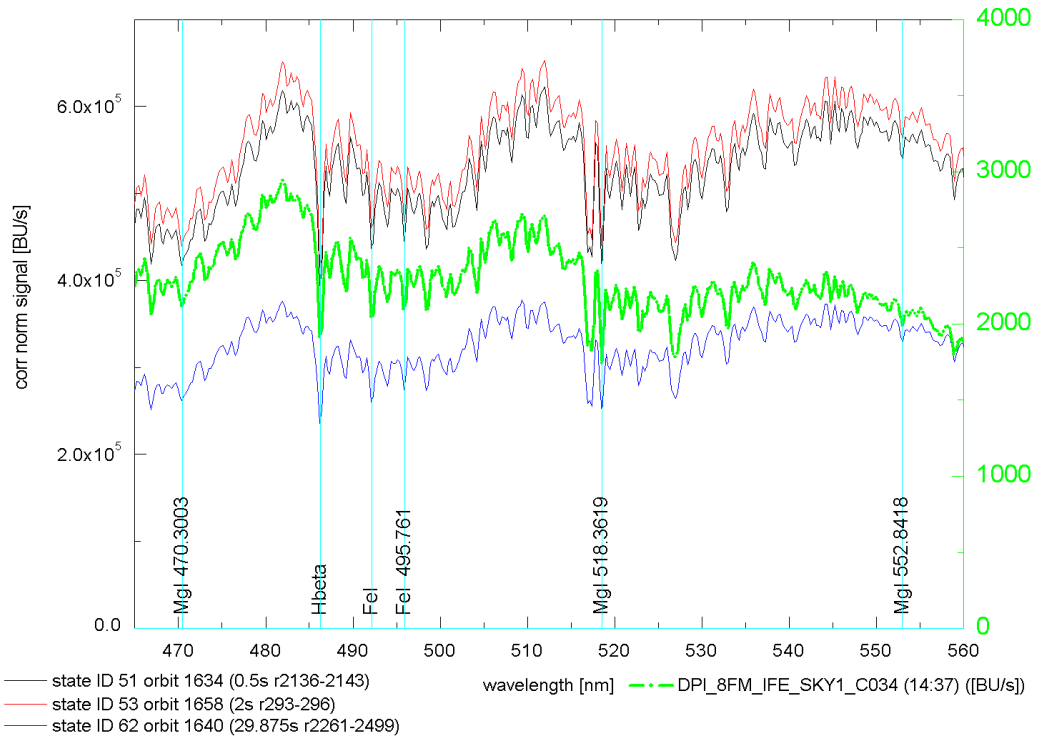

Figure A 6 **Channel 3** line positions. The **Mg I** line (470.3003 nm) is not used in the analysis due to its shape. At the last line position in channel 3: **Na I 588.9973 nm** a double line is visible [see Figure 15]. This line is as well not used.

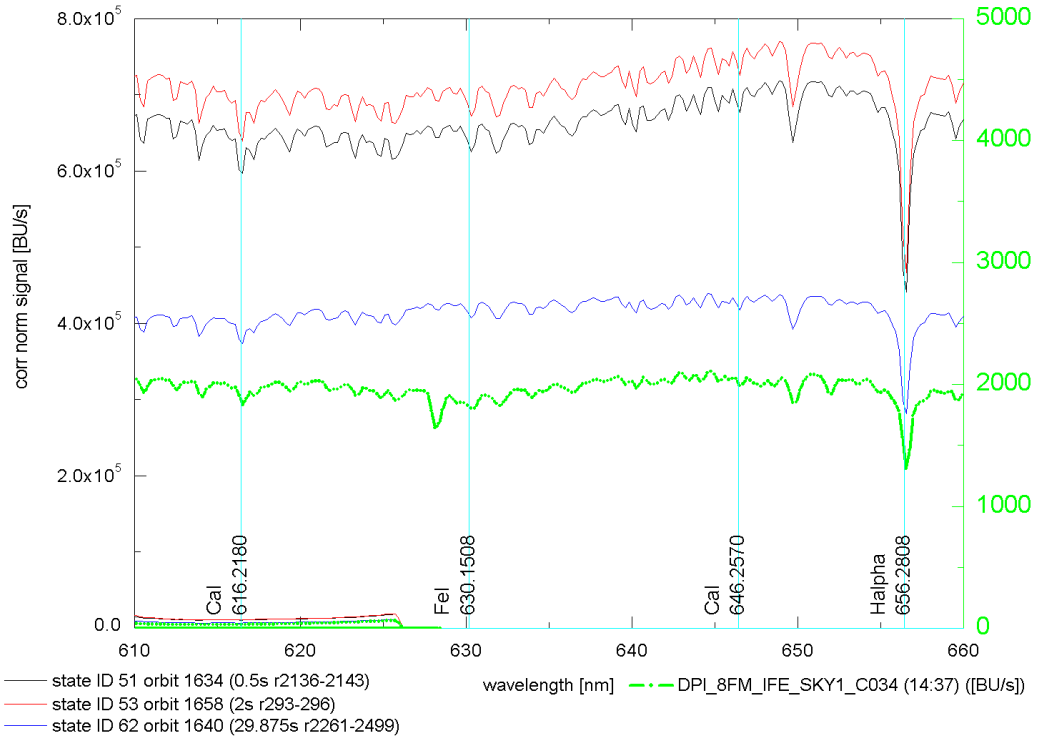

Figure A 7 **Channel 4** line positions in the beginning of the channel. The **Fe I** line **630.1508 nm** is due to its shape not used for the analysis.

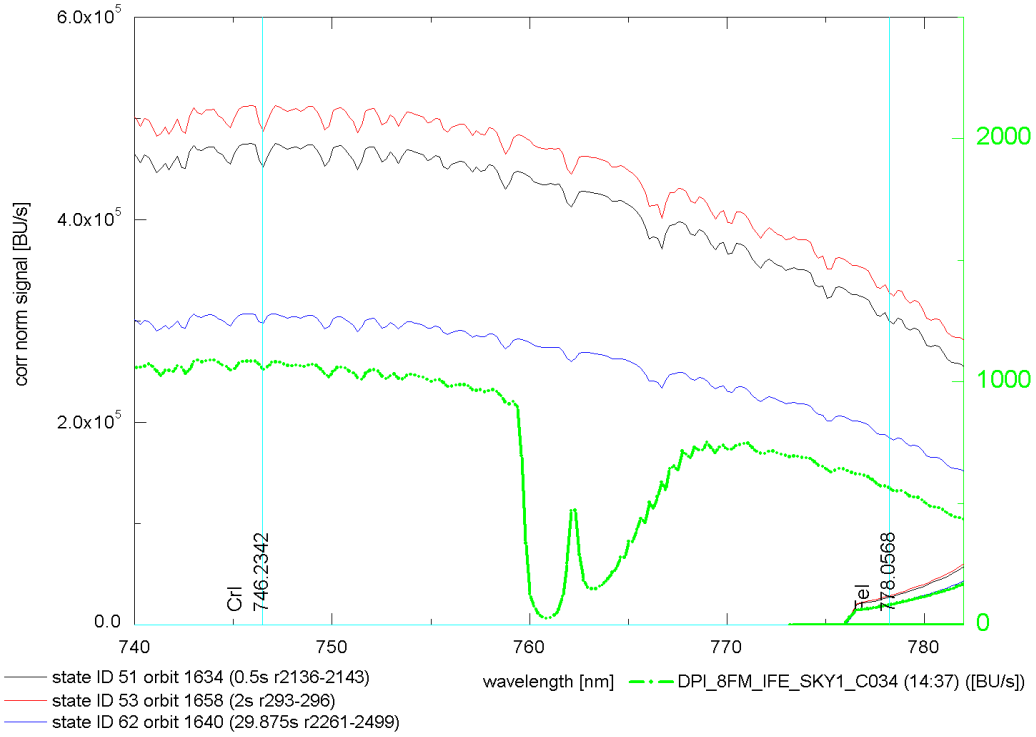

Figure A 8 **Channel 4** line positions at the end of the channel. The **Fe I** line **778.0568 nm** is not used for the analysis. The oxygen A-band feature (around 760 nm) is clearly visible in the on-ground zenith sky measurement.

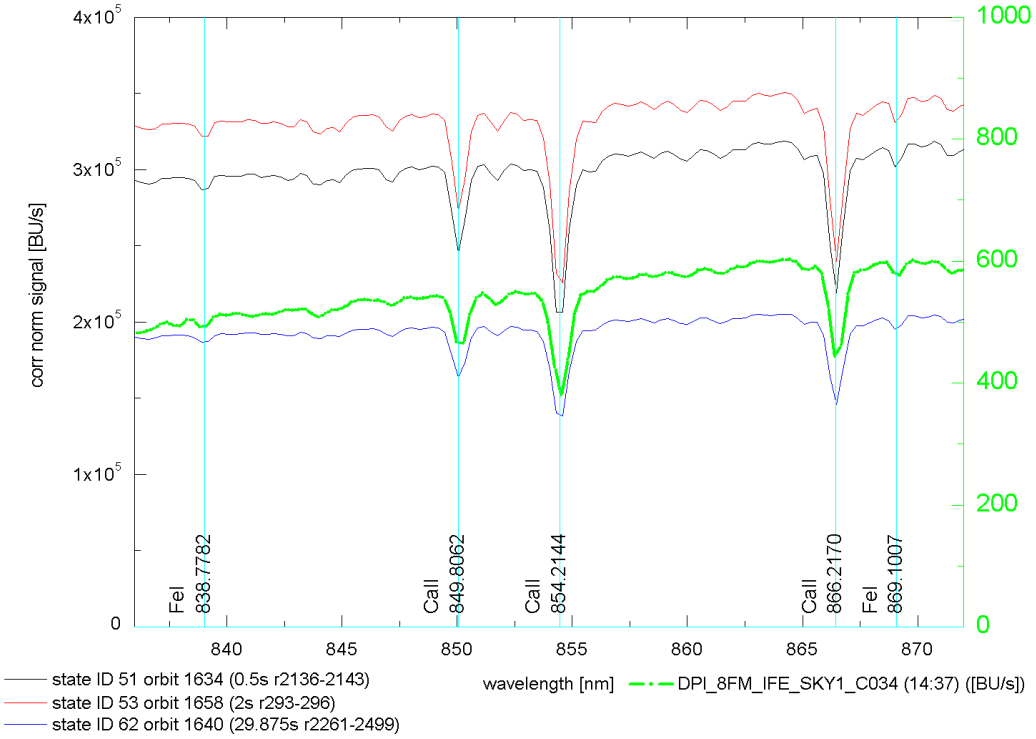

Figure A 9 **Channel 5** first five line positions where the first four are part of the key data.

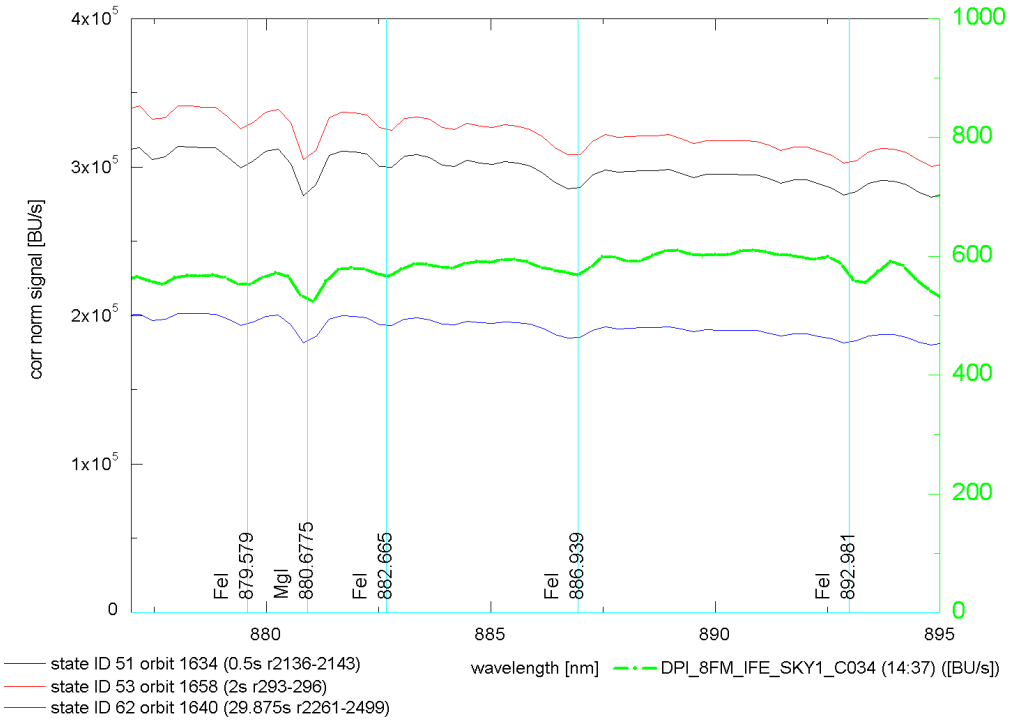

Figure A 10 **Channel 5** following line positions. The fits for the first three line positions shown here are visualised in Figure 29. The **Mg I** line at **880.6775 nm** is the only one from the key data. The last shown line **Fe I** at **892.981 nm** is not used for the analysis (also not included in the key data).

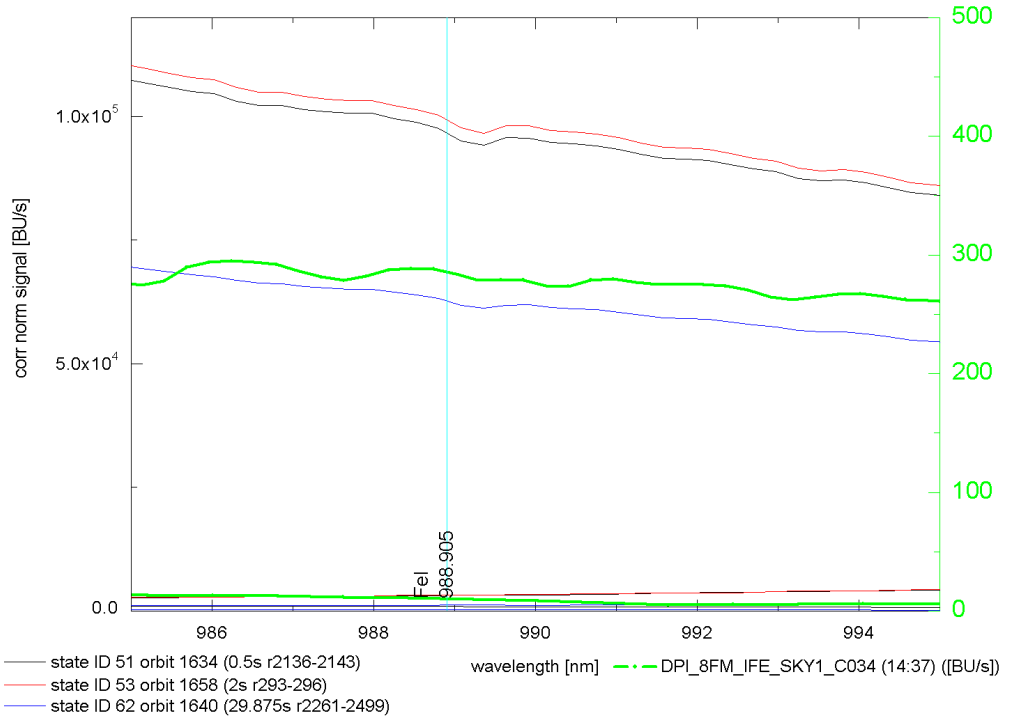

Figure A 11 **Channel 5** last line position given in the key data is not used for the analysis since an absorption feature of **Fe I** at **988.905 nm** is not visible (it could also not clearly be identified from the NIST atomic database list).

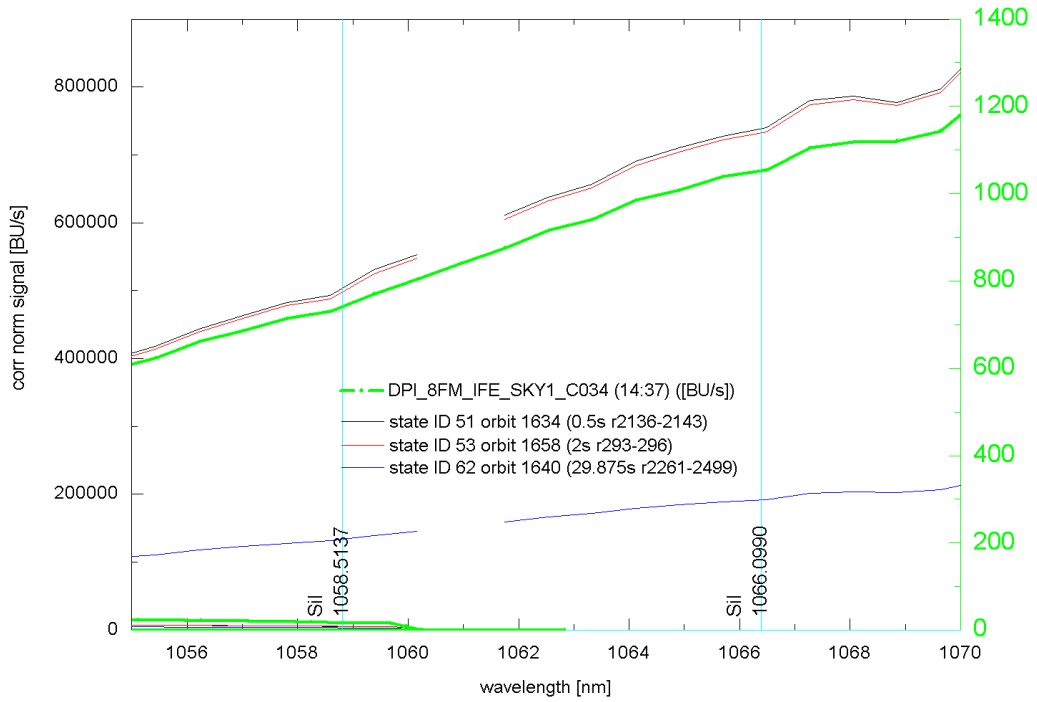

Figure A 12 **Channel 6** first two line positions from list in Table 13. These lines are not used for the analysis. Gaps in the data originate from the data correction.

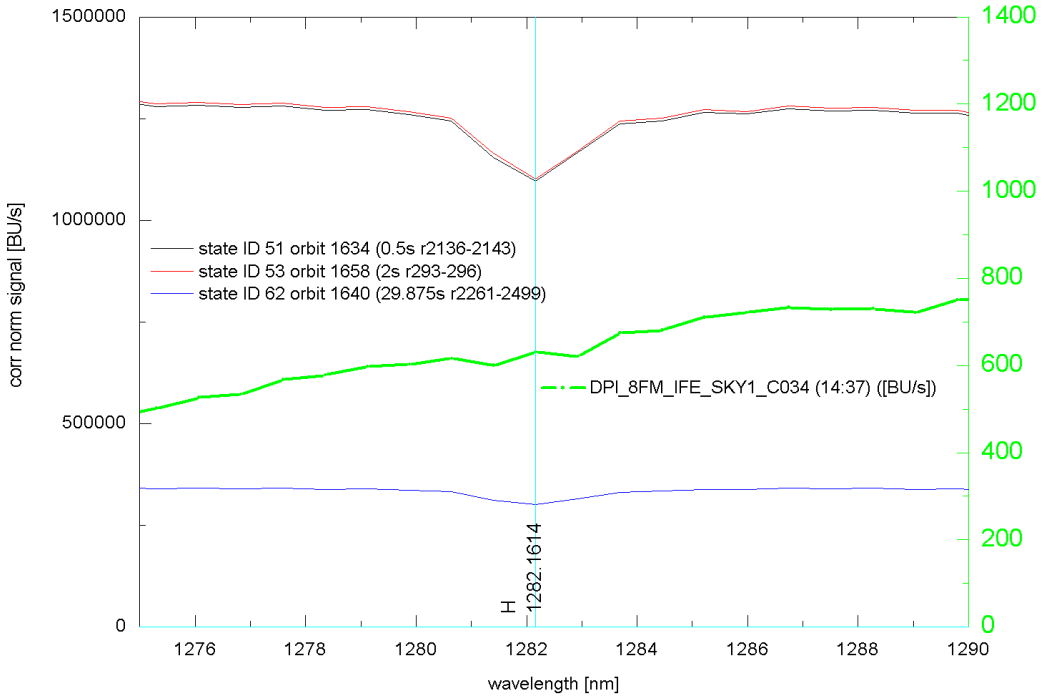

Figure A 13 **Channel 6 H** line (Livingston and Wallace) from list in Table 13.

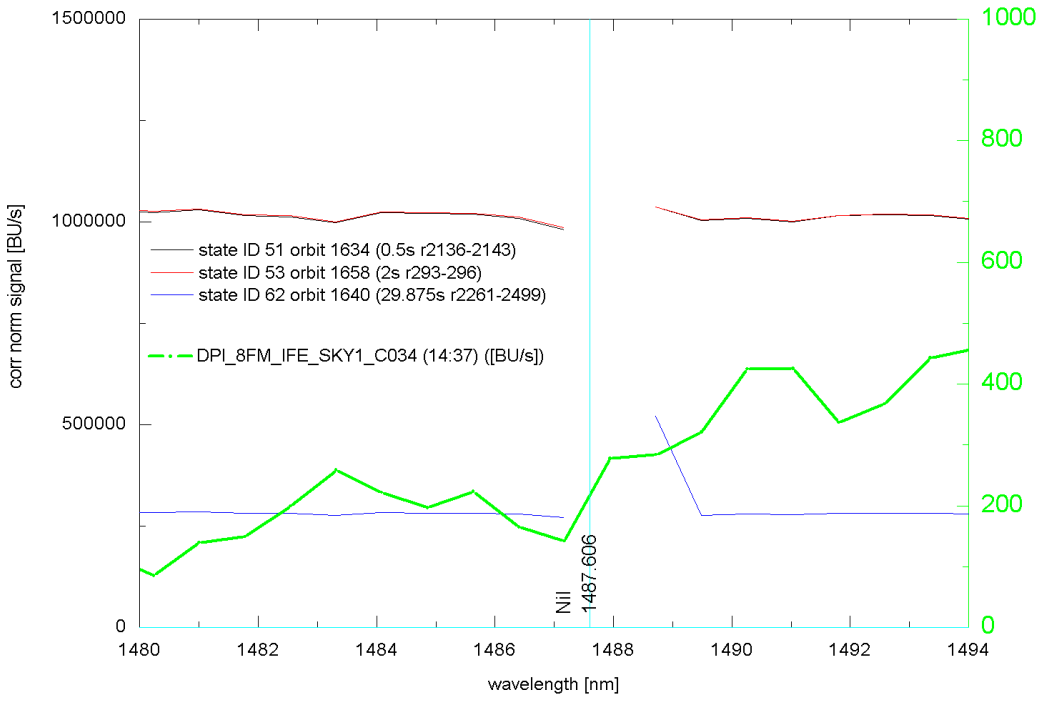

Figure A 14 **Channel 6** line **Ni I** (Livingston and Wallace) from list in Table 13. In the in-flight data of the shown orbits dead/ bad pixels are in this wavelength area.

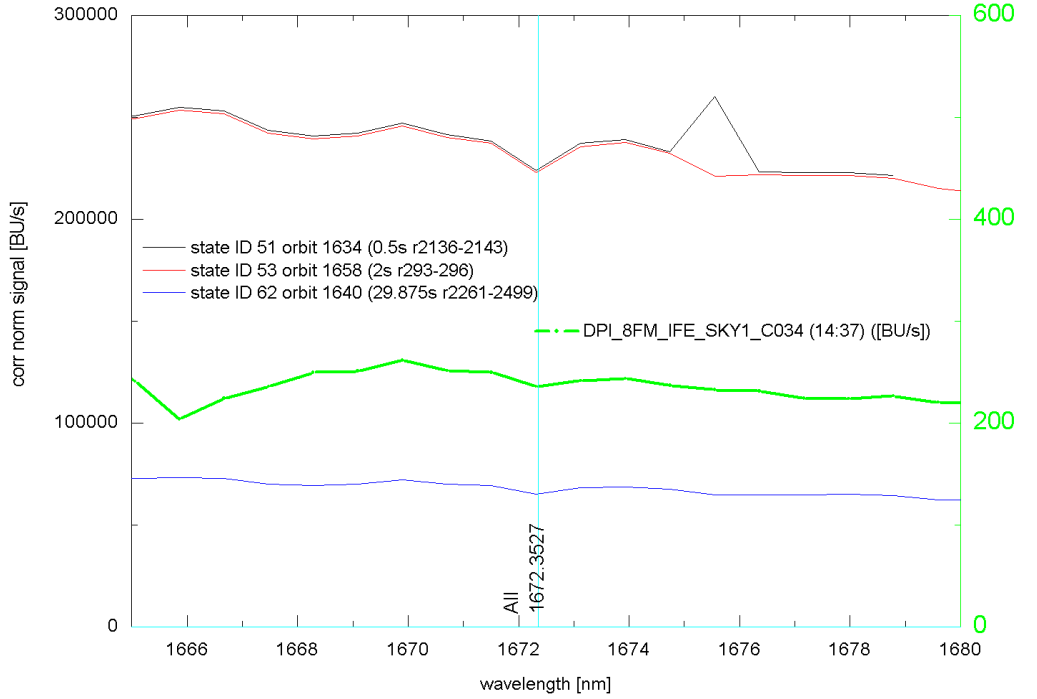

Figure A 15 **Channel 6 Al I** line (Livingston and Wallace) from list in Table 13.

For the completeness the data for channels 7 and 8 will also be shown in the following. Slight wavelength shifts are expected, since the *SO&C-pointing* (state_ID 51) shown in **black** as well as the *sun-over-ESM-diffuser-calibration* (state_ID 62) data in **blue** are not corrected for the Doppler shift, which can not be ignored for these longer wavelengths. Identification of several lines suffers from dead/ bad pixels. The gaps in the in-flight data originate not valid data in that wavelength range. Several line positions from the key data do not overlap with absorption features in the data.

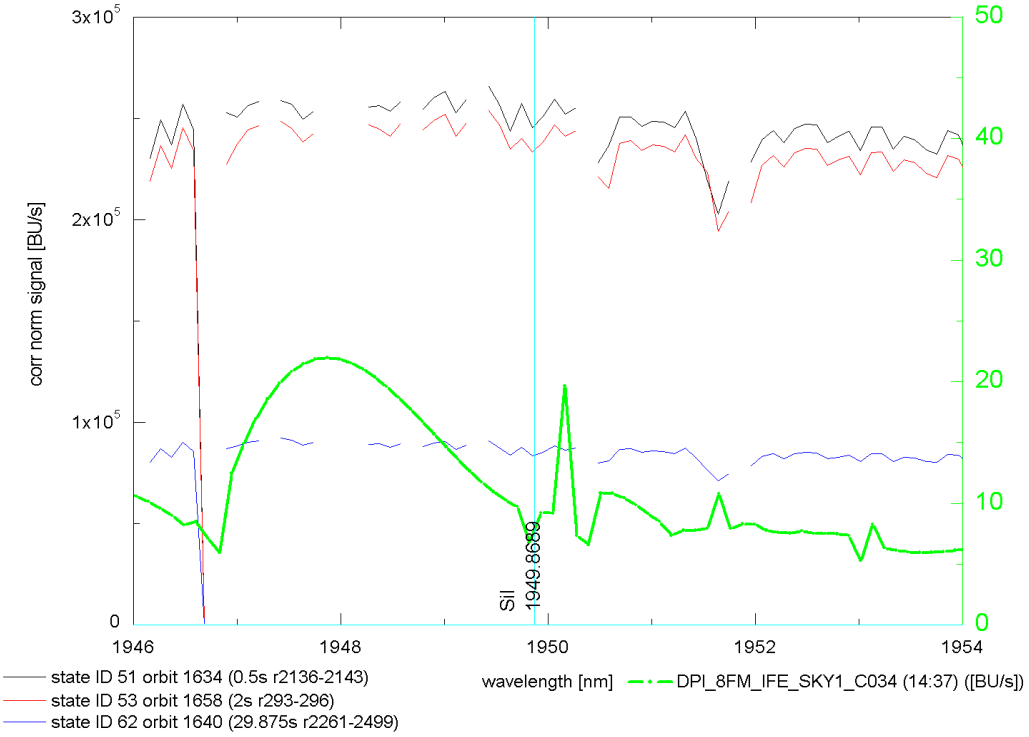

Figure A 16 **Channel 7** line position given in the key data. Not used for the analysis.

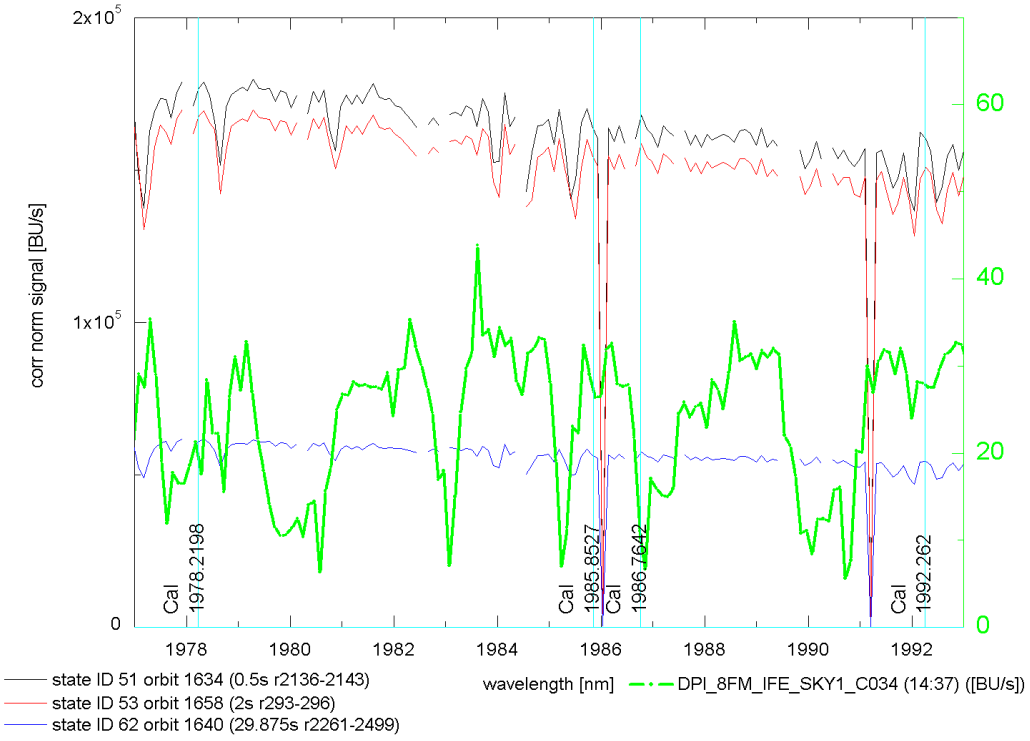

Figure A 17 **Channel 7** line positions given in the key data. Not used for the analysis.

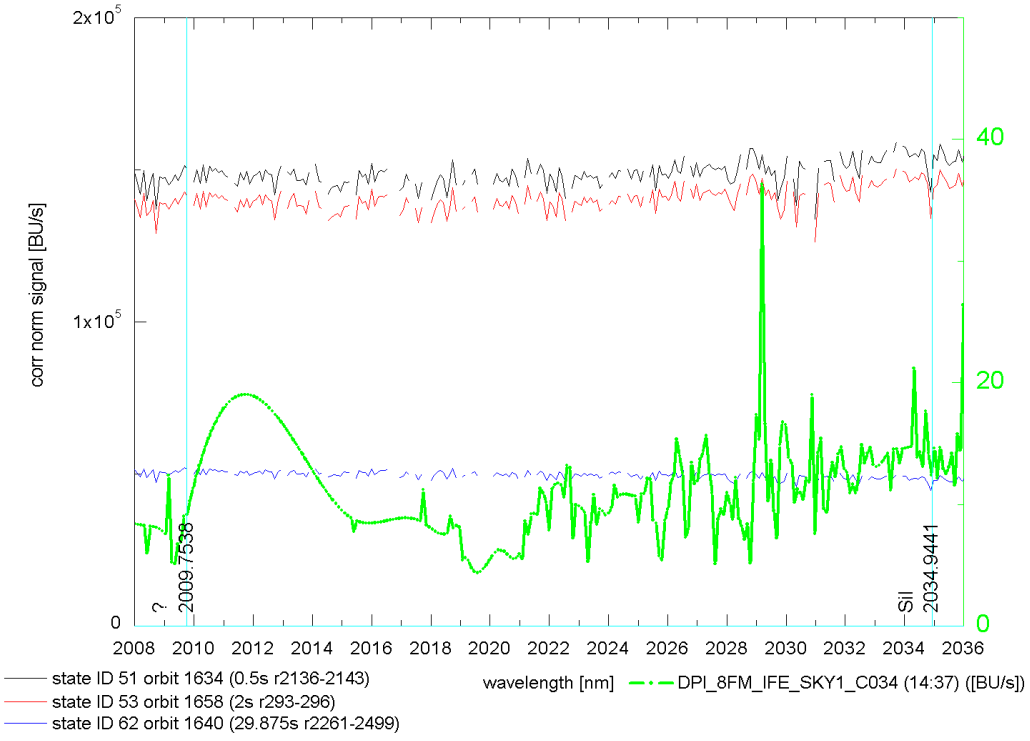

Figure A 18 **Channel 7** line position given in the key data. Not used for the analysis.

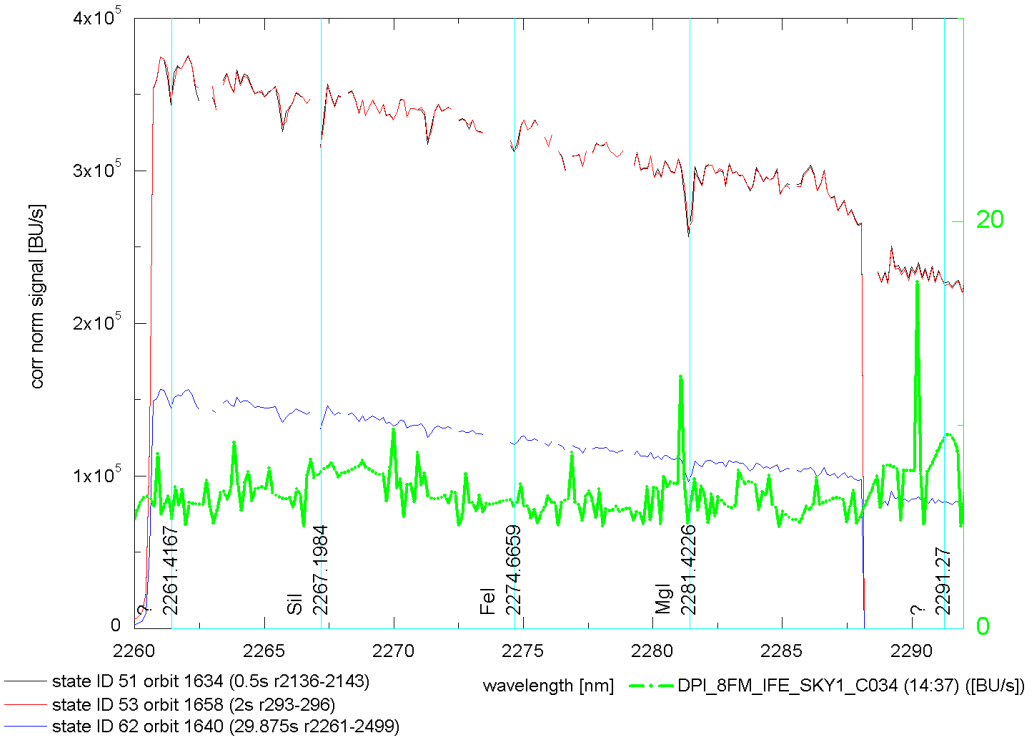

Figure A 19 **Channel 8** line position given in the key data. Not used for the analysis.

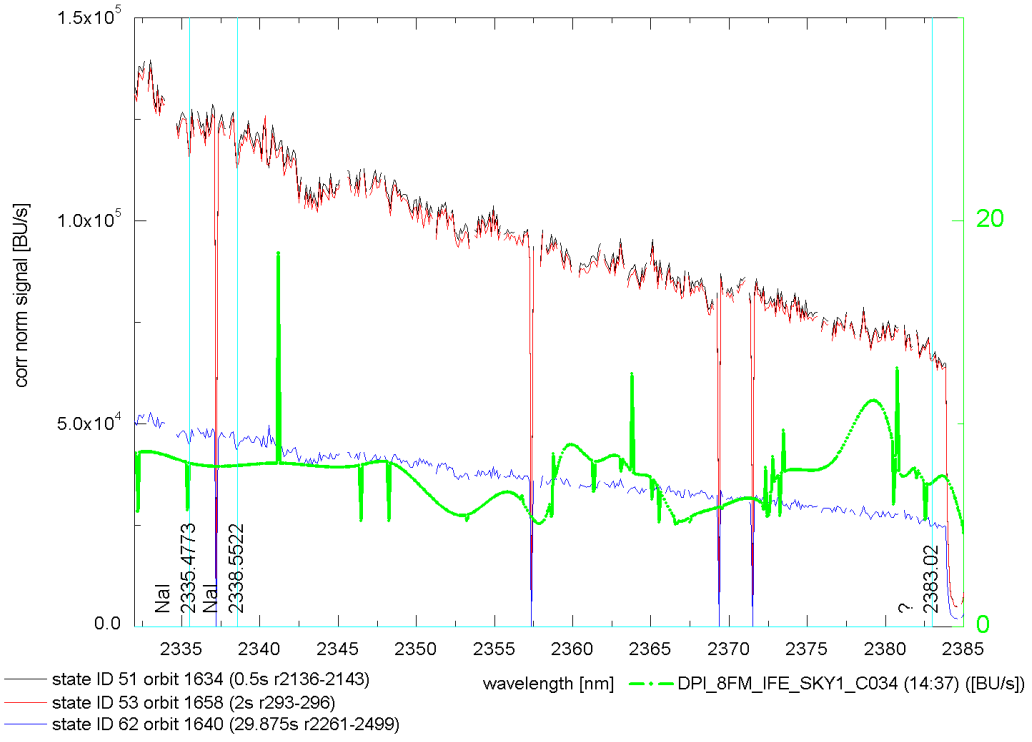

Figure A 20 **Channel 8** line position given in the key data. Not used for the analysis.

Annex 4 Gaussian, simple hyperbolic fit orbit 1642 SLS data

See following pages.

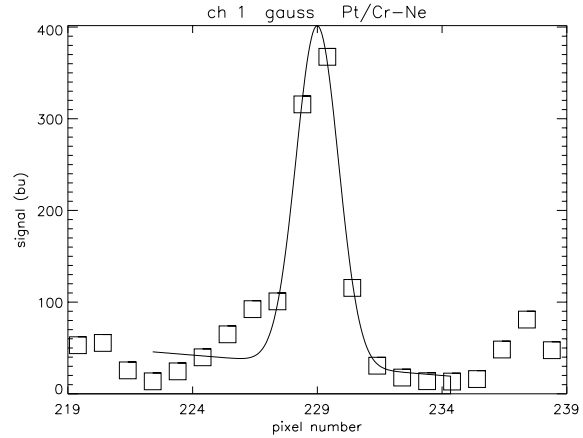
ch 1 gauss Pt/Cr-Ne
signal (bu)
pixel number
0
100
200
300
400
219
224
229
234
239

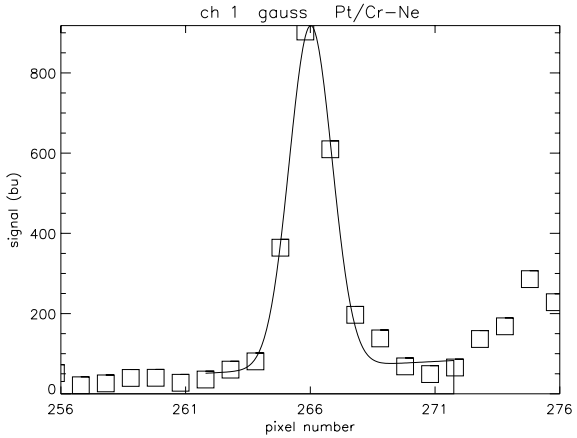
ch 1 gauss Pt/Cr-Ne
signal (bu)
pixel number
0
200
400
600
800
256
261
266
271
276

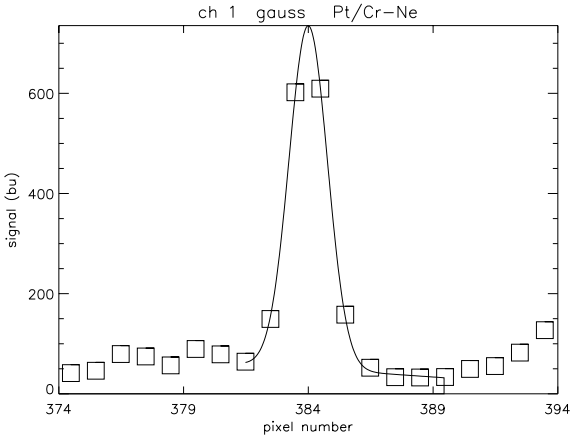
ch 1 gauss Pt/Cr-Ne
signal (bu)
pixel number
0
200
400
600
374
379
384
389
394

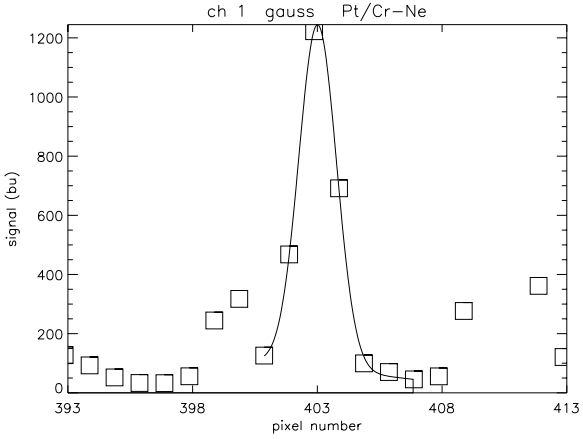
ch 1 gauss Pt/Cr-Ne
signal (bu)
pixel number
0
200
400
600
800
1000
1200
393
398
403
408
413

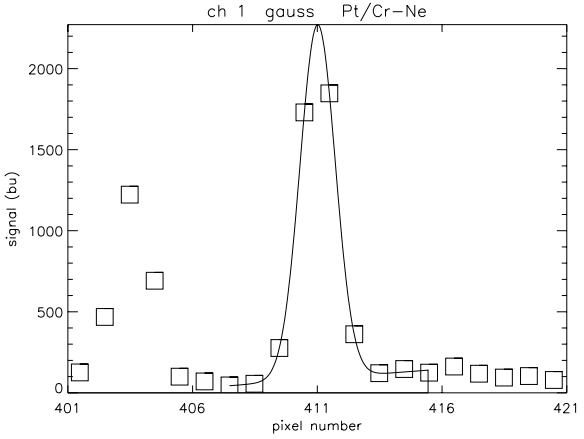
ch 1 gauss Pt/Cr-Ne
signal (bu)
pixel number
0
500
1000
1500
2000
401
406
411
416
421

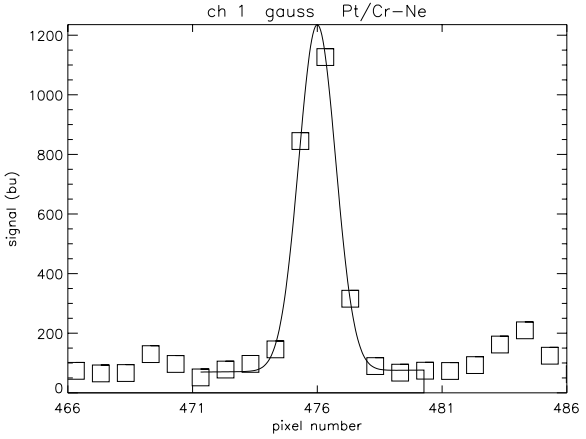
ch 1 gauss Pt/Cr-Ne
signal (bu)
pixel number
0
200
400
600
800
1000
1200
466
471
476
481
486

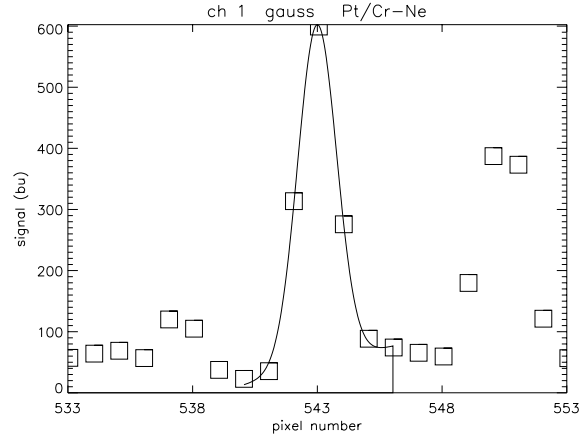
ch 1 gauss Pt/Cr-Ne
signal (bu)
pixel number
0
100
200
300
400
500
600
533
538
543
548
553

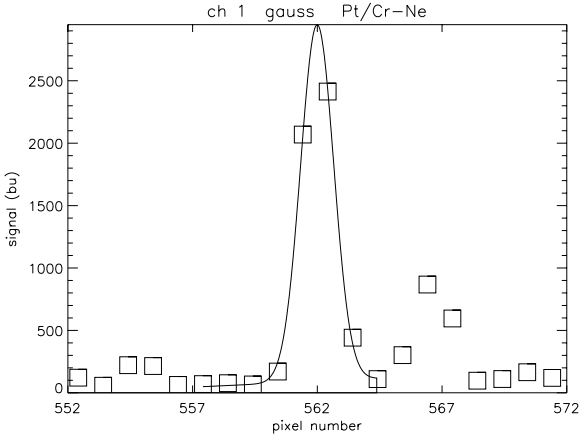
ch 1 gauss Pt/Cr-Ne
signal (bu)
pixel number
0
500
1000
1500
2000
2500
552
557
562
567
572

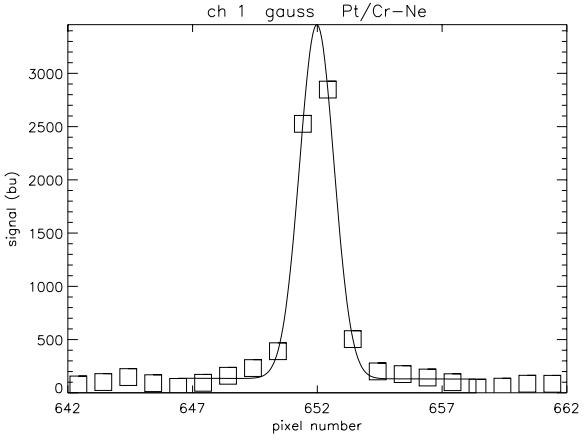
ch 1 gauss Pt/Cr-Ne
signal (bu)
pixel number
0
500
1000
1500
2000
2500
3000
642
647
652
657
662

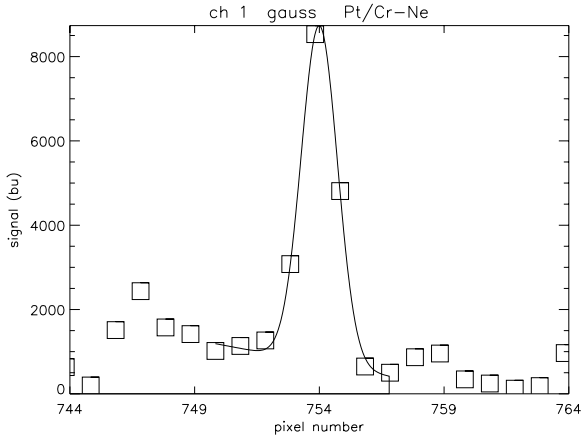

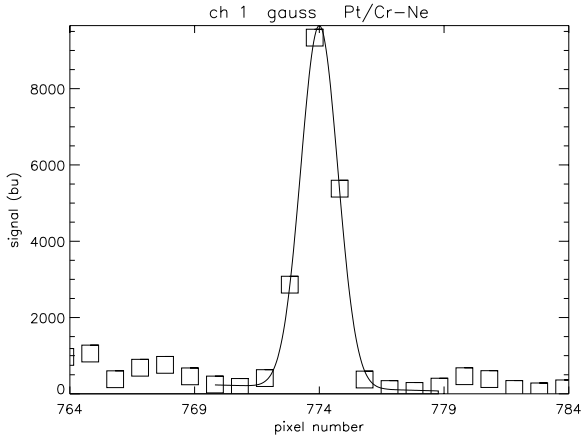

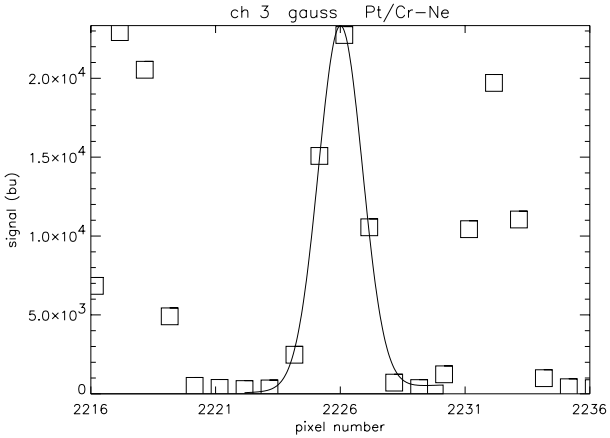

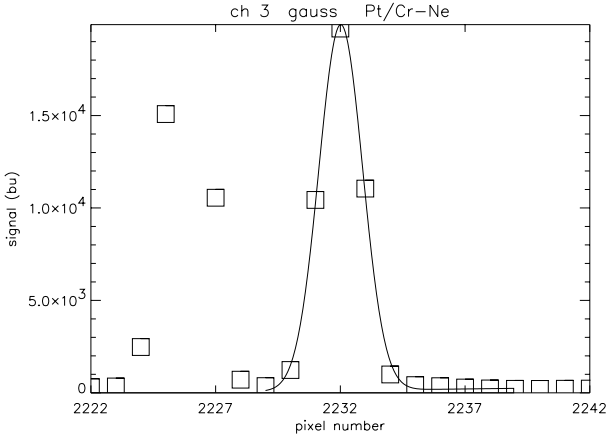

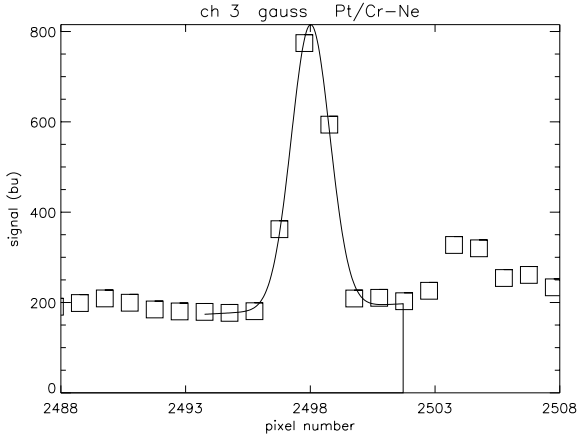

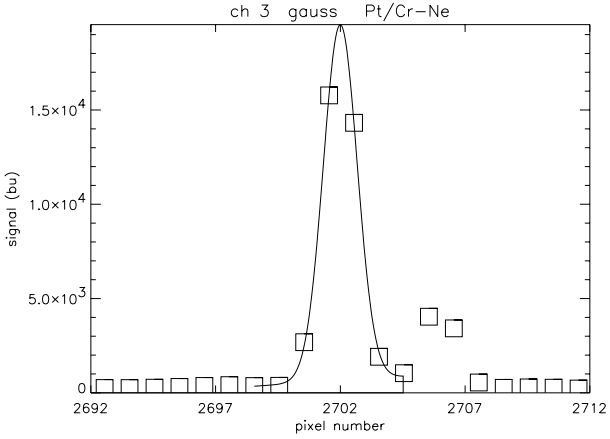

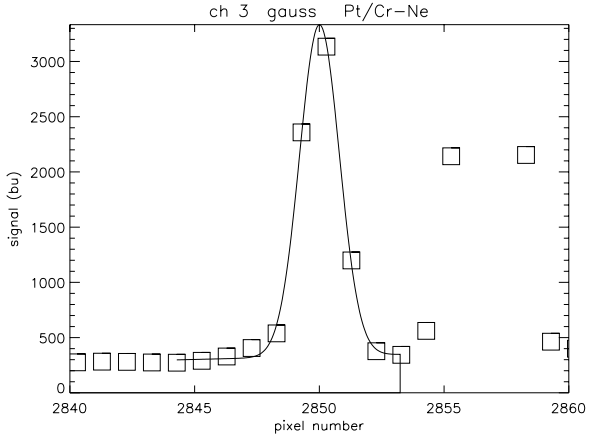

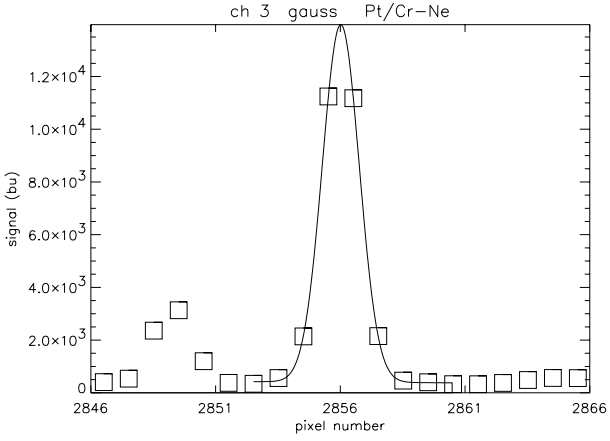

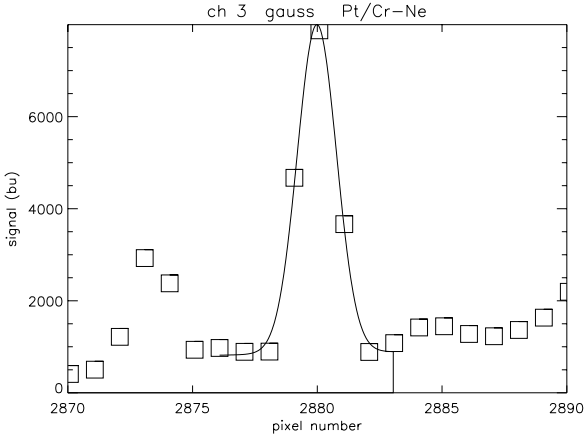

ch 1 gauss Pt/Cr-Ne
signal (bu)
pixel number
0
2000
4000
6000
8000
744
749
754
759
764
ch 1 gauss Pt/Cr-Ne
signal (bu)
pixel number
0
2000
4000
6000
8000
764
769
774
779
784
ch 3 gauss Pt/Cr-Ne
signal (bu)
pixel number
0
5.0×10^3
1.0×10^4
1.5×10^4
2.0×10^4
2216
2221
2226
2231
2236
ch 3 gauss Pt/Cr-Ne
signal (bu)
pixel number
0
5.0×10^3
1.0×10^4
1.5×10^4
2222
2227
2232
2237
2242
ch 3 gauss Pt/Cr-Ne
signal (bu)
pixel number
0
200
400
600
800
2488
2493
2498
2503
2508
ch 3 gauss Pt/Cr-Ne
signal (bu)
pixel number
0
5.0×10^3
1.0×10^4
1.5×10^4
2692
2697
2702
2707
2712
ch 3 gauss Pt/Cr-Ne
signal (bu)
pixel number
0
500
1000
1500
2000
2500
3000
2840
2845
2850
2855
2860
ch 3 gauss Pt/Cr-Ne
signal (bu)
pixel number
0
2.0×10^3
4.0×10^3
6.0×10^3
8.0×10^3
1.0×10^4
1.2×10^4
2846
2851
2856
2861
2866
ch 3 gauss Pt/Cr-Ne
signal (bu)
pixel number
0
2000
4000
6000
2870
2875
2880
2885
2890

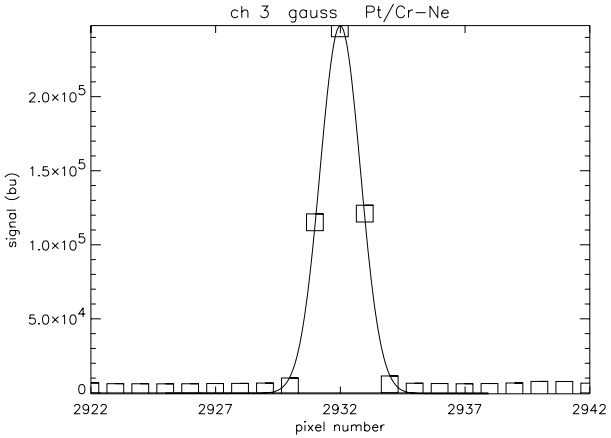
ch 3 gauss Pt/Cr−Ne

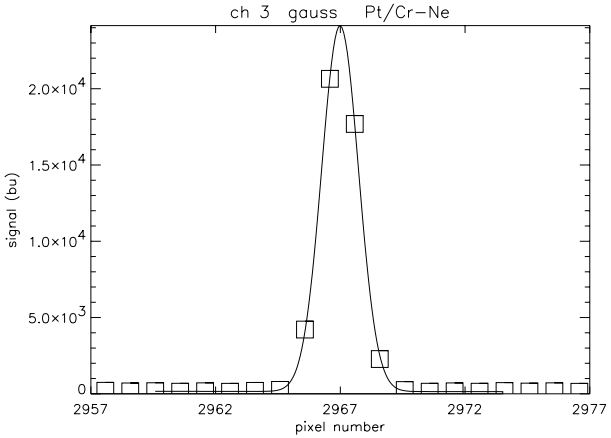
ch 3 gauss Pt/Cr−Ne

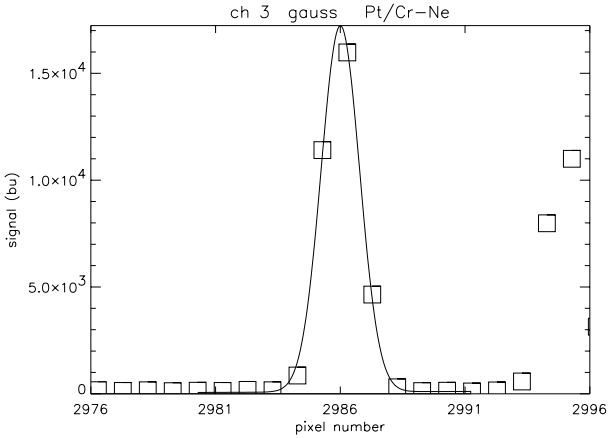
ch 3 gauss Pt/Cr−Ne

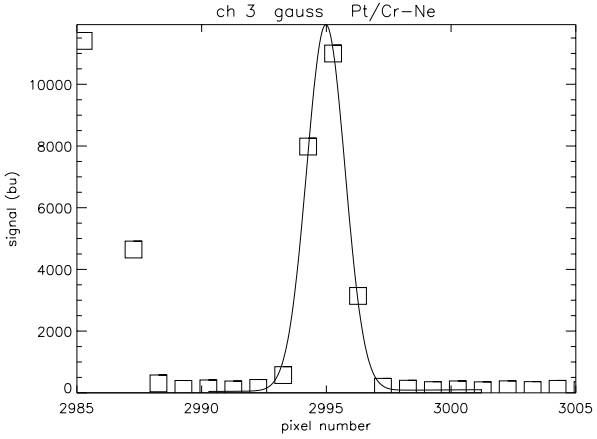
ch 3 gauss Pt/Cr−Ne

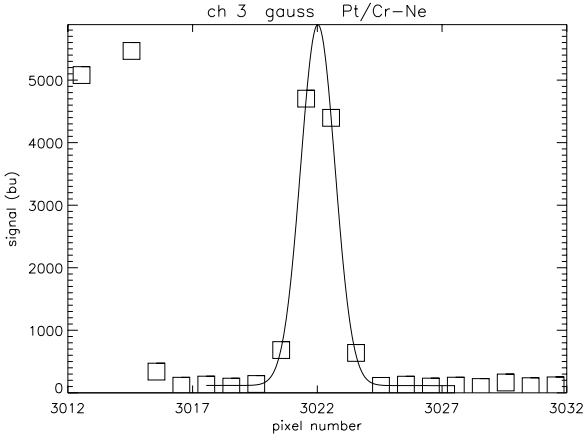
ch 3 gauss Pt/Cr−Ne

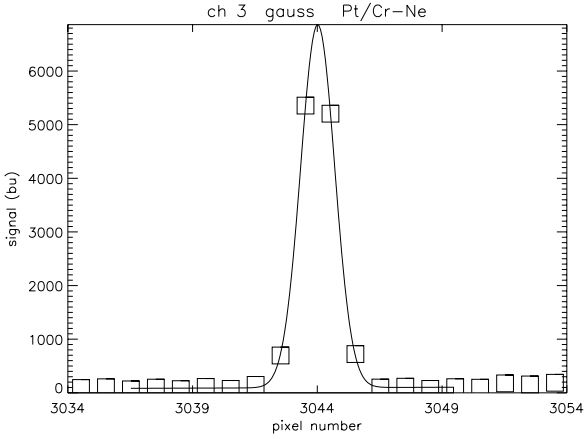
ch 3 gauss Pt/Cr−Ne

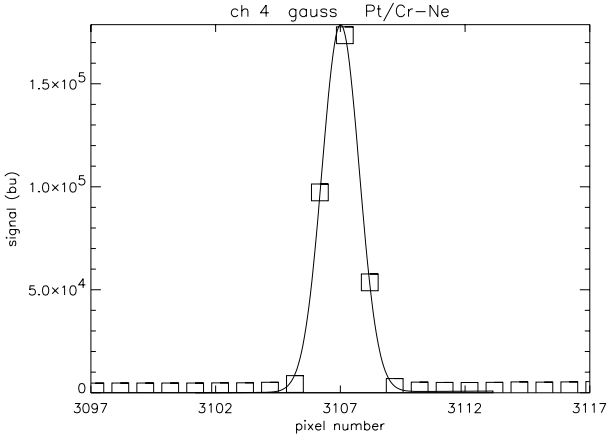
ch 4 gauss Pt/Cr−Ne

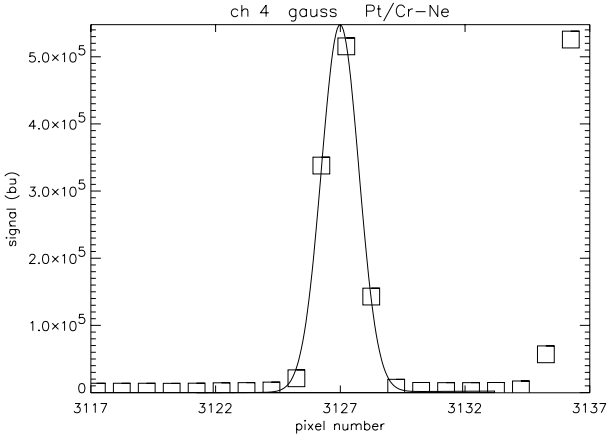
ch 4 gauss Pt/Cr−Ne

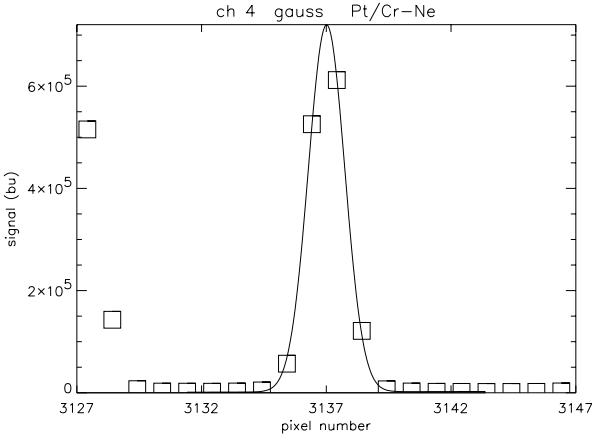
ch 4 gauss Pt/Cr−Ne

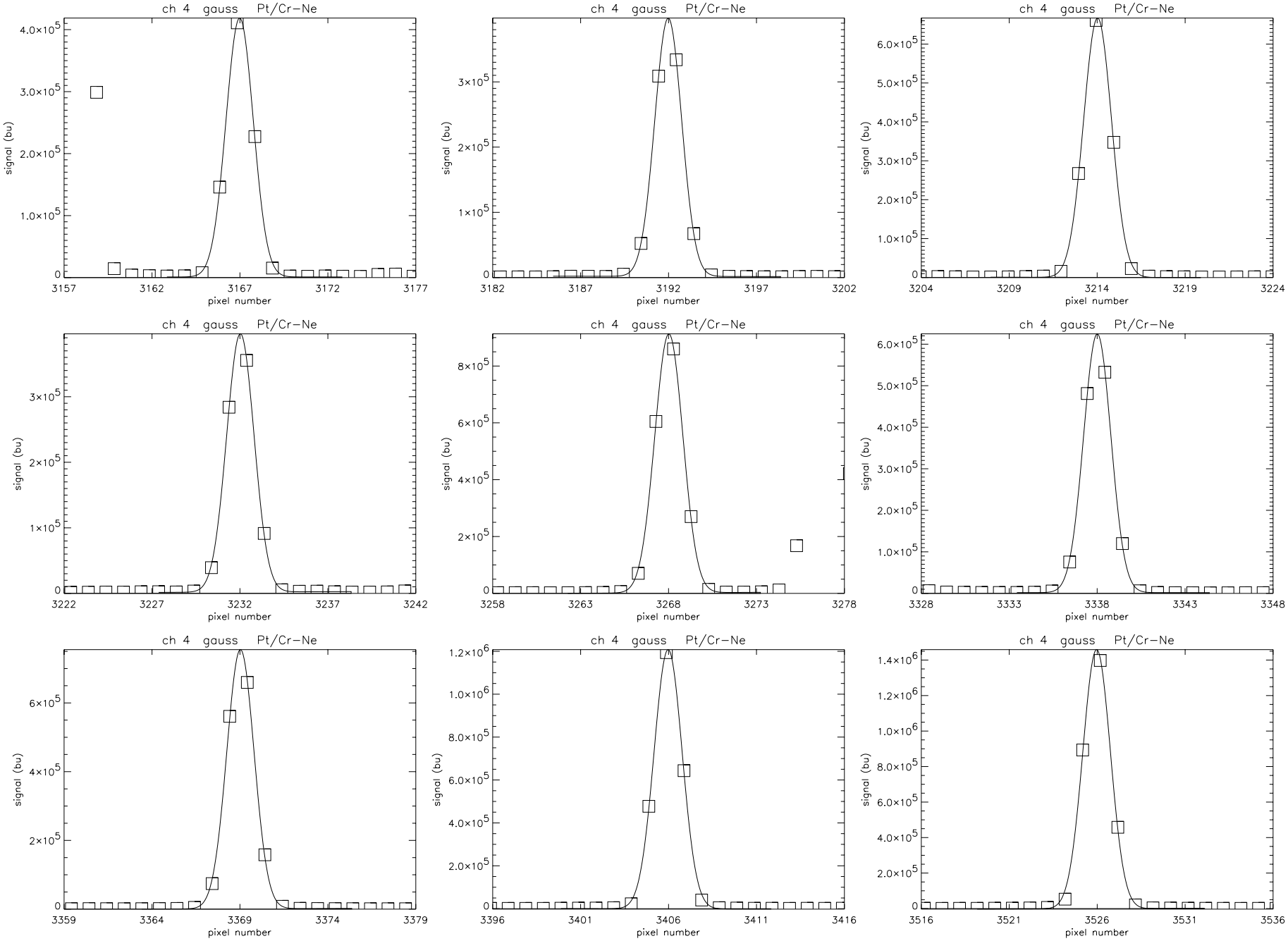
ch 4 gauss Pt/Cr-Ne
signal (bu)
pixel number
ch 4 gauss Pt/Cr-Ne
signal (bu)
pixel number
ch 4 gauss Pt/Cr-Ne
signal (bu)
pixel number
ch 4 gauss Pt/Cr-Ne
signal (bu)
pixel number
ch 4 gauss Pt/Cr-Ne
signal (bu)
pixel number
ch 4 gauss Pt/Cr-Ne
signal (bu)
pixel number
ch 4 gauss Pt/Cr-Ne
signal (bu)
pixel number
ch 4 gauss Pt/Cr-Ne
signal (bu)
pixel number
ch 4 gauss Pt/Cr-Ne
signal (bu)
pixel number

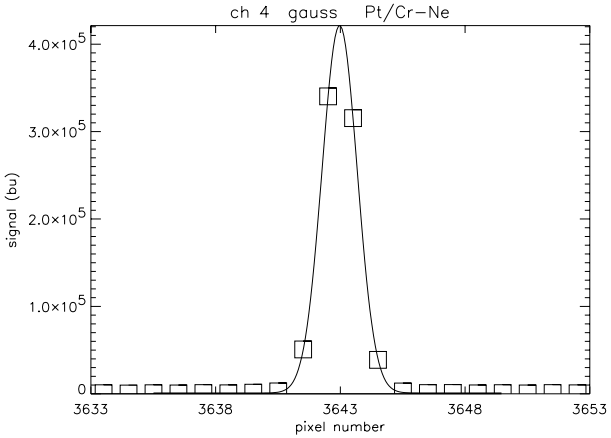
ch 4 gauss Pt/Cr-Ne
signal (bu)
0
1.0×10^5
2.0×10^5
3.0×10^5
4.0×10^5
3633
3638
3643
3648
3653
pixel number

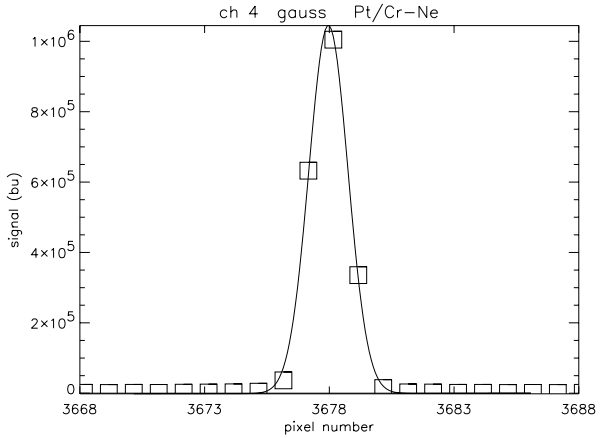
ch 4 gauss Pt/Cr-Ne
signal (bu)
0
2×10^5
4×10^5
6×10^5
8×10^5
1×10^6
3668
3673
3678
3683
3688
pixel number

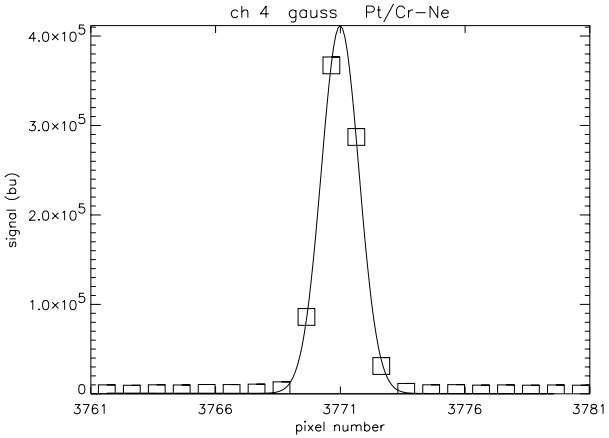
ch 4 gauss Pt/Cr-Ne
signal (bu)
0
1.0×10^5
2.0×10^5
3.0×10^5
4.0×10^5
3761
3766
3771
3776
3781
pixel number

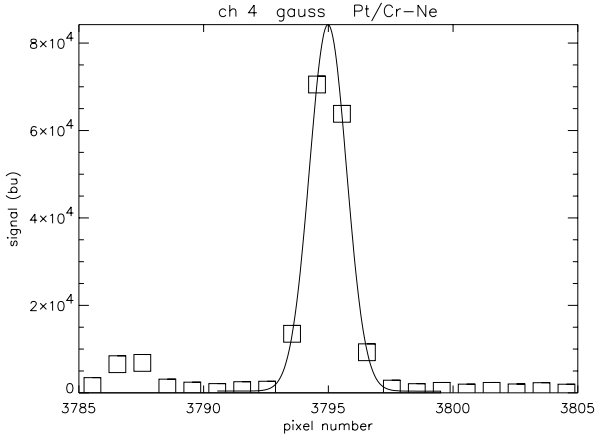
ch 4 gauss Pt/Cr-Ne
signal (bu)
0
2×10^4
4×10^4
6×10^4
8×10^4
3785
3790
3795
3800
3805
pixel number

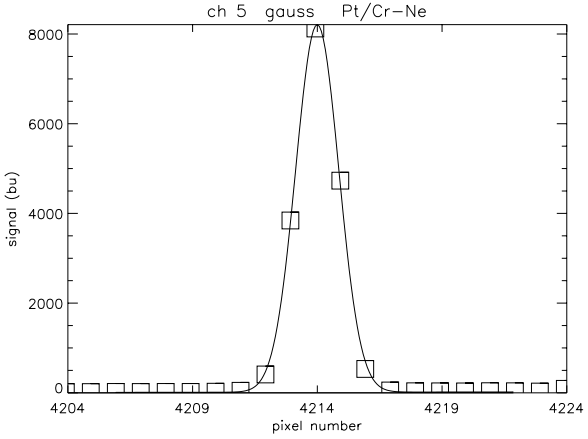
ch 5 gauss Pt/Cr-Ne
signal (bu)
0
2000
4000
6000
8000
4204
4209
4214
4219
4224
pixel number

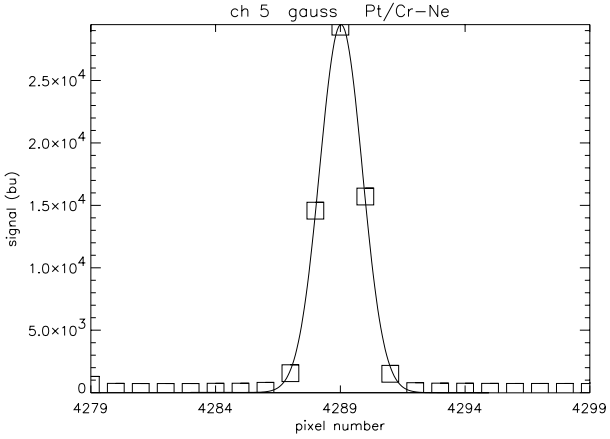
ch 5 gauss Pt/Cr-Ne
signal (bu)
0
5.0×10^3
1.0×10^4
1.5×10^4
2.0×10^4
2.5×10^4
4279
4284
4289
4294
4299
pixel number

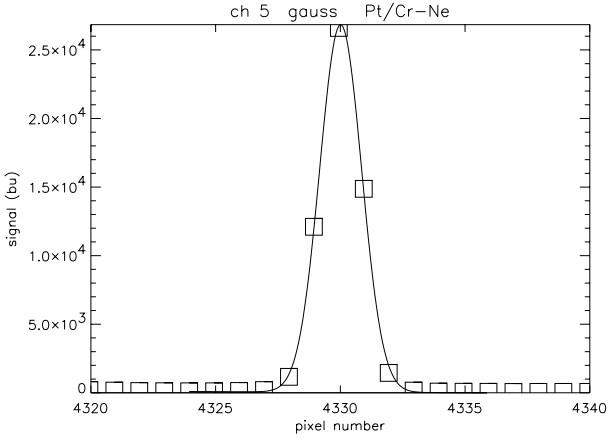
ch 5 gauss Pt/Cr-Ne
signal (bu)
0
5.0×10^3
1.0×10^4
1.5×10^4
2.0×10^4
2.5×10^4
4320
4325
4330
4335
4340
pixel number

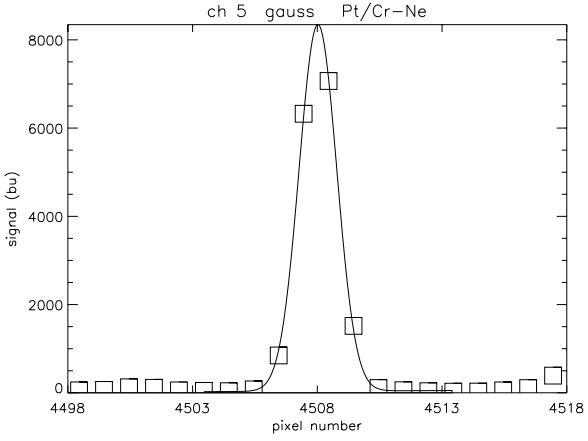
ch 5 gauss Pt/Cr-Ne
signal (bu)
0
2000
4000
6000
8000
4498
4503
4508
4513
4518
pixel number

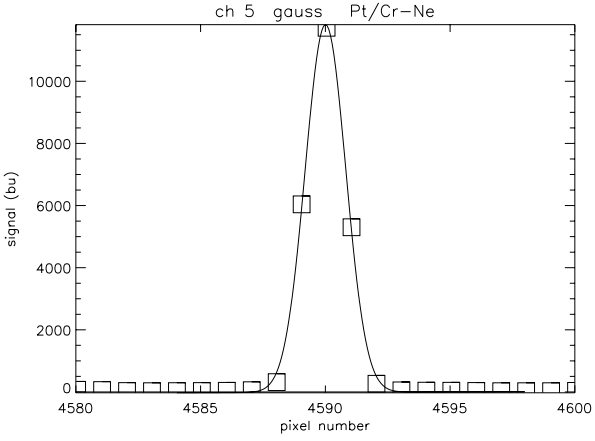
ch 5 gauss Pt/Cr-Ne
signal (bu)
0
2000
4000
6000
8000
10000
4580
4585
4590
4595
4600
pixel number

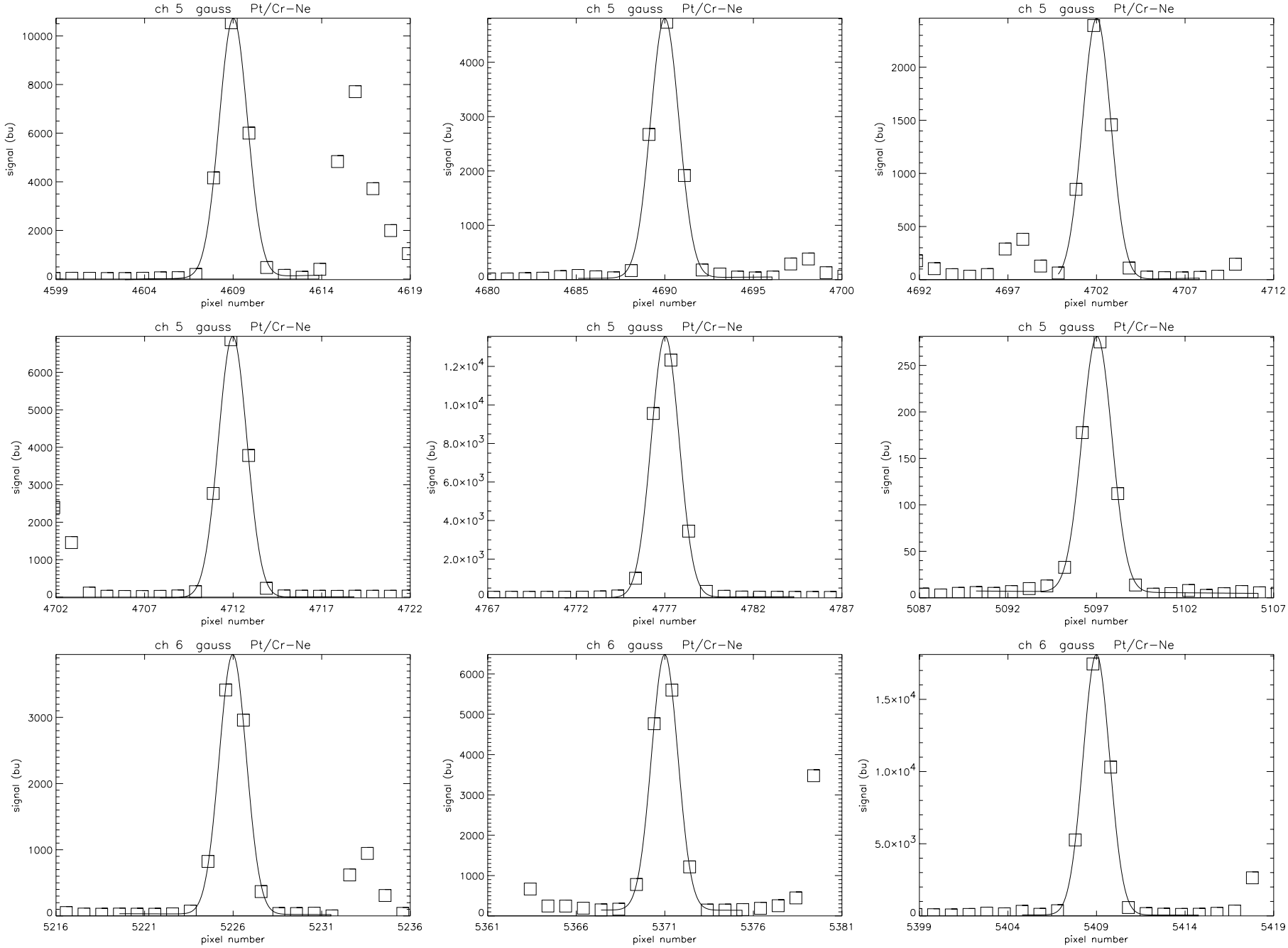
ch 5 gauss Pt/Cr-Ne
signal (bu)
pixel number
ch 5 gauss Pt/Cr-Ne
signal (bu)
pixel number
ch 5 gauss Pt/Cr-Ne
signal (bu)
pixel number
ch 5 gauss Pt/Cr-Ne
signal (bu)
pixel number
ch 5 gauss Pt/Cr-Ne
signal (bu)
pixel number
ch 5 gauss Pt/Cr-Ne
signal (bu)
pixel number
ch 6 gauss Pt/Cr-Ne
signal (bu)
pixel number
ch 6 gauss Pt/Cr-Ne
signal (bu)
pixel number
ch 6 gauss Pt/Cr-Ne
signal (bu)
pixel number

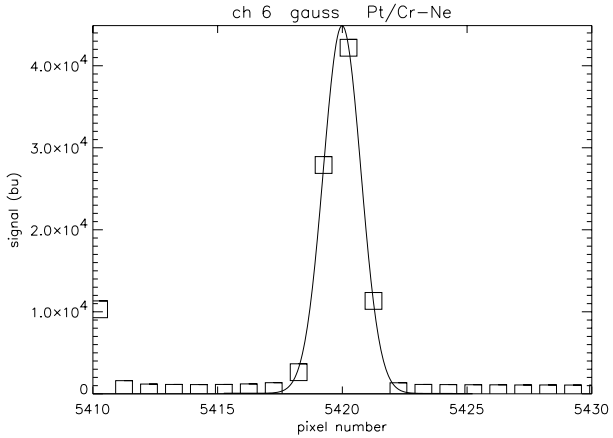
ch 6 gauss Pt/Cr−Ne
signal (bu)
0
1.0×10^4
2.0×10^4
3.0×10^4
4.0×10^4
5410
5415
5420
5425
5430
pixel number

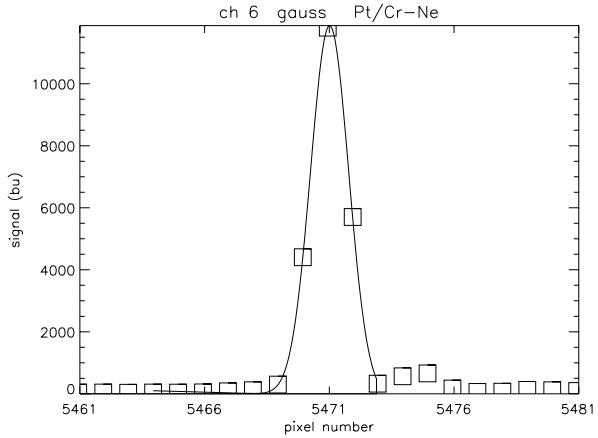
ch 6 gauss Pt/Cr−Ne
signal (bu)
0
2000
4000
6000
8000
10000
5461
5466
5471
5476
5481
pixel number

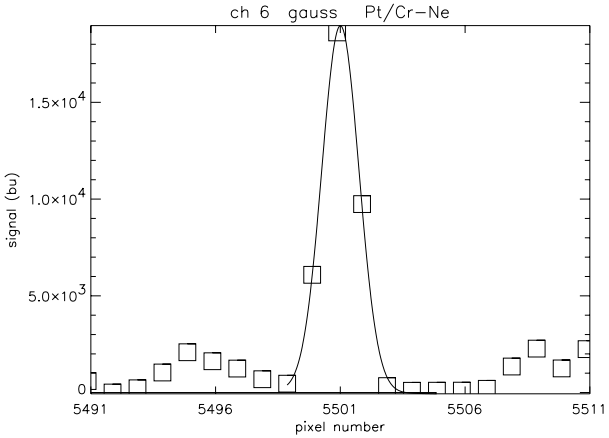
ch 6 gauss Pt/Cr−Ne
signal (bu)
0
5.0×10^3
1.0×10^4
1.5×10^4
5491
5496
5501
5506
5511
pixel number

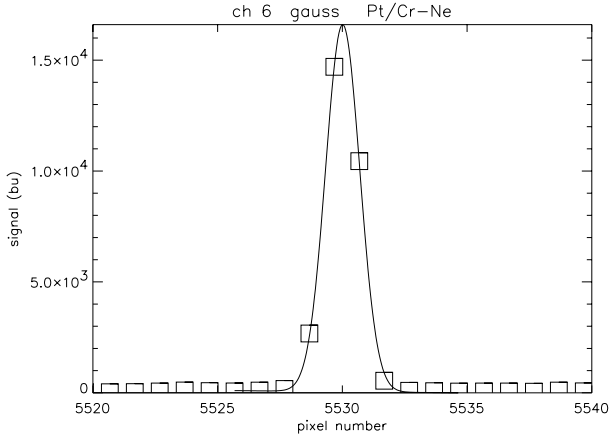
ch 6 gauss Pt/Cr−Ne
signal (bu)
0
5.0×10^3
1.0×10^4
1.5×10^4
5520
5525
5530
5535
5540
pixel number

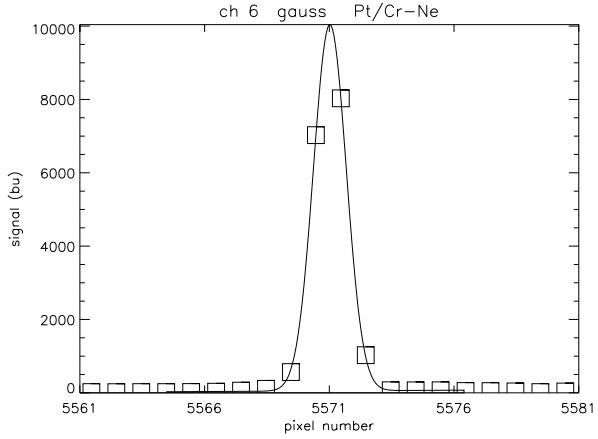
ch 6 gauss Pt/Cr−Ne
signal (bu)
0
2000
4000
6000
8000
10000
5561
5566
5571
5576
5581
pixel number

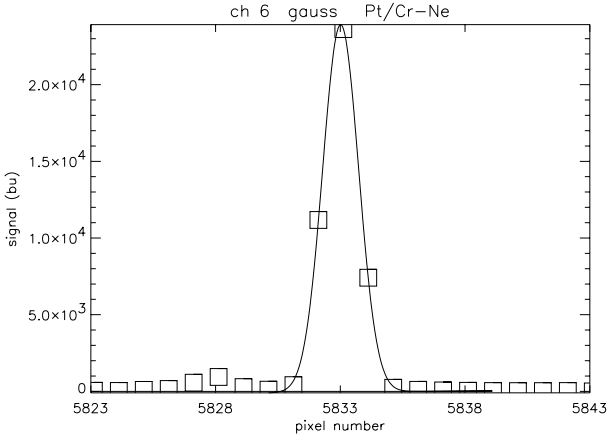
ch 6 gauss Pt/Cr−Ne
signal (bu)
0
5.0×10^3
1.0×10^4
1.5×10^4
2.0×10^4
5823
5828
5833
5838
5843
pixel number

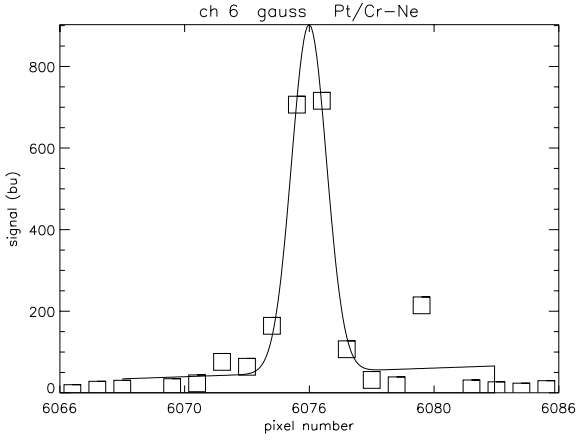
ch 6 gauss Pt/Cr−Ne
signal (bu)
0
200
400
600
800
6066
6070
6076
6080
6086
pixel number

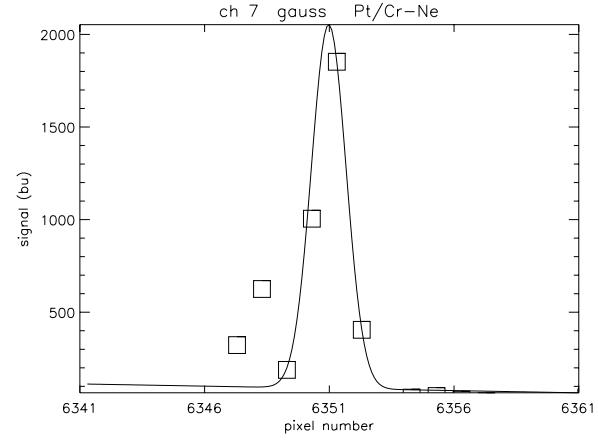
ch 7 gauss Pt/Cr−Ne
signal (bu)
500
1000
1500
2000
6341
6346
6351
6356
6361
pixel number

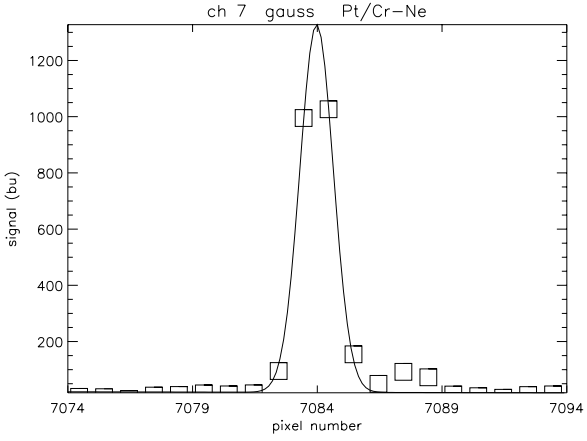
ch 7 gauss Pt/Cr−Ne
signal (bu)
200
400
600
800
1000
1200
7074
7079
7084
7089
7094
pixel number

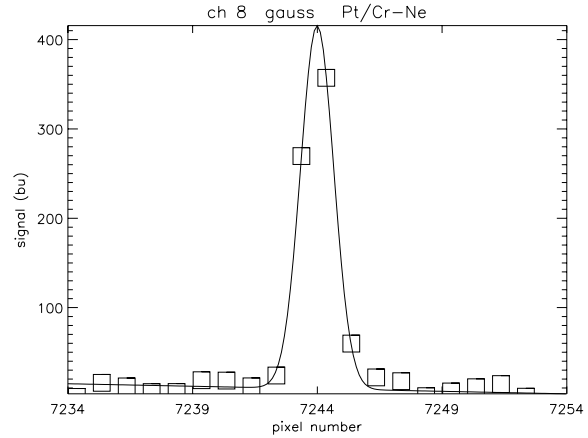
ch 8 gauss Pt/Cr-Ne
signal (bu)
pixel number
400
300
200
100
7234
7239
7244
7249
7254

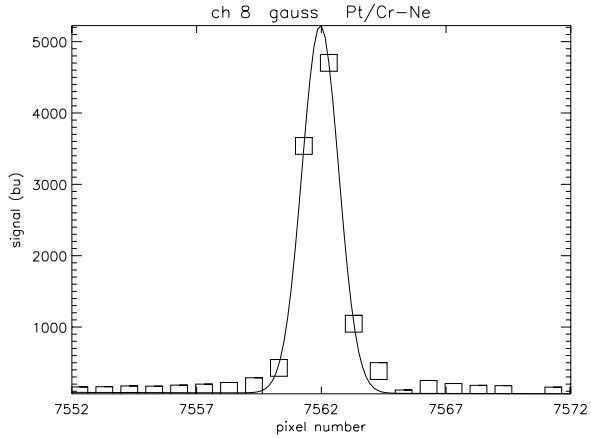
ch 8 gauss Pt/Cr-Ne
signal (bu)
pixel number
5000
4000
3000
2000
1000
7552
7557
7562
7567
7572

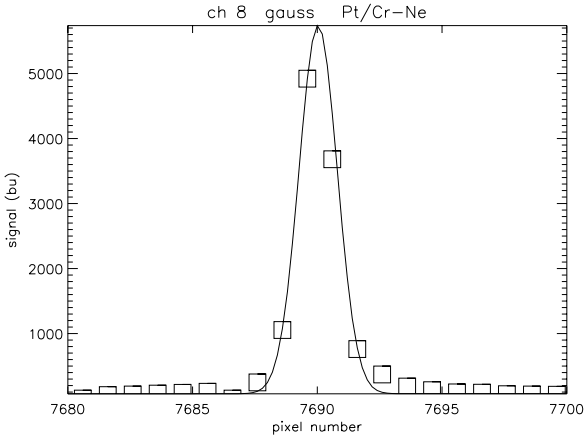
ch 8 gauss Pt/Cr-Ne
signal (bu)
pixel number
5000
4000
3000
2000
1000
7680
7685
7690
7695
7700

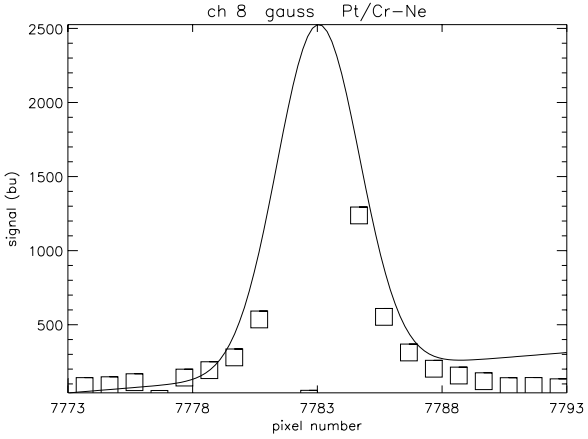
ch 8 gauss Pt/Cr-Ne
signal (bu)
pixel number
2500
2000
1500
1000
500
7773
7778
7783
7788
7793

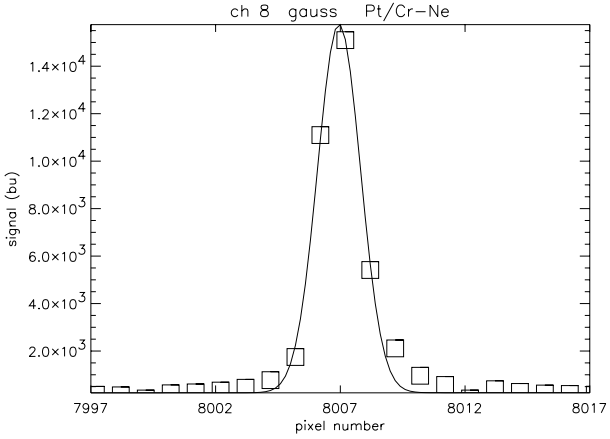
ch 8 gauss Pt/Cr-Ne
signal (bu)
pixel number
1.4×10^4
1.2×10^4
1.0×10^4
8.0×10^3
6.0×10^3
4.0×10^3
2.0×10^3
7997
8002
8007
8012
8017

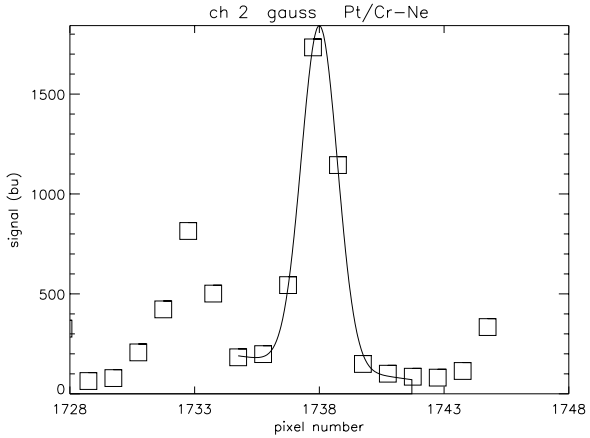
ch 2 gauss Pt/Cr-Ne
signal (bu)
pixel number
0
500
1000
1500
1728
1733
1738
1743
1748

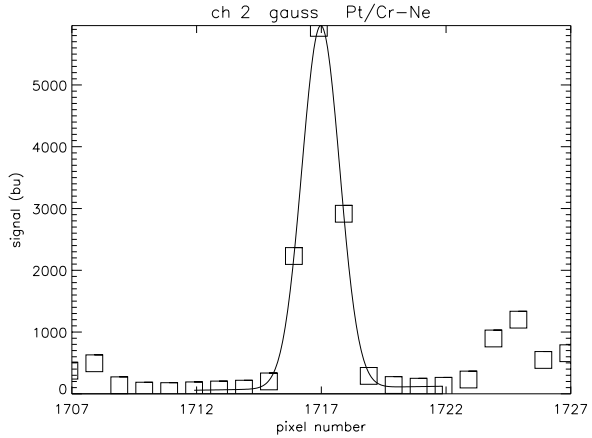
ch 2 gauss Pt/Cr-Ne
signal (bu)
pixel number
0
1000
2000
3000
4000
5000
1707
1712
1717
1722
1727

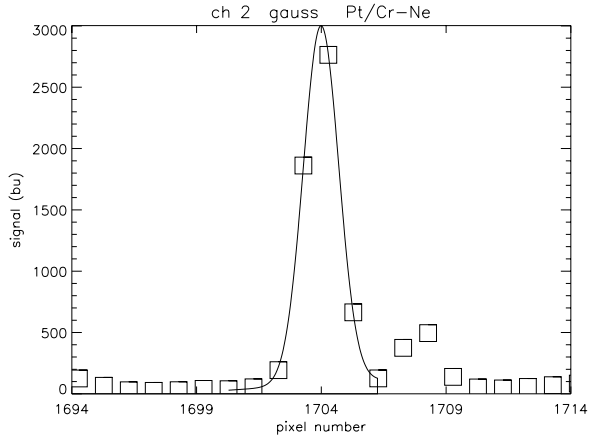
ch 2 gauss Pt/Cr-Ne
signal (bu)
pixel number
0
500
1000
1500
2000
2500
3000
1694
1699
1704
1709
1714

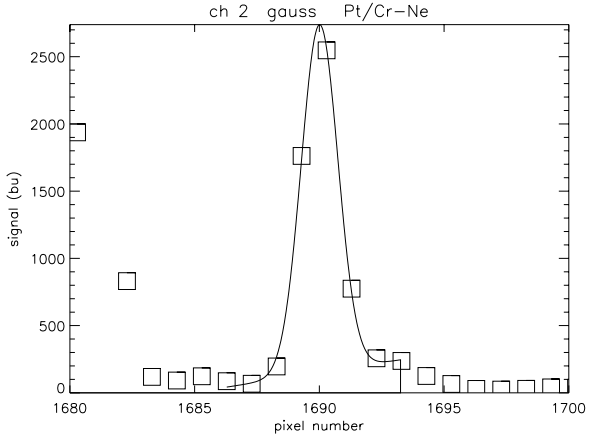
ch 2 gauss Pt/Cr-Ne
signal (bu)
pixel number
0
500
1000
1500
2000
2500
1680
1685
1690
1695
1700

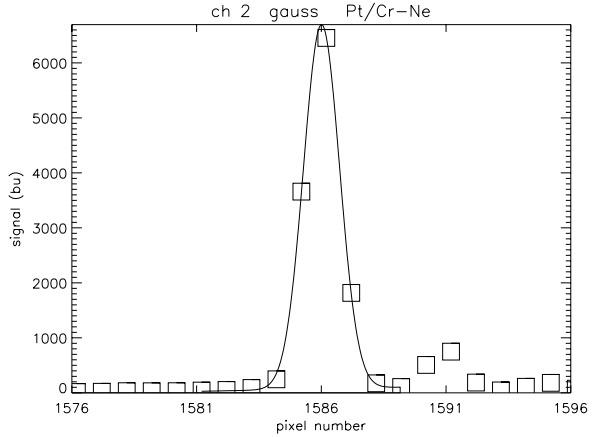
ch 2 gauss Pt/Cr-Ne
signal (bu)
pixel number
0
1000
2000
3000
4000
5000
6000
1576
1581
1586
1591
1596

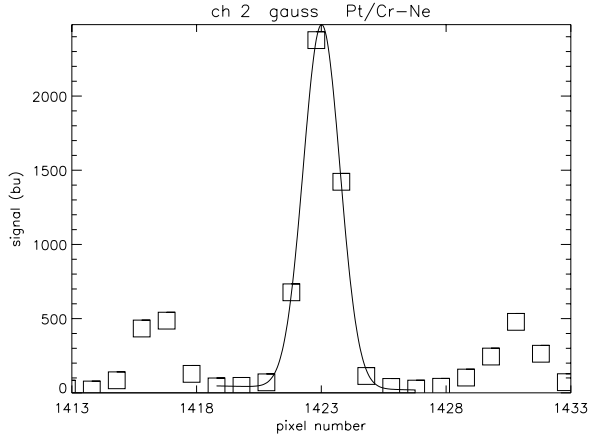
ch 2 gauss Pt/Cr-Ne
signal (bu)
pixel number
0
500
1000
1500
2000
1413
1418
1423
1428
1433

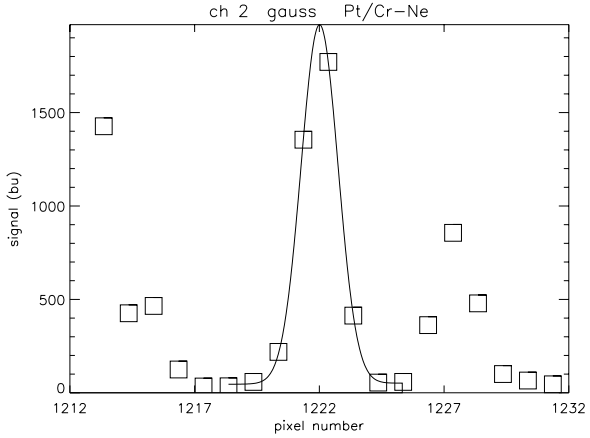
ch 2 gauss Pt/Cr-Ne
signal (bu)
pixel number
0
500
1000
1500
1212
1217
1222
1227
1232

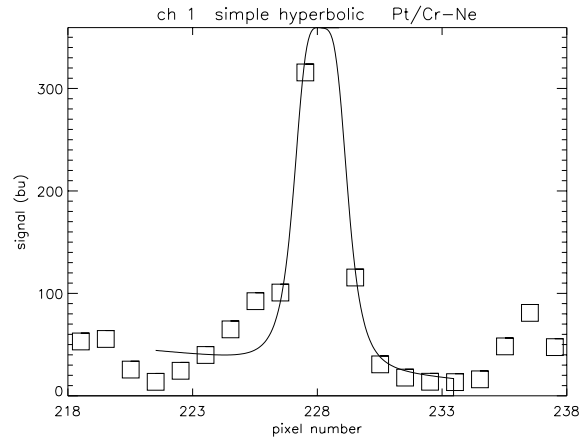
ch 1 simple hyperbolic Pt/Cr−Ne
signal (bu)
pixel number
0
100
200
300
218
223
228
233
238

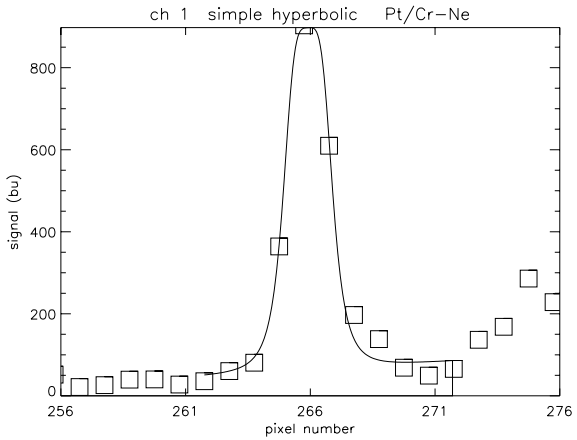
ch 1 simple hyperbolic Pt/Cr−Ne
signal (bu)
pixel number
0
200
400
600
800
256
261
266
271
276

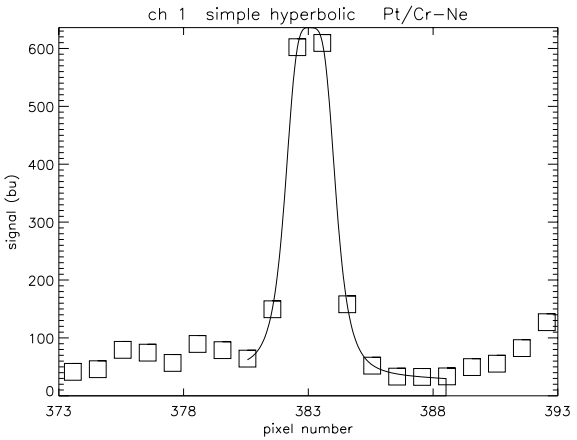
ch 1 simple hyperbolic Pt/Cr−Ne
signal (bu)
pixel number
0
100
200
300
400
500
600
373
378
383
388
393

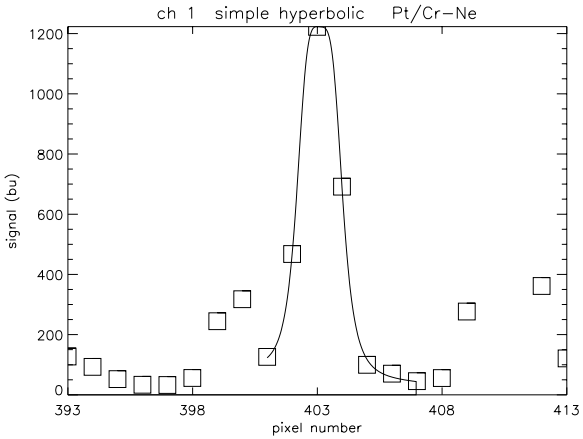
ch 1 simple hyperbolic Pt/Cr−Ne
signal (bu)
pixel number
0
200
400
600
800
1000
1200
393
398
403
408
413

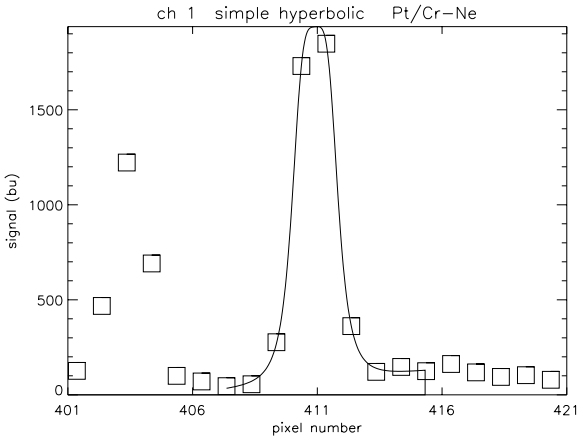
ch 1 simple hyperbolic Pt/Cr−Ne
signal (bu)
pixel number
0
500
1000
1500
401
406
411
416
421

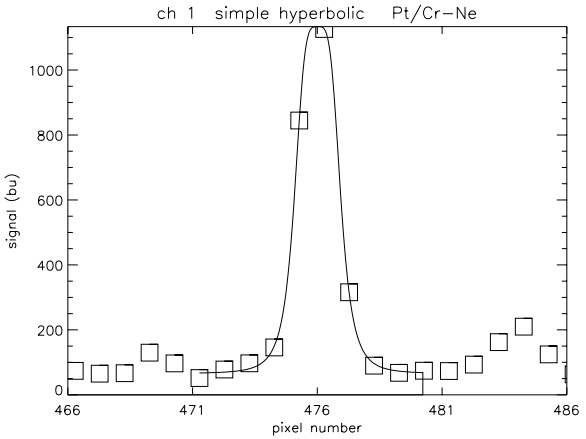
ch 1 simple hyperbolic Pt/Cr−Ne
signal (bu)
pixel number
0
200
400
600
800
1000
466
471
476
481
486

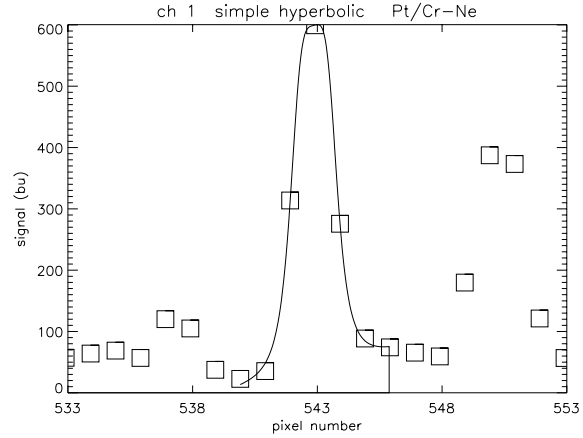
ch 1 simple hyperbolic Pt/Cr−Ne
signal (bu)
pixel number
0
100
200
300
400
500
600
533
538
543
548
553

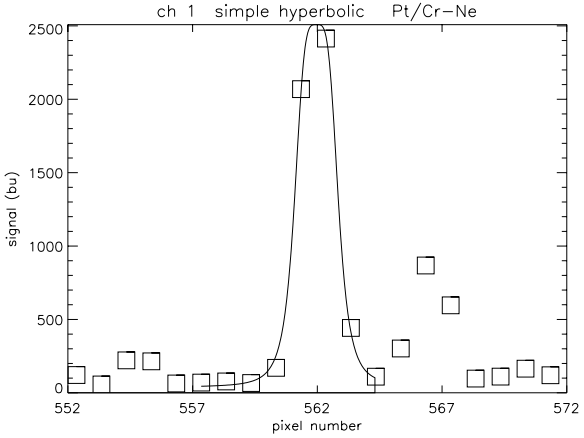
ch 1 simple hyperbolic Pt/Cr−Ne
signal (bu)
pixel number
0
500
1000
1500
2000
2500
552
557
562
567
572

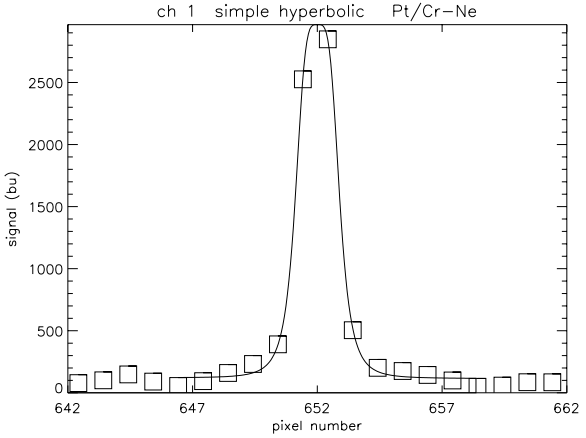
ch 1 simple hyperbolic Pt/Cr−Ne
signal (bu)
pixel number
0
500
1000
1500
2000
2500
642
647
652
657
662

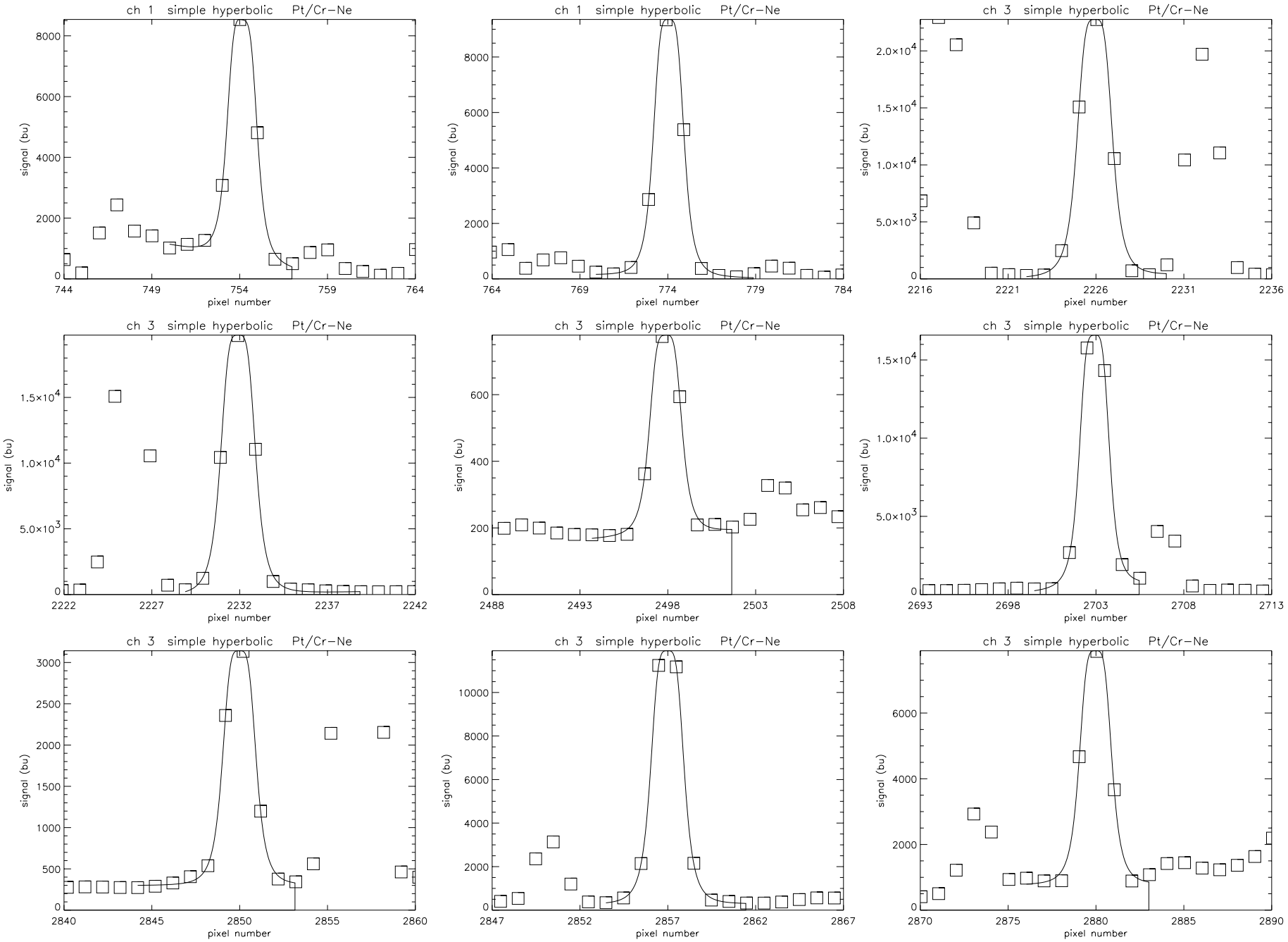
ch 1 simple hyperbolic Pt/Cr−Ne
signal (bu)
pixel number
ch 1 simple hyperbolic Pt/Cr−Ne
signal (bu)
pixel number
ch 3 simple hyperbolic Pt/Cr−Ne
signal (bu)
pixel number
ch 3 simple hyperbolic Pt/Cr−Ne
signal (bu)
pixel number
ch 3 simple hyperbolic Pt/Cr−Ne
signal (bu)
pixel number
ch 3 simple hyperbolic Pt/Cr−Ne
signal (bu)
pixel number
ch 3 simple hyperbolic Pt/Cr−Ne
signal (bu)
pixel number
ch 3 simple hyperbolic Pt/Cr−Ne
signal (bu)
pixel number
ch 3 simple hyperbolic Pt/Cr−Ne
signal (bu)
pixel number

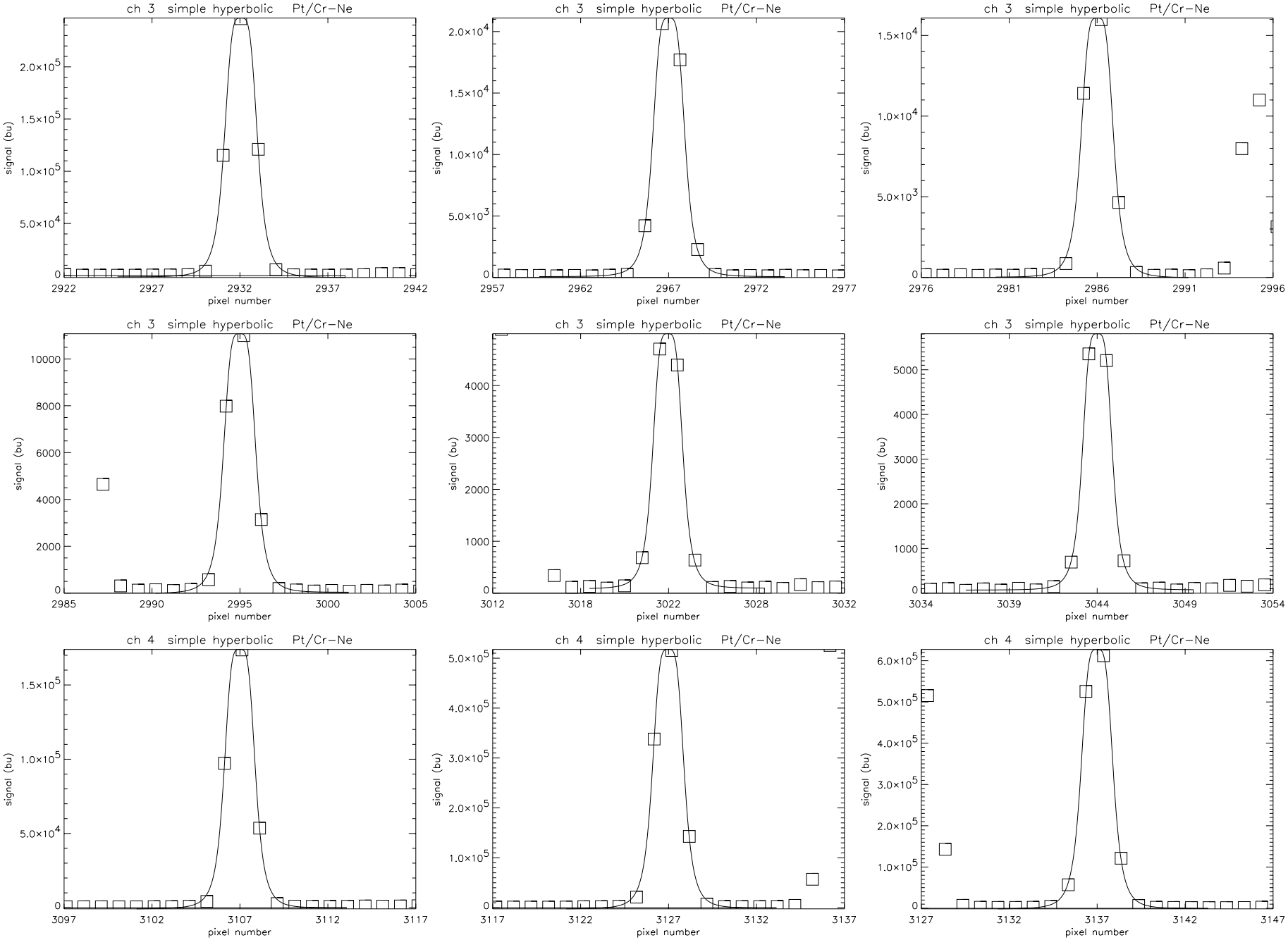
ch 3 simple hyperbolic Pt/Cr−Ne
signal (bu)
pixel number
ch 3 simple hyperbolic Pt/Cr−Ne
signal (bu)
pixel number
ch 3 simple hyperbolic Pt/Cr−Ne
signal (bu)
pixel number
ch 3 simple hyperbolic Pt/Cr−Ne
signal (bu)
pixel number
ch 3 simple hyperbolic Pt/Cr−Ne
signal (bu)
pixel number
ch 3 simple hyperbolic Pt/Cr−Ne
signal (bu)
pixel number
ch 4 simple hyperbolic Pt/Cr−Ne
signal (bu)
pixel number
ch 4 simple hyperbolic Pt/Cr−Ne
signal (bu)
pixel number
ch 4 simple hyperbolic Pt/Cr−Ne
signal (bu)
pixel number

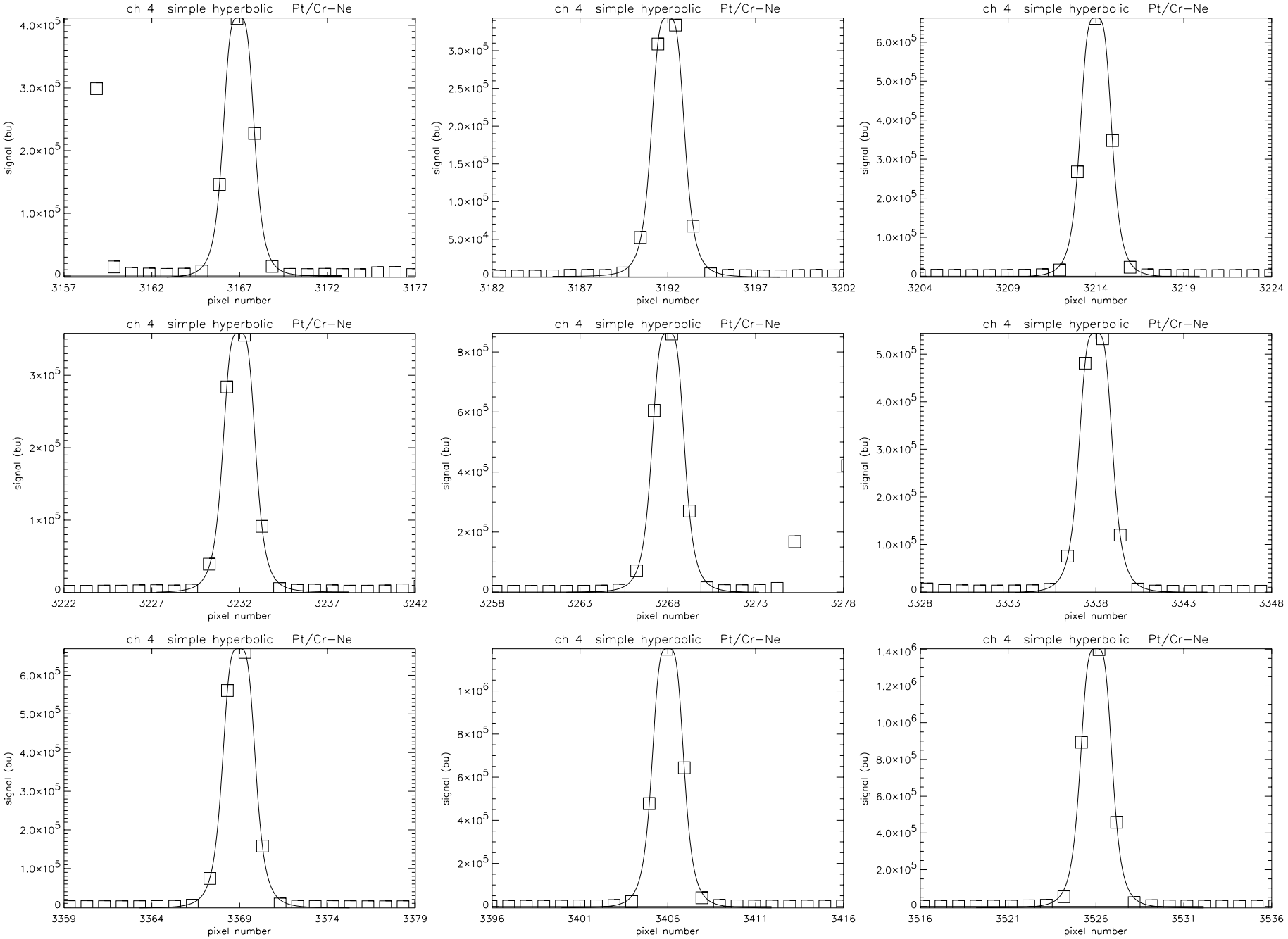
ch 4 simple hyperbolic Pt/Cr−Ne
signal (bu)
pixel number
ch 4 simple hyperbolic Pt/Cr−Ne
signal (bu)
pixel number
ch 4 simple hyperbolic Pt/Cr−Ne
signal (bu)
pixel number
ch 4 simple hyperbolic Pt/Cr−Ne
signal (bu)
pixel number
ch 4 simple hyperbolic Pt/Cr−Ne
signal (bu)
pixel number
ch 4 simple hyperbolic Pt/Cr−Ne
signal (bu)
pixel number
ch 4 simple hyperbolic Pt/Cr−Ne
signal (bu)
pixel number
ch 4 simple hyperbolic Pt/Cr−Ne
signal (bu)
pixel number
ch 4 simple hyperbolic Pt/Cr−Ne
signal (bu)
pixel number

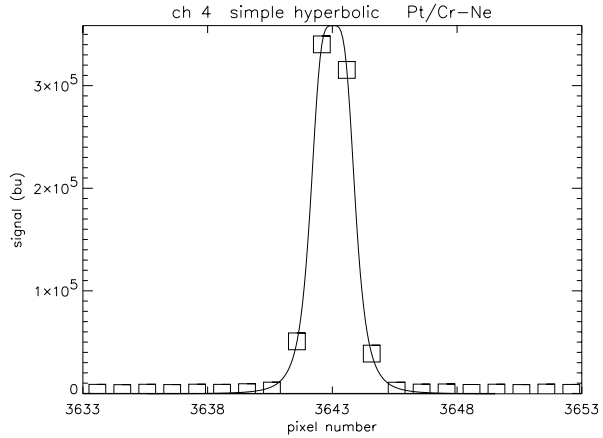
ch 4 simple hyperbolic Pt/Cr−Ne
signal (bu)
pixel number
0
1×10^5
2×10^5
3×10^5
3633
3638
3643
3648
3653

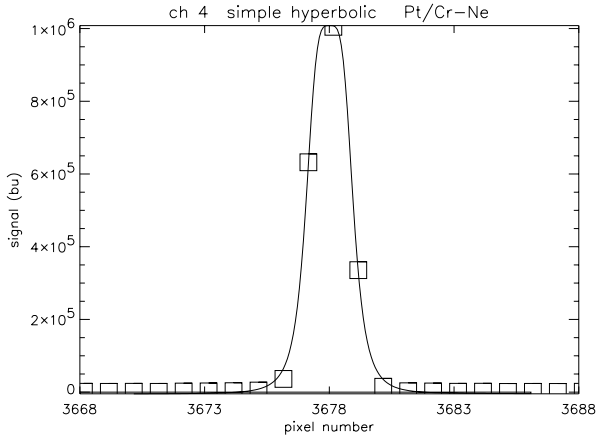
ch 4 simple hyperbolic Pt/Cr−Ne
signal (bu)
pixel number
0
2×10^5
4×10^5
6×10^5
8×10^5
1×10^6
3668
3673
3678
3683
3688

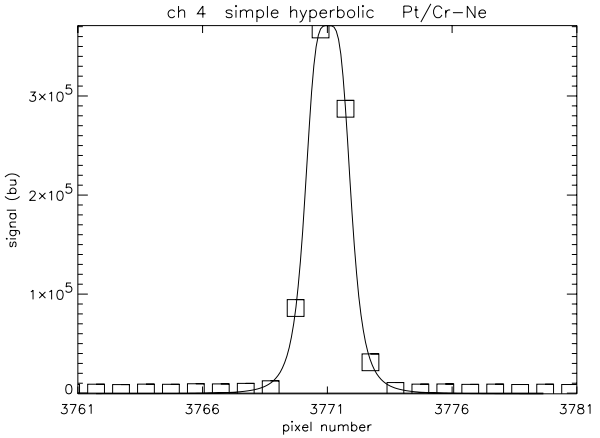
ch 4 simple hyperbolic Pt/Cr−Ne
signal (bu)
pixel number
0
1×10^5
2×10^5
3×10^5
3761
3766
3771
3776
3781

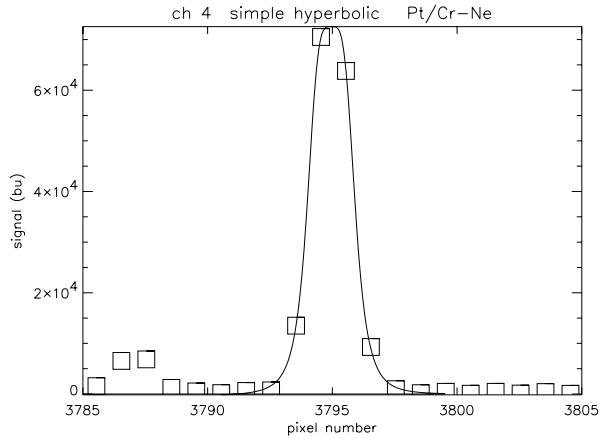
ch 4 simple hyperbolic Pt/Cr−Ne
signal (bu)
pixel number
0
2×10^4
4×10^4
6×10^4
3785
3790
3795
3800
3805

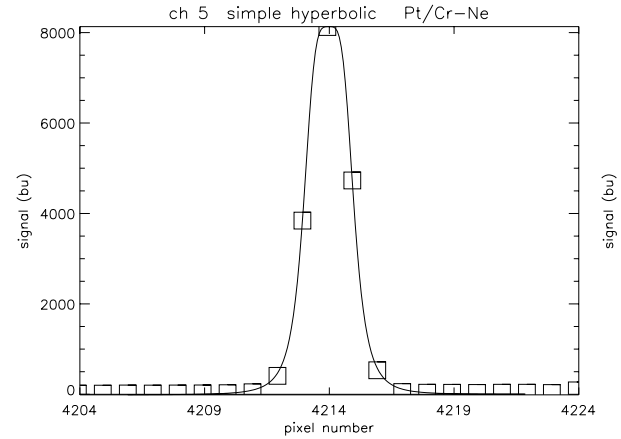
ch 5 simple hyperbolic Pt/Cr−Ne
signal (bu)
pixel number
0
2000
4000
6000
8000
4204
4209
4214
4219
4224

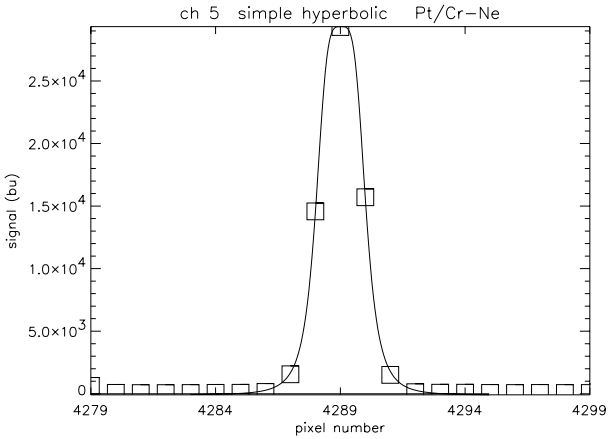
ch 5 simple hyperbolic Pt/Cr−Ne
signal (bu)
pixel number
0
5.0×10^3
1.0×10^4
1.5×10^4
2.0×10^4
2.5×10^4
4279
4284
4289
4294
4299

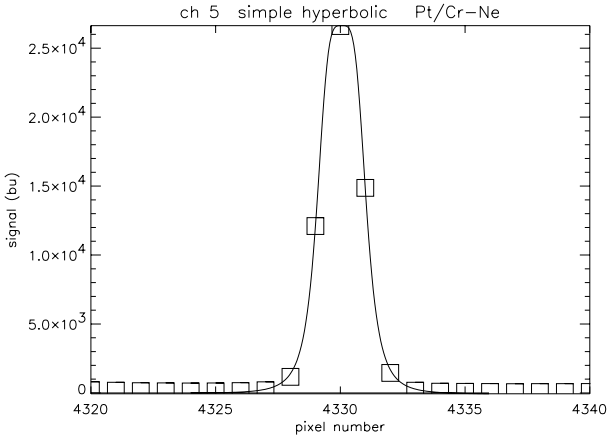
ch 5 simple hyperbolic Pt/Cr−Ne
signal (bu)
pixel number
0
5.0×10^3
1.0×10^4
1.5×10^4
2.0×10^4
2.5×10^4
4320
4325
4330
4335
4340

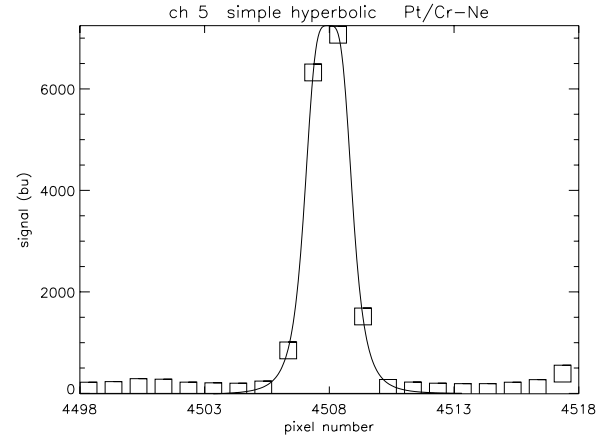
ch 5 simple hyperbolic Pt/Cr−Ne
signal (bu)
pixel number
0
2000
4000
6000
4498
4503
4508
4513
4518

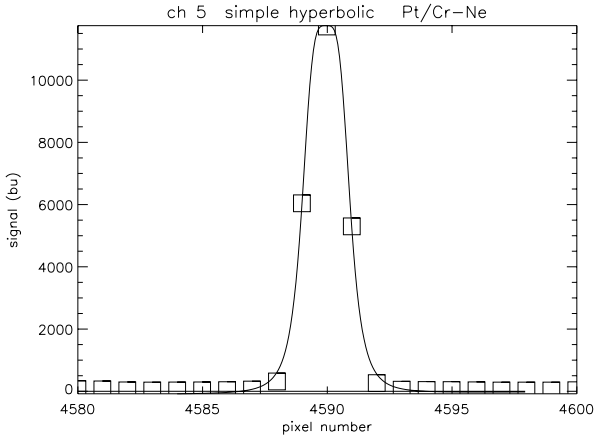
ch 5 simple hyperbolic Pt/Cr−Ne
signal (bu)
pixel number
0
2000
4000
6000
8000
10000
4580
4585
4590
4595
4600

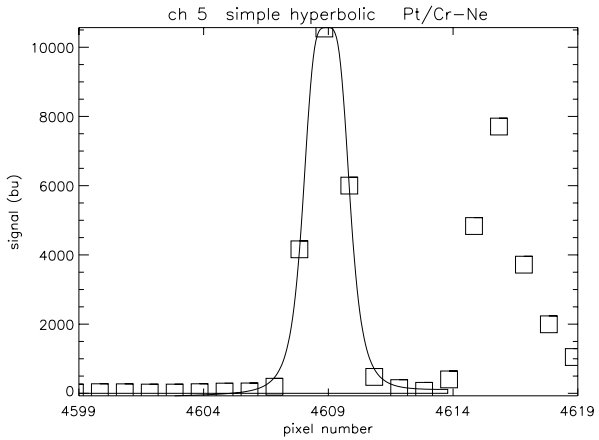
ch 5 simple hyperbolic Pt/Cr−Ne

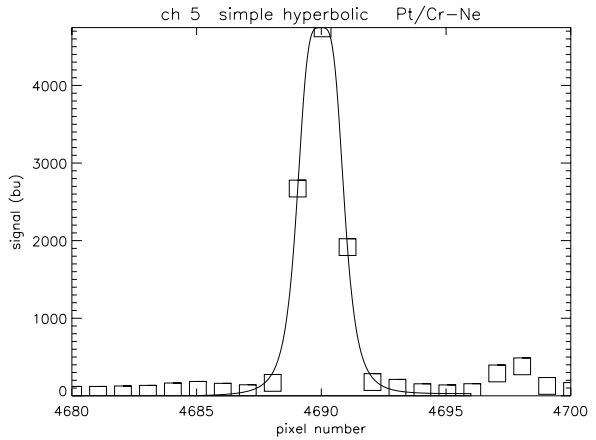
ch 5 simple hyperbolic Pt/Cr−Ne

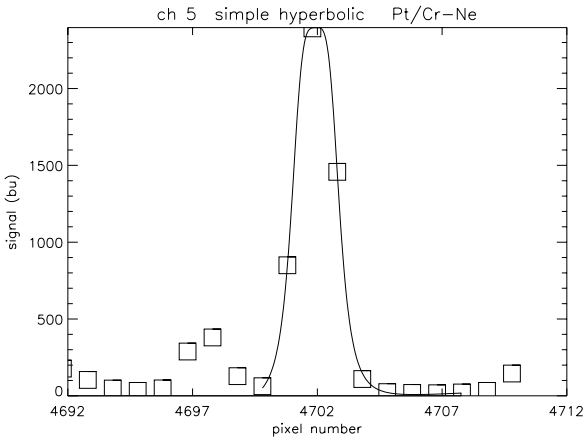
ch 5 simple hyperbolic Pt/Cr−Ne

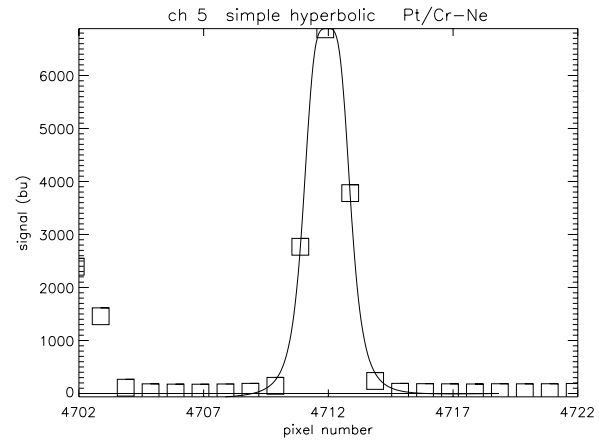
ch 5 simple hyperbolic Pt/Cr−Ne

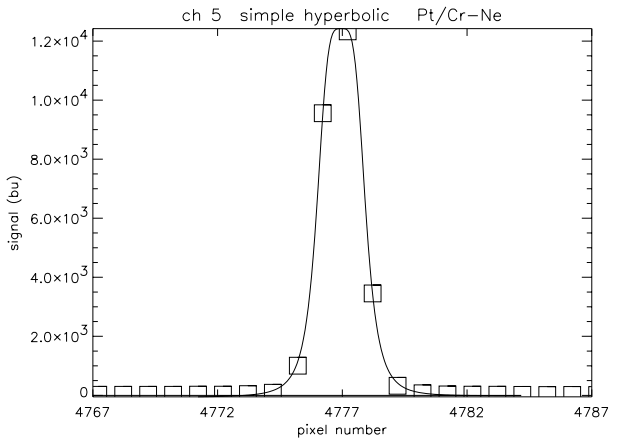
ch 5 simple hyperbolic Pt/Cr−Ne

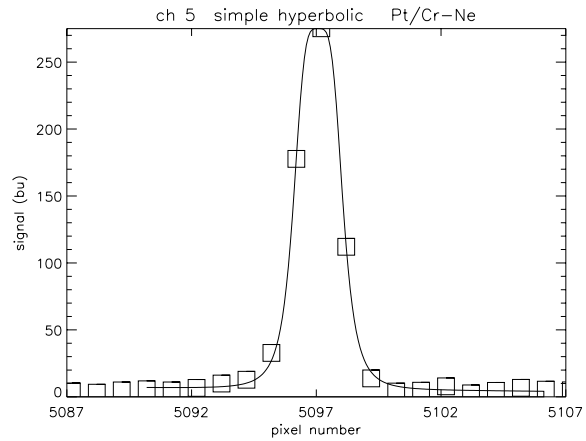
ch 5 simple hyperbolic Pt/Cr−Ne

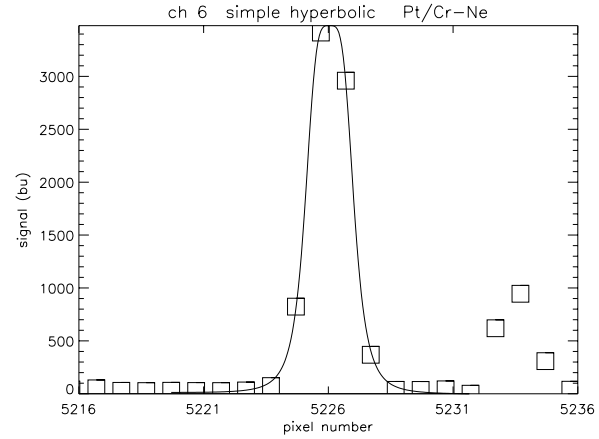
ch 6 simple hyperbolic Pt/Cr−Ne

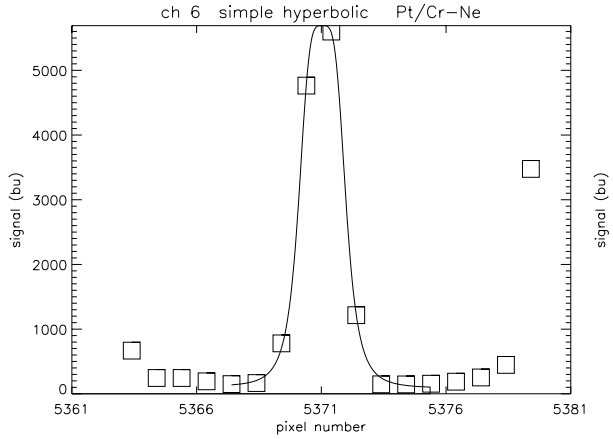
ch 6 simple hyperbolic Pt/Cr−Ne

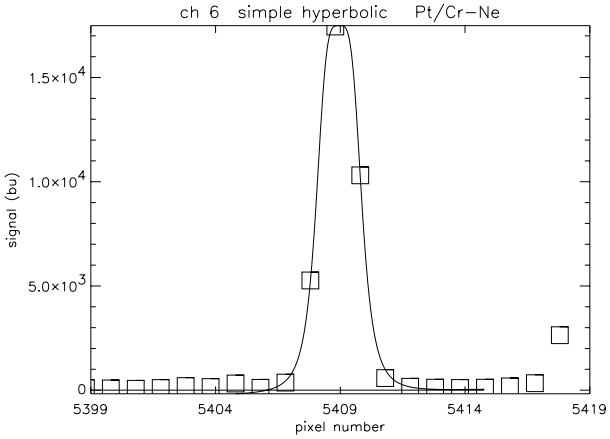
ch 6 simple hyperbolic Pt/Cr−Ne

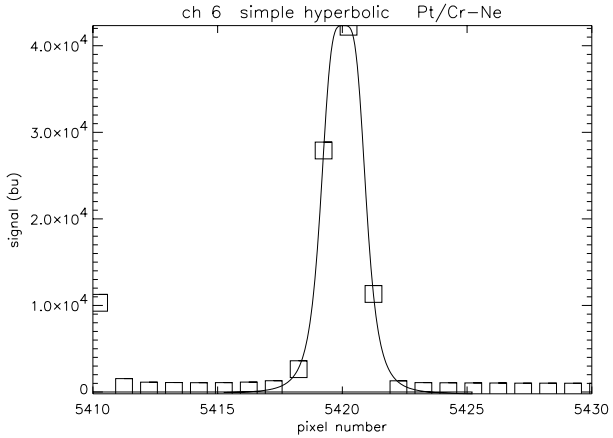
ch 6 simple hyperbolic Pt/Cr–Ne
signal (bu)
0
1.0×10^4
2.0×10^4
3.0×10^4
4.0×10^4
5410
5415
5420
5425
5430
pixel number

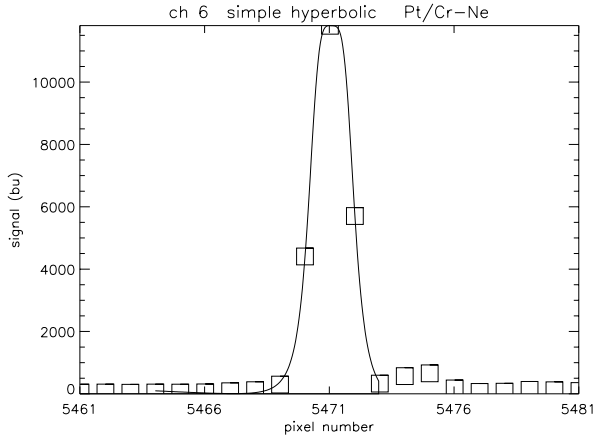
ch 6 simple hyperbolic Pt/Cr–Ne
signal (bu)
0
2000
4000
6000
8000
10000
5461
5466
5471
5476
5481
pixel number

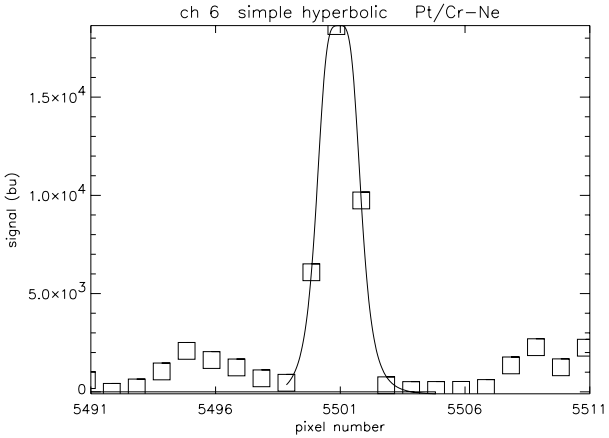
ch 6 simple hyperbolic Pt/Cr–Ne
signal (bu)
0
5.0×10^3
1.0×10^4
1.5×10^4
5491
5496
5501
5506
5511
pixel number

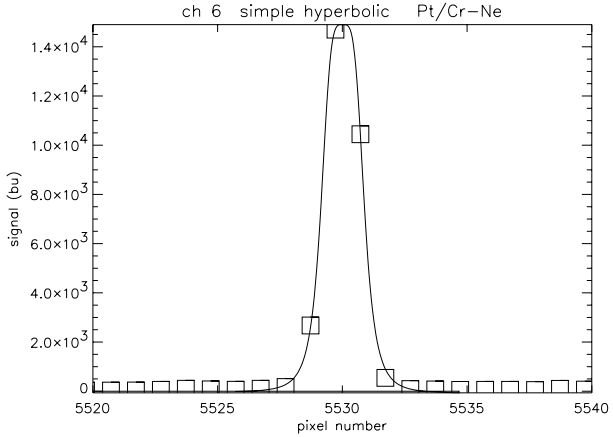
ch 6 simple hyperbolic Pt/Cr–Ne
signal (bu)
0
2.0×10^3
4.0×10^3
6.0×10^3
8.0×10^3
1.0×10^4
1.2×10^4
1.4×10^4
5520
5525
5530
5535
5540
pixel number

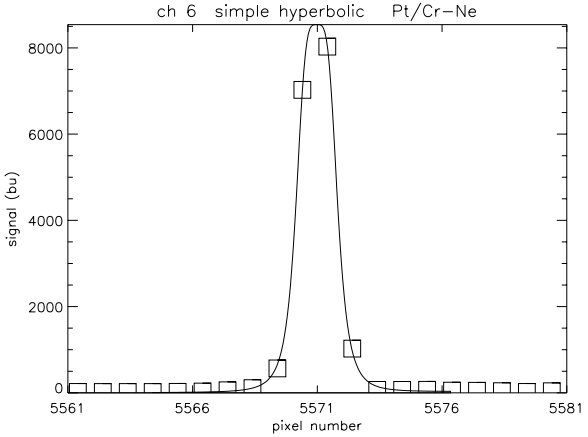
ch 6 simple hyperbolic Pt/Cr–Ne
signal (bu)
0
2000
4000
6000
8000
5561
5566
5571
5576
5581
pixel number

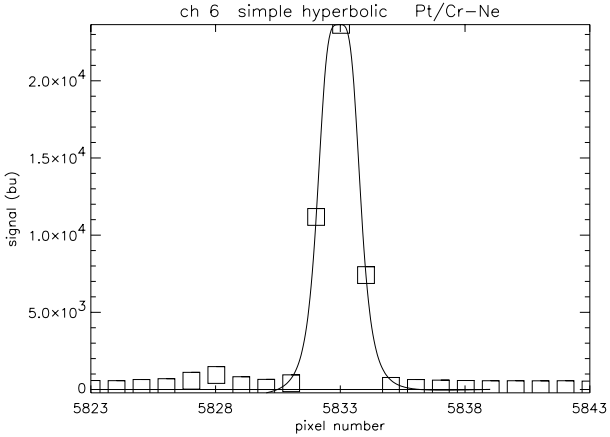
ch 6 simple hyperbolic Pt/Cr–Ne
signal (bu)
0
5.0×10^3
1.0×10^4
1.5×10^4
2.0×10^4
5823
5828
5833
5838
5843
pixel number

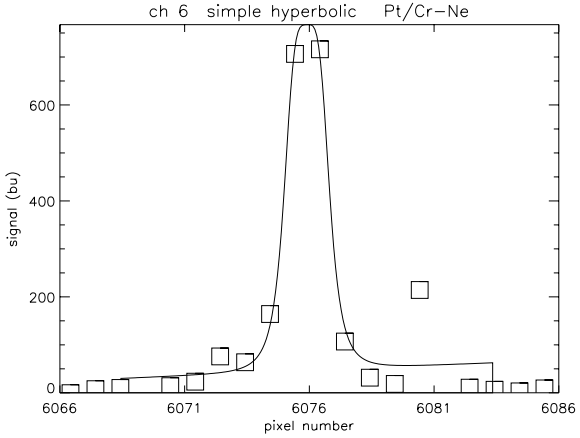
ch 6 simple hyperbolic Pt/Cr–Ne
signal (bu)
0
200
400
600
6066
6071
6076
6081
6086
pixel number

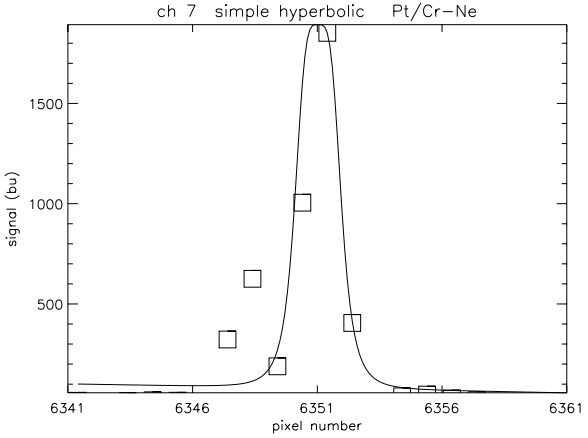
ch 7 simple hyperbolic Pt/Cr–Ne
signal (bu)
500
1000
1500
6341
6346
6351
6356
6361
pixel number

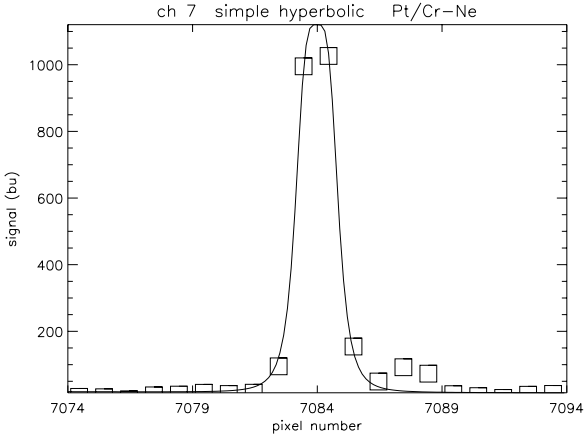
ch 7 simple hyperbolic Pt/Cr–Ne
signal (bu)
200
400
600
800
1000
7074
7079
7084
7089
7094
pixel number

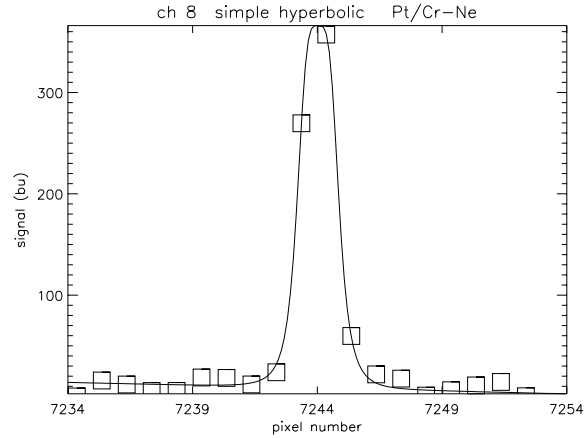
ch 8 simple hyperbolic Pt/Cr−Ne
signal (bu)
pixel number
7234
7239
7244
7249
7254
100
200
300

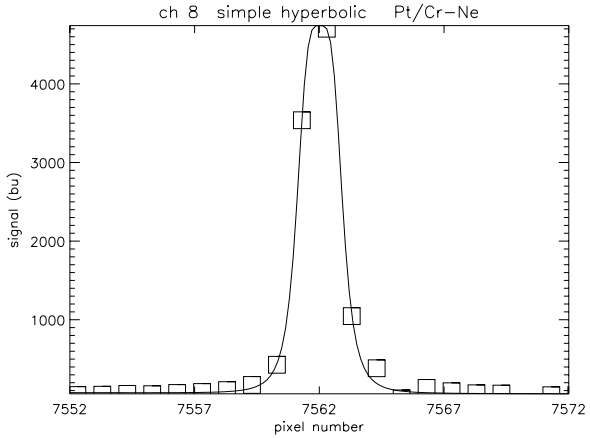
ch 8 simple hyperbolic Pt/Cr−Ne
signal (bu)
pixel number
7552
7557
7562
7567
7572
1000
2000
3000
4000

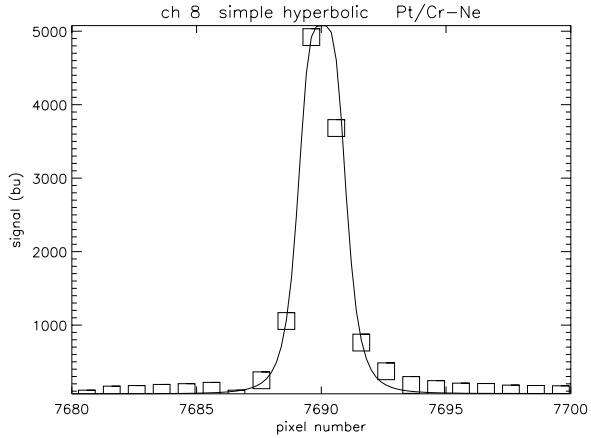
ch 8 simple hyperbolic Pt/Cr−Ne
signal (bu)
pixel number
7680
7685
7690
7695
7700
1000
2000
3000
4000
5000

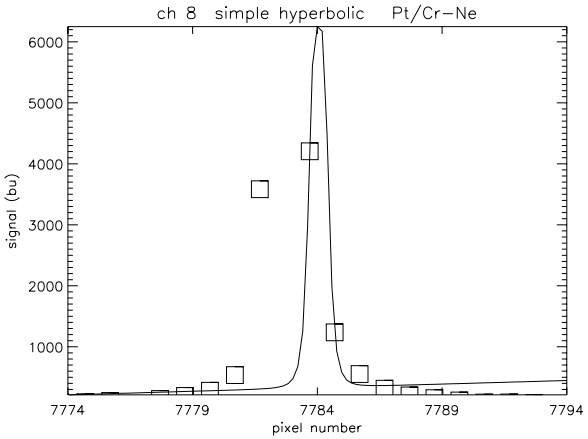
ch 8 simple hyperbolic Pt/Cr−Ne
signal (bu)
pixel number
7774
7779
7784
7789
7794
1000
2000
3000
4000
5000
6000

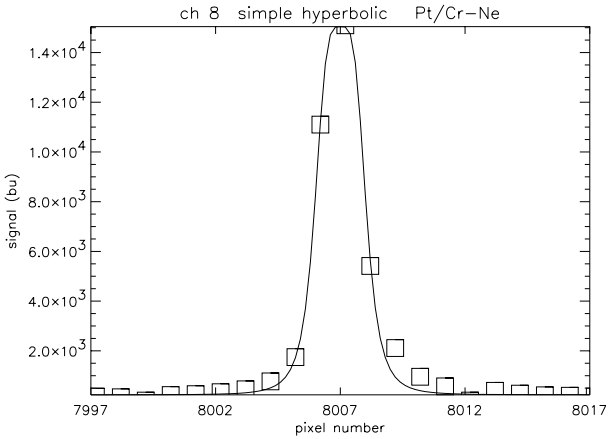
ch 8 simple hyperbolic Pt/Cr−Ne
signal (bu)
pixel number
7997
8002
8007
8012
8017
2.0×10^3
4.0×10^3
6.0×10^3
8.0×10^3
1.0×10^4
1.2×10^4
1.4×10^4

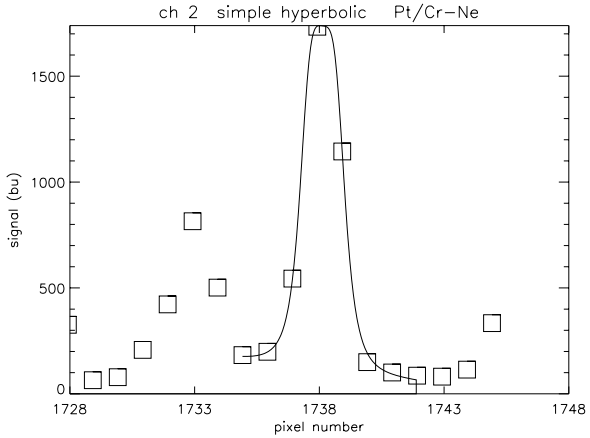
ch 2 simple hyperbolic Pt/Cr−Ne
signal (bu)
pixel number
0
500
1000
1500
1728
1733
1738
1743
1748

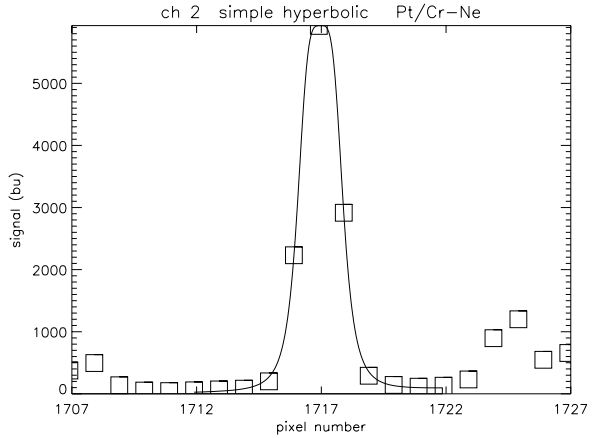
ch 2 simple hyperbolic Pt/Cr−Ne
signal (bu)
pixel number
0
1000
2000
3000
4000
5000
1707
1712
1717
1722
1727

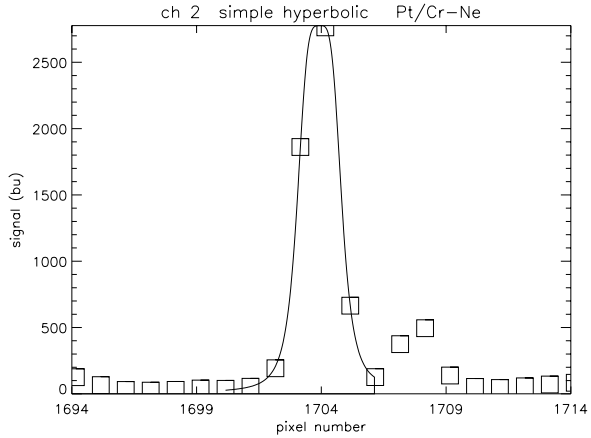
ch 2 simple hyperbolic Pt/Cr−Ne
signal (bu)
pixel number
0
500
1000
1500
2000
2500
1694
1699
1704
1709
1714

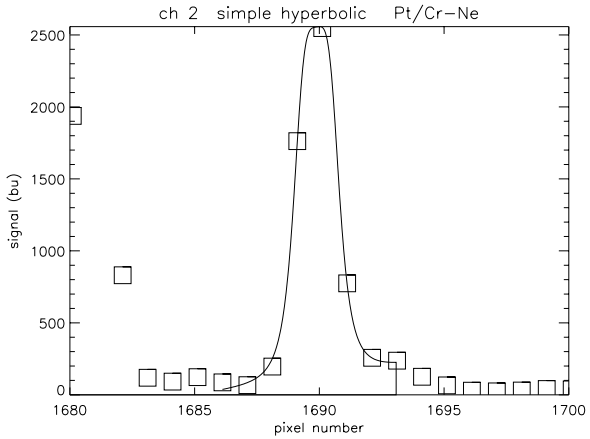
ch 2 simple hyperbolic Pt/Cr−Ne
signal (bu)
pixel number
0
500
1000
1500
2000
2500
1680
1685
1690
1695
1700

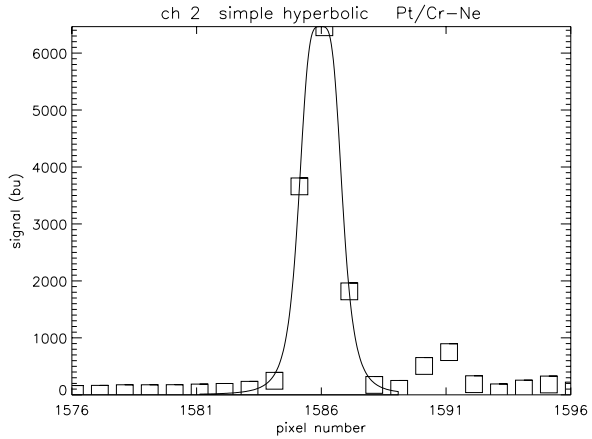
ch 2 simple hyperbolic Pt/Cr−Ne
signal (bu)
pixel number
0
1000
2000
3000
4000
5000
6000
1576
1581
1586
1591
1596

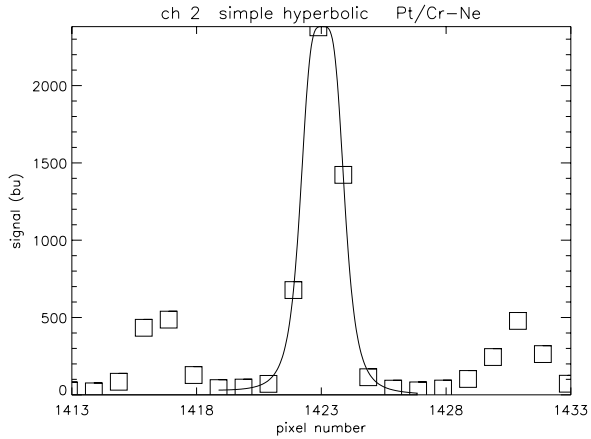
ch 2 simple hyperbolic Pt/Cr−Ne
signal (bu)
pixel number
0
500
1000
1500
2000
1413
1418
1423
1428
1433

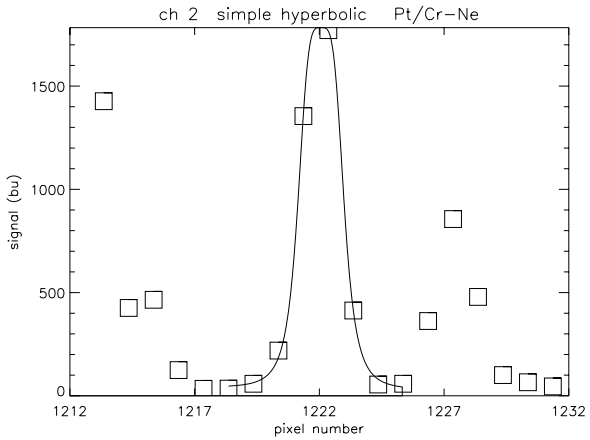
ch 2 simple hyperbolic Pt/Cr−Ne
signal (bu)
pixel number
0
500
1000
1500
1212
1217
1222
1227
1232